



1918

**TALLINNA TEHNIKAÜLIKOOL**  
TALLINN UNIVERSITY OF TECHNOLOGY

# **Analysis of Molecular Movements in Cardiac Myocytes**

ARDO ILLASTE

TALLINN 2012



THESIS ON NATURAL AND EXACT SCIENCES B124

# **Analysis of Molecular Movements in Cardiac Myocytes**

ARDO ILLASTE

**TUT**  
**PRESS**

TALLINN UNIVERSITY OF TECHNOLOGY  
Institute of Cybernetics  
Laboratory of Systems Biology

**This dissertation was accepted for the defense of the degree of Doctor of Philosophy (Engineering Physics) on 23 January 2012.**

**Supervisor:** Marko Vendelin, PhD  
Laboratory of Systems Biology, Institute of Cybernetics,  
Tallinn University of Technology, Tallinn, Estonia

**Opponents:** Pasi Tavi, PhD  
Department of Biotechnology and Molecular Medicine,  
University of East Finland, Kuopio, Finland

Allen Kaasik, PhD  
Department of Pharmacology,  
University of Tartu, Tartu, Estonia

Defense of the thesis: 23 February 2012

Declaration:

I hereby declare that this doctoral thesis, submitted for the doctoral degree at Tallinn University of Technology, is my original investigation and achievement and has not been submitted for the defense of any academic degree elsewhere.

---

Ardo Illaste

Copyright: Ardo Illaste, 2012, Creative Commons Attribution-NonCommercial-NoDerivs 3.0 Unported License

Colophon: This thesis was typeset with  $\LaTeX$  2 $\epsilon$  using André Miede's *classicthesis* style with modifications by David Schryer and Ardo Illaste to conform with Tallinn University of Technology style guidelines. The main font is Libertine (Times compatible). Biolinum is used for sans-serif text.

ISSN 1406-4723

ISBN 978-9949-23-241-3 (publication)

ISBN 978-9949-23-242-0 (PDF)

LOODUS - JA TÄPPISTEADUSED B124

# Molekulaarsete liikumiste analüüs südamelihaskudedes

ARDO ILLASTE

TTÜ  
KIRJASTUS



---

## CONTENTS

---

SUMMARY	vii
KOKKUVÕTE	viii
LIST OF PUBLICATIONS	ix
LIST OF CONFERENCE PRESENTATIONS	x
RELEASED SOFTWARE	xi
PREFACE	xii
ACKNOWLEDGEMENTS	xiii
ACRONYMS	xv
<b>THESIS</b>	17
1 INTRODUCTION	19
2 RASTER IMAGE CORRELATION SPECTROSCOPY	23
2.1 Fundamentals . . . . .	23
2.1.1 Image acquisition . . . . .	23
2.1.2 Correlation function & diffusion . . . . .	23
2.1.3 Time delay between pixels . . . . .	27
2.2 Extensions to RICS . . . . .	28
2.2.1 Motivation for modifications . . . . .	28
2.2.2 Variation of scanning angle . . . . .	28
2.2.3 Variation of scanning resolution . . . . .	30
2.2.4 Two diffusing species . . . . .	30
2.2.5 Triplet states . . . . .	31
2.3 Full form of correlation function . . . . .	32
3 ESTIMATION OF DIFFUSION COEFFICIENTS IN RAT CARDIOMYO- CYTES	33
3.1 Cardiomyocyte preparation . . . . .	33
3.2 Diffusion coefficients in cardiomyocytes . . . . .	34
3.3 Conclusions . . . . .	35
4 NUMERICAL SIMULATIONS OF RESTRICTED DIFFUSION	39
4.1 Computational model setup . . . . .	39
4.2 Barrier properties estimated from computational model . . . . .	42
4.3 Conclusions . . . . .	42
5 ONE-DIMENSIONAL COMPUTATIONAL RICS	45

CONTENTS

5.1	Motivation & model setup . . . . .	45
5.2	Barrier effects on regional diffusion coefficients . . . . .	45
5.3	Conclusions . . . . .	47
6	HYPERTROFIC CARDIOMYOPATHY IN RAF1 MUTANTS	49
7	DEVELOPMENT OF CARDIAC ENERGETICS IN POSTNATAL MOUSE HEART	51
8	CONCLUSIONS	53
	Extended RICS technique . . . . .	53
	Estimation of diffusion coefficients of fluorescent dyes . . . . .	54
	Mathematical modelling of restricted diffusion . . . . .	54
	Cardiomyocyte hypertrophy in Noonan syndrome . . . . .	54
	Development of energetic microdomains . . . . .	55
	<b>BIBLIOGRAPHY</b>	57
	<b>CURRICULUM VITAE</b>	63
	<b>APPENDIX</b>	69
	<b>PUBLICATION I</b>	71
	<b>PUBLICATION II</b>	77
	<b>PUBLICATION III</b>	91

---

## SUMMARY

---

**T**HIS DISSERTATION EXPLORES the fascinating world of cardiac function and dysfunction. Through application of various experimental and computational techniques new insights into aspects of intracellular diffusion restrictions, causes of hypertrophy, and development of cardiac energetics are gained. Experiments on rat cardiomyocytes using raster image correlation spectroscopy reveal a counterintuitive result, whereby diffusion of a smaller fluorescent molecule is restricted more than that of a larger one, when comparing diffusion in the cytosol to that in solution. A stochastic computational model of diffusion is applied to find a possible explanation for this result. Modeling results suggest the existence of regularly placed semi-permeable barriers in the cardiomyocyte situated  $\sim 1 \mu\text{m}$  apart and having very low permeabilities. Such structures in the intracellular environment could enact a significant role in the function of cardiomyocytes, as well as in dysfunctional states of the heart. Also discussed are experiments probing the causes of hypertrophic cardiomyopathy with the aim of studying mutations that affect signalling cascades and cause abnormalities in cardiomyocyte calcium handling.

---

## KOKKUVÕTE

---

**K**ÄESOLEVAS VÄITEKIRJAS SISENETAKSE südame funktsioneerimise keerulisse aga köitvasse maailma. Rakendades erinevaid eksperimentaalseid ja arvutuslikke meetodeid saadakse uusi teadmisi rakusiseste difusioonitakistuste, südame hüpertroofia ja südameenergeetika arenguliste muutuste valdkondadest. Raster korrelatsioon-spektroskoopia katsed roti südamelihasrakus näitavad, et väiksemate molekulide difusioon on raku sees rohkem takistatud kui suuremate molekulide difusioon. Sellele intuitisioonivastasele tulemusele leitakse seletus kasutades stohhastilist arvutuslikku mudelit modelleerimaks rakusisest takistatud difusiooni. Modelleerimistulemused vihjavad korrapäraste, osaliselt läbitavate barjääride olemasolule südamelihasrakkudes. Nimetatud barjäärid asuksid teine-teisest  $\sim 1 \mu\text{m}$  kaugusel ja oleks suhteliselt raskesti läbitavad. Sellised rakusisesed struktuurid võivad omada olulist rolli nii südamelihasrakkude normaalses toimimises kui ka patoloogilistes juhtudes. Antud töö esitab veel katsetulemusi südame hüpertroofia põhjuste uuringutest. Saadud tulemused selgitavad kuidas hüpertroofiat põhjustavad mutatsioonid mõjutavad signaalikaskaade ning põhjustavad ohtlikke kõrvalekaldeid kaltsiumiringluse normaalsest toimimisest südamelihasrakkudes.

---

## LIST OF PUBLICATIONS

---

- I Illaste A, Kalda M, Schryer DW, Sepp M ; **Life of mice - development of cardiac energetics.** *Journal of Physiology*, 588(23), December 2010
- II Dhandapany P, Fabris F, Tonk R, Illaste A, Karakikes I, Sorourian M, Sheng J, Hajjar R, Tartaglia M, Sobie R, Lebeche D, Gelb B; **Cyclosporine attenuates cardiomyocyte hypertrophy induced by RAF1 mutants in Noonan and LEOPARD syndromes.** *Journal of Molecular and Cellular Cardiology*, Volume 51, Issue 1, July 2011
- III Illaste A, Laasmaa M, Peterson P, Vendelin M; **Analysis of molecular movement reveals latticelike obstructions to diffusion in heart muscle cells.** *Biophysical Journal*, 2012, *in press*

### *Summary of author's contributions*

- I Organizer and main writer for Publication I.
- II For Publication II, which consists of work carried out in Mount Sinai School of Medicine, I carried out some of the confocal microscopy experiments, wrote data analysis software and performed data analysis to ascertain the differences in calcium handling between RAF1-mutation-induced hypertrophic and wildtype cardiomyocytes.
- III In Publication III, consisting of the main results of my doctoral studies, I conducted the raster image correlation spectroscopy (RICS) experiments, improved the design of the experimental protocol, wrote the code for and performed numerical simulations together with analysis of the results, and prepared a large part of the manuscript and figures.

---

LIST OF CONFERENCE PRESENTATIONS

---

- I Illaste A, Vendelin M; **Mathematical Model of Mitochondrial Energy Metabolism**; 64<sup>th</sup> Harden Conference on Mitochondrial Physiology, Ambleside, United Kingdom, September 14 - 18, 2007
- II Illaste A, Vendelin M; **Mathematical Model Of Mitochondrial Energy Metabolism** ; Biophysical Meeting 2008, Long Beach, California, USA, February 2 - 6, 2008
- III Illaste A, Vendelin M; **Computational Model Of Citric Acid Cycle And Oxidative Phosphorylation In Mitochondria**; Biophysical Meeting 2009, Boston, Massachusetts, February 28 - March 4, 2009
- IV Fabris F, Illaste A; Park M; Adler E D; Sobie E A; **Mechanisms Underlying Spontaneous Beating in Human Embryonic Stem Cell-Derived Cardiac Myocytes**; Biophysical Meeting 2010, San Francisco, California, USA, February 20 - 24, 2010
- V Illaste A, Laasmaa M, Schryer D, Birkedal R, Peterson P, Vendelin M; **Determination of Regional Diffusion Coefficients of Fluorescent ATP in Rat Cardiomyocytes**; Biophysical Meeting 2010, San Francisco, California, USA, February 20 - 24, 2010
- VI Illaste A, Laasmaa M, Birkedal R, Peterson P, Vendelin M; **Mapping Diffusion Coefficients of Fluorescent Dyes in Cardiomyocytes**; Biophysical Meeting 2011, Baltimore, Maryland, USA, March 5 - 9, 2011
- VII Illaste A, Laasmaa M, Peterson P, Vendelin M; **Analysis of Molecular Movement Reveals Latticelike Obstructions to Diffusion in Heart Muscle Cells**; Biophysical Meeting 2012, San Diego, California, USA, February 25 - 29, 2012

---

**RELEASED SOFTWARE**

---

LSJuicer – a multi-platform tool for analysing fluorescence vs. time data (e.g., linescan images from confocal microscopes, csv data from spectrophotometers, fluorimeters, etc). This open-source software was used for analyzing  $\text{Ca}^{2+}$  transients in Publication II and was also employed for  $\text{Ca}^{2+}$  spark analysis in [22]. Available at <http://lsjuicer.googlecode.com>

---

## PREFACE

---

**T**HIS DISSERTATION CONTAINS selected results from my doctoral studies. The main focus of these studies has been on applying RICS for determining properties of diffusion in cardiomyocytes. In the beginning stages of this project an attempt was made to use existing equipment available at Tallinn University of Technology. Unfortunately, after months of trials it became clear that this equipment was not able to carry out the experimental protocol we had developed in a satisfactory manner. As a result of this, we designed and built a confocal microscopy setup of our own, optimized for performing RICS experiments.

Before the building and testing was complete, however, I travelled to New York in order to spend 8 months at Mount Sinai School of Medicine in the laboratory of Dr. Eric A. Sobie. This side-project, although also involving confocal microscopy and cardiac muscle cells, was quite different from what I had previously been involved in. The collaboration developed into an article on hypertrophic cardiomyocytes (Publication II) and resulted in the release of a software package aimed at calcium transient analysis.

On my return to Estonia the work on RICS resumed. Although the technical difficulties with the equipment had now been resolved, optimization of the experimental protocol remained. After a year of fine-tuning and improvements, experiments started to become reproducible. Parallel to conducting experiments, I started working on a stochastic computational model of diffusion that I employed for running RICS simulations *in silico* in order to obtain further insights into the results yielded by biological experiments. The results of this combined approach to study diffusion in cardiomyocytes are presented in Publication III and form the main body of this text.

As RICS is only one method used in our laboratory in its quest to unravel the subtleties of cardiac energetics, it is only suitable that we would monitor other developments in the field. One direct result of this is an article (Publication I) reviewing recent results in postnatal development of energetic microdomains in mouse.

---

## ACKNOWLEDGEMENTS

---

**M**Y CURIOSITY TOWARDS the world of science got a major boost when my father started purchasing the Scientific American journal in the early nineties so that I could satisfy my appetite for reading about intriguing new aspects of this world. The books that accumulated in my home on topics such as cellular automata, chaos, complexity and fractals captured my attention and kindled my interest in these fascinating fields. I am grateful for his effort in immersing me in these topics and his interest in my ongoing scientific endeavours. The support of my mother for my studies and interests was equally crucial in ensuring that I reach where I am today. I am thankful for the help and guidance from my parents in everything I have undertaken.

During my bachelor studies, after completing a course given by Professor Jüri Engelbrecht, I had the honour of being asked to join the Institute of Cybernetics. Having read his books on chaos and complexity it was a thrill to take one of his classes. It was beyond my wildest dreams, however, to be invited to work on these very same topics I had been reading about and tinkering with on my own just a few years prior. I am thankful to Professor Engelbrecht also for acquainting me with my supervisor Dr. Marko Vendelin, whose enthusiasm and energy accompanied me on my journey into cardiac energetics. Marko's advice and knowledge have made me feel confident when navigating the stormy and unpredictable seas of biophysical research. Also, I will be forever in his debt for introducing me to the most special person in my life.

It has been a pleasure working together with all the members of the Systems Biology lab: the original PhD student gang David, Mari and Mervi with whom we have been through thick and thin, and the latecomers Martin, Niina, Natalja, Jelena, Merle and Päivo. This work would not have been possible without their help. My gratitude also belongs to Dr. Rikke Birkedal for her efforts in ensuring that I have cells to perform experiments on (especially during the do-or-die week during the christmas break in 2011) and to Dr. Pearu Peterson for keeping a watchful eye that the temptation of fuzzy language is fought and that only words based on facts ever get put down on paper.

I am grateful to Dr. Eric A. Sobie from the Mount Sinai School of Medicine for offering me the opportunity to work with him for 8 months in New York and for stepping up to help in a bleak situation caused by unfortunate circumstances.

## CONTENTS

Lastly, without the unconditional support and love from my wife Hena, the last years of this journey would have been an immeasurably more arduous undertaking.

Financial support from the Wellcome Trust, the Estonian Science Foundation, as well as the Archimedes Foundation is appreciated.

---

## ACRONYMS

---

AATP	ATTO633-ATP
ADEX	Alexa647-dextran 10K
ANT	adenine nucleotide translocase
ATP	adenosine triphosphate
CF	correlation function
CK	creatine kinase
CM	cardiomyocyte
DC	diffusion coefficient
FCS	fluorescence correlation spectroscopy
HCM	hypertrophic cardiomyopathy
IBS	inter-barrier space
ICS	image correlation spectroscopy
LSCM	laser scanning confocal microscope
NMR	nuclear magnetic resonance
PSF	point spread function
RAF1	serine/threonine-protein kinase
RICS	raster image correlation spectroscopy
ROS	reactive oxygen species
SERCA	sarco/endoplasmic reticulum Ca <sup>2+</sup> ATPase



# THESIS



---

## INTRODUCTION

---

**T**HE SUBJECTS THAT HAVE BEEN explored during my doctoral studies, employ various methods and approaches. They all, however, deal with the common underlying topic of function and dysfunction of cardiac cells.

The first of these subjects relates to the study of how intracellular compartmentation and diffusion restrictions influence cardiac energetics. The existence of diffusion restrictions has been shown in numerous experiments. For example, studies on caffeine induced tension transients have revealed the restricted access of externally supplied adenosine triphosphate (ATP) to intracellular enzymes consuming ATP [11]. Measurements of  $O_2$  consumption by mitochondria during oxidative phosphorylation in permeabilized cardiomyocytes also indicate existence of diffusion restrictions between mitochondria and extracellular solution [13, 25]. The presence of such compartmentation can be visualized by looking at oscillations of mitochondrial membrane potential induced by reactive oxygen species (ROS) [14] and modulation of the ATP sensitive potassium channel by phosphocreatine [1]. Compartmentation caused by such restrictions and how this affects energy transfer in the heart is a clinically relevant problem [9] and concentrations of molecules involved in intracellular energy transfer can be used as a predictive indicator of mortality in dilated cardiomyopathy patients [19].

Substantial diffusion restrictions have so far been suggested from indirect measurements as mentioned above. In skeletal muscle, nuclear magnetic resonance (NMR) experiments have found diffusion of ATP to be hindered compared to diffusion in water [4, 15]. However, the decrease in diffusion coefficients found in these NMR experiments is not big enough to explain the experimental results from oxygraphy measurements listed above. According to computational modeling attempting to reproduce results from oxygen consumption experiments [24], a decrease several times higher than that found in NMR experiments in the diffusion coefficients of adenine nucleotides is necessary to account for the results from oxygraphy measurements.

Employing a novel fluorescence correlation spectroscopy (FCS) based technique termed raster image correlation spectroscopy (RICS), diffusion of fluorescent ATP

has been measured in cardiac myocytes [29]. The RICS method makes use of the fact that in a confocal image each pixel is separated from another not only in distance but also in time [6, 7]. Combining this knowledge with FCS methods allows one to determine information about molecular dynamics, concentrations and diffusion coefficients from images obtained with most laser scanning confocal microscopes (LSCMs). When applied to estimating the diffusion coefficient (DC) of fluorescently labelled ATP in rat cardiomyocytes [29], a more pronounced reduction was found compared to that determined by NMR. Due to the technical difficulties experienced in [29] the RICS method was extended further and has developed into what forms the main results of this dissertation.

The extended RICS technique developed herein was applied to estimate the DCs of two different fluorescent molecules (ATTO633-ATP and Alexa647-dextran 10K) in rat cardiomyocytes. The results obtained from these measurements were used to determine parameters of hypothesized diffusion restrictions in form of semi-permeable barriers. This was carried out with the aid of a stochastic computational model of restricted diffusion. The extended RICS method was applied in analysis of both, experimental and modelled data. Chapter 2 introduces the RICS method and the fundamentals of the extensions to it that have been employed in this dissertation. It is almost entirely composed of the first chapter of the Supporting Material of Publication III and is included in full to familiarize the reader with the subject. Chapter 3 presents a summary of the experimental results, while Chapter 4 lays out the results obtained from computational model of restricted diffusion. Information presented in Chapters 3 to 4 are concise summaries of the main results given in detail in Publication III and its supporting material. In Chapter 5 some hitherto unpublished aspects concerning computational studies on one-dimensional regional RICS are presented.

The second topic explored in this work concerns hypertrophic cardiomyopathy caused by the Noonan syndrome, which is a relatively common genetic disorder (affecting 1 in 1000-2500 births [5]). It causes abnormal development in many parts of the body and can result in congenital heart defects [20, 27]. Chapter 6 covers results from the experimental study presented in full detail in Publication II, where three common mutations responsible for Noonan syndrome and their effect on downstream signalling pathways are investigated. Methods employed included immunoblotting for determining changes in expression levels of several proteins playing vital roles in  $\text{Ca}^{2+}$  signalling and confocal fluorescence measurements to establish possible dysfunction of  $\text{Ca}^{2+}$  handling.

Chapter 7 summarizes the main conclusions from Publication I, where a review of developmental changes in formation of energetic microdomains in cardiomyocytes was presented.

In summary, this dissertation presents a concise overview of the work performed during my doctoral studies. With the exception of Chapter 2, where the details of the extended RICS method have been laid out to introduce the topic to the reader, chapters present only the main results and conclusions from each of the studied topics in order to avoid excessive duplication with respect to the full publications given in the appendix. The reader is invited to consult the appended publications to gain more profound insight into the background information, methods used and physiological implications of the results obtained.



---

## RASTER IMAGE CORRELATION SPECTROSCOPY

---

**R**ASTER IMAGE CORRELATION SPECTROSCOPY is based on merging the concepts of LSCM, FCS and image correlation spectroscopy (ICS)[3, 6]. Detailed reviews are available covering the method and how it relates to other FCS-based methods [7, 10]. Here, a brief overview of the concepts behind RICS and to our modification to this method are presented.

### 2.1 FUNDAMENTALS

#### 2.1.1 *Image acquisition*

Fundamental to the method of RICS is the realization that in an image obtained by a LSCM, pixels on the image are not only separated in space but also in time [6]. Photons emitted by excited fluorescent molecules are recorded as raster images as the mirrors scan the laser beam on the specimen. When recording a two dimensional raster image, the laser beam moves along one image axis ( $\xi$ ), spending  $\tau_d$  seconds acquiring each pixel on the line (dwell time), then flies back to the beginning of the line with flyback time  $\tau_f$ , moves one pixel forward in the other axis ( $\psi$ ) and records the second line. This sequential processes is repeated until the whole image has been scanned line by line (Fig. 1), resulting in a rectangular grid of pixels separated in space and time.

#### 2.1.2 *Correlation function & diffusion*

By calculating the correlation function (CF) of the scanned image it is possible to extract information about the space-time relationship between the pixels and to characterize, for example, reaction kinetics, translational and rotational diffusion, conformational dynamics, molecular flow, etc. [7, 10, 16]. This can be done by fitting experimentally obtained CF s with theoretical CF curves derived for the

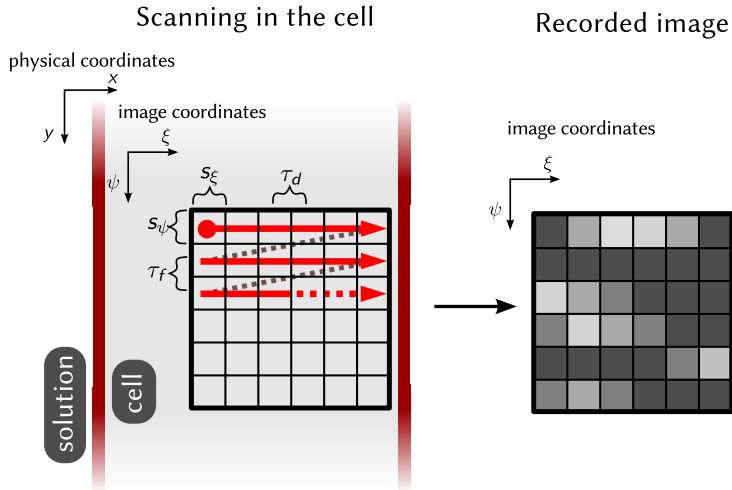


**Figure 1** – RICS image acquisition. A raster image consisting of a grid of pixels is acquired within a cell. Pixels are separated by  $s_\xi, s_\psi$   $\mu\text{m}$  spatially and by  $\tau_d, n_\xi \times \tau_d + \tau_f$   $\mu\text{s}$  temporally in the  $\xi$  and  $\psi$  directions, respectively. In the default case the image coordinates  $\xi, \psi$  align with the physical coordinates  $x, y$ . The image obtained (on the right) shows traces of diffusing molecules within the cell.

phenomenon being observed. In this paper we focus on applying RICS on analysis of diffusion of fluorescent dyes.

The correlation function  $G(\Delta\xi, \Delta\psi, \Delta\zeta)$  indicates the similarity of an image to a copy of itself shifted by  $\Delta\xi$  in the  $\xi$  direction,  $\Delta\psi$  in the  $\psi$  direction (see Fig. 2) and, in case a 3D stack of images is analyzed,  $\Delta\zeta$  in the  $\zeta$  direction (otherwise  $\Delta\zeta = 0$ ).

The CF for a given shift is calculated by multiplying the fluorescence values in the original image with values in the shifted image and averaging over all the pixels. The result is normalized to average image fluorescence squared:

$$G(\Delta\xi, \Delta\psi, \Delta\zeta) = \frac{\langle F(\xi, \psi, \zeta) \cdot F(\xi + \Delta\xi, \psi + \Delta\psi, \zeta + \Delta\zeta) \rangle_{\xi, \psi, \zeta}}{\langle F \rangle_{\xi, \psi, \zeta}^2} - 1, \quad (2.1)$$

where  $\langle \dots \rangle$  signifies averaging over the whole image.

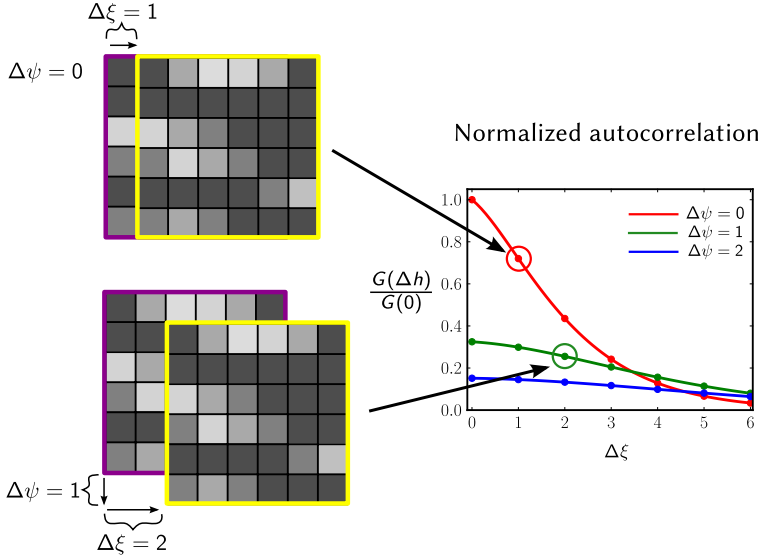


**Figure 2** – The correlation function  $G(\Delta\mathbf{h})$  for the shift  $\Delta\mathbf{h} = (\Delta\xi, \Delta\psi)$  is calculated by shifting a copy of the original image, multiplying the fluorescence values and averaging over the image. Arrows indicate the location of the correlation value for the shifts shown. The CF here is normalized to the zero-shift correlation  $G(0)$  from Eq.2.7.

The CF can also be calculated in terms of fluorescence fluctuations from the average  $\delta F = F - \langle F \rangle$  by substituting  $F = \delta F + \langle F \rangle$  into Eq.2.1:

$$G(\Delta\xi, \Delta\psi, \Delta\zeta) = \frac{\langle \delta F(\xi, \psi, \zeta) \cdot \delta F(\xi + \Delta\xi, \psi + \Delta\psi, \zeta + \Delta\zeta) \rangle_{\xi, \psi, \zeta}}{\langle F \rangle_{\xi, \psi, \zeta}^2}.$$

It is more convenient to present the CF in vector form with image shift vector  $\Delta\mathbf{h} = [\Delta\xi, \Delta\psi, \Delta\zeta]$  and position vector  $\mathbf{h} = [\xi, \psi, \zeta]$ :

$$G(\Delta\mathbf{h}) = \frac{\langle \delta F(\mathbf{h}) \cdot \delta F(\mathbf{h} + \Delta\mathbf{h}) \rangle_{\mathbf{h}}}{\langle F \rangle_{\mathbf{h}}^2}. \quad (2.2)$$

The physical coordinates corresponding to image coordinates  $\mathbf{h}$  are  $\mathbf{p} = \mathbf{p}_0 + \mathbf{h}\mathbf{S}$ . Here,  $\mathbf{p}_0$  is the physical location at the 0-th pixel and  $\mathbf{S} = \text{diag}(s_\xi, s_\psi, s_\zeta)$  is a diagonal matrix containing pixel sizes in each image dimension. Shift  $\Delta\mathbf{h}$  in im-

age coordinates converts to a shift  $\Delta\mathbf{p} = [\Delta x, \Delta y, \Delta z]$  in the physical coordinate system:

$$\begin{aligned}\Delta\mathbf{p} &= \Delta\mathbf{h}\mathbf{S} = [\Delta\xi, \Delta\psi, \Delta\zeta] \begin{pmatrix} s_\xi & 0 & 0 \\ 0 & s_\psi & 0 \\ 0 & 0 & s_\zeta \end{pmatrix} \\ &= [\Delta\xi \cdot s_\xi, \Delta\psi \cdot s_\psi, \Delta\zeta \cdot s_\zeta] = [\Delta x, \Delta y, \Delta z].\end{aligned}$$

For simplicity we consider that the fluorescence signal recorded at location  $\mathbf{p}$  is obtained from the convolution of the point spread function (PSF) of the microscope and the concentration of the fluorescent dye ( $c$ ) in the PSF volume.

$$F(\mathbf{p}) = B \int W(\mathbf{r}) \cdot c(\mathbf{p} - \mathbf{r}) \, d\mathbf{r},$$

where  $W$  is the PSF and  $B$  a parameter called brightness given by  $B = q\sigma Q$  [16]. Here,  $q$  is the quantum efficiency of detecting emitted photons,  $\sigma$  the cross-section of absorption and  $Q$  the emission quantum yield of the fluorescent molecule. Employing this relationship between recorded fluorescence and concentration, Eq.2.2 can be used to connect the fluctuations of fluorescence visible on the recorded image to fluctuations in concentration of the diffusing dye:

$$\begin{aligned}G(\Delta\mathbf{h}) &= \frac{\langle \delta F(\mathbf{p}) \cdot \delta F(\mathbf{p} + \mathbf{q}(\Delta\mathbf{h})) \rangle_{\mathbf{p}}}{\langle F(\mathbf{p}) \rangle_{\mathbf{p}}^2} \\ &= \frac{1}{\langle c(\mathbf{p}) \rangle_{\mathbf{p}}^2} \iint W(\mathbf{r}) W(\mathbf{r}') G_D(\mathbf{r}, \mathbf{r}', \Delta\mathbf{h}) \, d\mathbf{r} \, d\mathbf{r}'.\end{aligned}\quad (2.3)$$

$G_D$  is the correlation due to diffusion and can be calculated analytically [28]:

$$\begin{aligned}G_D(\mathbf{r}, \mathbf{r}', \Delta\mathbf{h}) &= \langle \delta c(\mathbf{p} + \mathbf{r}) \cdot \delta c(\mathbf{p} + \mathbf{r}' + \mathbf{q}(\Delta\mathbf{h})) \rangle_{\mathbf{p}} \\ &= \langle c \rangle \prod_{i=1}^n (4\pi D_i)^{-\frac{1}{2}} \exp\left(-\frac{(\mathbf{r}'_i + \mathbf{q}_i - \mathbf{r}_i)^2}{4D_i t(\Delta\mathbf{h})}\right),\end{aligned}\quad (2.4)$$

where  $\delta c(\mathbf{p})$  is the fluctuation in concentration of the fluorescent dye at location  $\mathbf{p}$ ,  $\langle c \rangle$  is the average concentration,  $D_i$  are diagonal components of the diffusion tensor [4] in the coordinate system composed of principal axes, collected here into  $\mathbf{D} = [D_x, D_y, D_z]$ . If diffusion is isotropic then all components in  $\mathbf{D}$  are equal. In the case of anisotropic diffusion, components of  $\mathbf{D}$  can have different

values. The time delay  $t(\Delta\mathbf{h})$  indicates how much time has passed between acquisition of two pixels separated by the shift  $\Delta\mathbf{h}$ . The number  $n$  indicates the number of dimensions and in general  $n=3$ . The equations are still valid, however, for lower  $n$  values as well.

Although the PSF is dependent on the microscope and should be measured experimentally, an analytic estimate is often used [16, 28]:

$$W(\mathbf{r}) = \prod_{i=1}^n \exp\left(-2\frac{r_i^2}{w_i^2}\right) \quad (2.5)$$

Here,  $\mathbf{w}$  is a vector describing the width of the PSF in spatial directions. It is customary to perform calibrations using a fluorescent molecule with a known concentration in order to determine the  $\mathbf{w}$  values. Furthermore, the  $x$  and  $y$  components of  $\mathbf{w}$  are often assumed to be equal.

Using the PSF definition from Eq.2.5 and  $G_D$  from Eq.2.4 the integrals in Eq.2.2 can be calculated and the following analytic form obtained:

$$G(\Delta\mathbf{h}) = \frac{1}{\langle c \rangle} \prod_{i=1}^n \left[ \frac{1}{\sqrt{\pi(4D_i t(\Delta\mathbf{h}) + w_i^2)}} \exp\left(-\frac{q(\Delta\mathbf{h})_i^2}{4D_i t(\Delta\mathbf{h}) + w_i^2}\right) \right]. \quad (2.6)$$

From this result it can be seen that with zero shift (i.e.,  $\Delta\mathbf{h} = (0, 0, 0)$ ) the CF gives:

$$G(0) = \frac{1}{\langle c \rangle} \prod_{i=1}^n \frac{1}{\sqrt{\pi w_i}}. \quad (2.7)$$

As  $G(0)$  is independent of the diffusion of the fluorescent molecule it can be used to determine the global concentration of the molecule or, knowing that, the properties of the PSF (i.e., components of  $\mathbf{w}$ ).

### 2.1.3 Time delay between pixels

Scanning a 2D raster image with  $n_\xi$  pixels in the  $\xi$  direction, with  $\tau_d$  seconds used as the dwell time for all pixels and  $\tau_f$  being the time that it takes for the beam to move from the end of one line to the beginning of the next, the time delay between two pixels separated by the shift  $\Delta\mathbf{h}$  used in Eqs. 2.6 and 2.9 is:

$$t(\Delta\mathbf{h}) = t(\Delta\xi, \Delta\psi) = \Delta\xi \cdot \tau_d + \Delta\psi \cdot (n_\xi \cdot \tau_d + \tau_f). \quad (2.8)$$

Inserting this relation in the CF Eqs. 2.6 and 2.9 will yield the function that can be used for fitting experimentally obtained data and obtaining diffusion coefficients.

## 2.2 EXTENSIONS TO RICS

### 2.2.1 Motivation for modifications

As we have demonstrated, RICS can be used to determine anisotropy of diffusion by varying the time delay between physical location in the sample during a scan. This can be achieved by altering the angle of scanning [29].

Also, diffusion dependent changes in the CF can be subtle, making them hard to detect and fit, especially with noisy data. Through changes in scanning resolution additional aspects of the CF can be estimated, leading to a larger amount of datapoints available for fitting.

### 2.2.2 Variation of scanning angle

In order to detect anisotropy of diffusion, several scanning angles can be used to alter the time delay between pixels acquired from the same location [29]. When scanning is performed at an angle  $\alpha$  relative to the physical coordinate axes, the

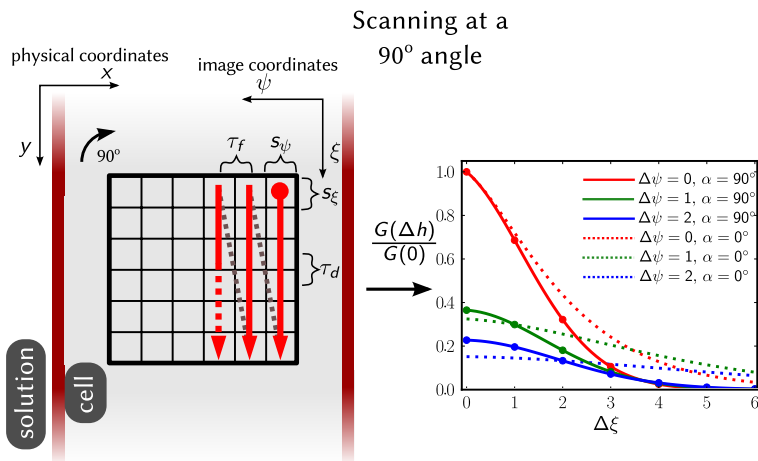


**Figure 3** – Modified scanning for RICS. Scanning at an angle  $\alpha$  rotates the image coordinates with respect to the physical coordinates and results in a different CF which can be used for determining anisotropy of diffusion. The CF for  $0^\circ$  angle scanning from Fig. 2 is shown in dotted lines and differs from the CF obtained for an image scanned at a different angle. In the shown example, scanning is performed at a  $90^\circ$  angle, effectively aligning the image  $\xi$  axis with the physical  $y$  axis and image  $\psi$  axis with physical  $x$  axis.

CF equations need to be modified to account for this. For example, if scanning is performed under a  $90^\circ$  angle, the image  $\xi$  and  $\psi$  axes actually correspond to the physical  $y$  and  $x$  axes, respectively (see Fig. 3). The CF that takes the scanning angle into account is:

$$G(\Delta\mathbf{h}, \alpha) = \frac{1}{\langle c \rangle} \prod_{i=1}^n \left[ \frac{1}{\sqrt{\pi (4D_i t(\Delta\mathbf{h}) + w_i^2)}} \exp \left( -\frac{q(\Delta\mathbf{h}, \alpha)_i^2}{4D_i t(\Delta\mathbf{h}) + w_i^2} \right) \right], \quad (2.9)$$

where the physical shift  $\Delta\mathbf{p}$  is now a function of the rotation angle  $\alpha$ :

$$\Delta\mathbf{p}(\Delta\mathbf{h}, \alpha) = \Delta\mathbf{h} \mathbf{S} (\mathbf{M}(\alpha))^T \quad (2.10)$$

$\mathbf{M}(\alpha)$  is the rotation matrix for rotation angle  $\alpha$ . For rotating around the  $z$  axis, as is done in this paper, the rotation matrix is:

$$\mathbf{M}(\alpha) = \begin{pmatrix} \cos \alpha & -\sin \alpha & 0 \\ \sin \alpha & \cos \alpha & 0 \\ 0 & 0 & 1 \end{pmatrix}.$$

It is possible to do rotations around another axis or even multiple rotations around different axes by inserting a suitable rotation matrix in Eq.2.10 (assuming that the microscope employed is able to perform such scans).

The physical shift vector from Eq.2.10 for rotation  $\alpha$  around the  $z$  axis is:

$$\begin{aligned} \Delta\mathbf{p}(\Delta\mathbf{h}, \alpha) &= [\Delta x, \Delta y, \Delta z] \\ &= \Delta\mathbf{h} \mathbf{S} (\mathbf{M}(\alpha))^T \\ &= \begin{pmatrix} \Delta\xi \cdot s_\xi \\ \Delta\psi \cdot s_\psi \\ \Delta\zeta \cdot s_\zeta \end{pmatrix}^T \begin{pmatrix} \cos \alpha & \sin \alpha & 0 \\ -\sin \alpha & \cos \alpha & 0 \\ 0 & 0 & 1 \end{pmatrix} \\ &= \begin{pmatrix} \Delta\xi \cdot s_\xi \cdot \cos \alpha - \Delta\psi \cdot s_\psi \cdot \sin \alpha \\ \Delta\xi \cdot s_\xi \cdot \sin \alpha + \Delta\psi \cdot s_\psi \cdot \cos \alpha \\ \Delta\zeta \cdot s_\zeta \end{pmatrix}^T. \end{aligned}$$

It is easy to verify that when  $\alpha = 0$ ,  $\mathbf{M}$  reduces to the identity matrix and Eq.2.9 simplifies to Eq.2.6.

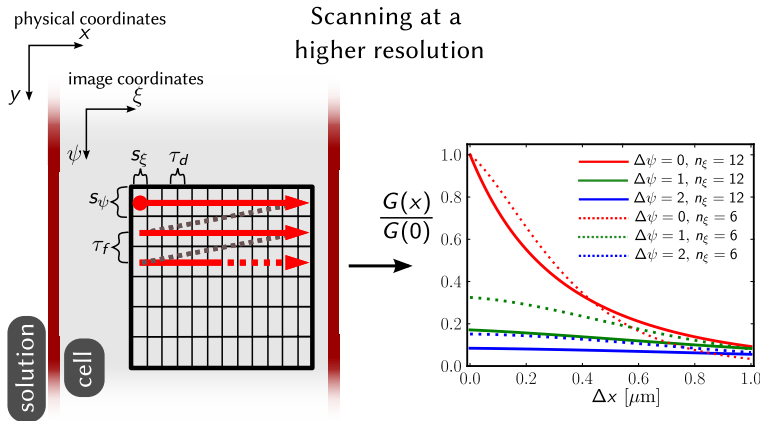


**Figure 4** – Modified scanning for RICS. Changing the scanning resolution also alters the shape of the CF. In the example shown, the image is scanned at two times higher resolution resulting in the CF depicted with solid lines. Since the pixel dwell time  $\tau_d$  is not changed, scanning one line takes two times longer. For comparison, the CF from Fig. 2 is shown in dotted lines. The horizontal axis now shows physical shift values in  $\mu\text{m}$  since the pixel size and count for the two CFs is different.

### 2.2.3 Variation of scanning resolution

Changes in scanning resolution [29] or pixel dwell time  $\tau_d$  [8] will alter the time delay function Eq.2.8 and result in different correlation curves. An example for scanning with double resolution but unchanged pixel dwell time  $\tau_d$  in  $\xi$  axis is shown on Fig. 4. An increased resolution increases the time taken to record a line and decreases pixel size. Therefore, in order to compare the CF for different resolutions it is more suitable to present them as functions of physical distance as is done in Fig. 4.

### 2.2.4 Two diffusing species

It is possible for the fluorescent molecule to bind with other, larger, molecules in the intracellular solution. As a result, two subspecies of the fluorescent molecule would be diffusing in the cell: the faster unbound form and the slower bound form. Assuming that fluorescent properties of the dye are not altered as a result of

binding and that the two species are non-interacting (i.e., the binding/unbinding is relatively slow), the CF for two species diffusing is [12, 16] :

$$G(\Delta\mathbf{h}, \alpha) = \frac{1}{\langle c_1(\mathbf{p}) + c_2(\mathbf{p}) \rangle_{\mathbf{p}}^2} \cdot \iint W(\mathbf{r})W(\mathbf{r}') (\langle c_1 \rangle \cdot g_{D1} + \langle c_2 \rangle \cdot g_{D2}) \, d\mathbf{r} \, d\mathbf{r}', \quad (2.11)$$

where  $\langle c_1 \rangle$ ,  $\langle c_2 \rangle$  are concentrations of the two components and  $g_{D1}$  and  $g_{D2}$  are given by  $G_{Dk}(\mathbf{r}, \mathbf{r}', \Delta\mathbf{h}, \alpha) / \langle c_k \rangle$ , ( $k = 1, 2$ ). Inserting the gaussian PSF given in Eq.2.5 to calculate the CF for two components from Eq.2.11:

$$G(\Delta\mathbf{h}, \alpha) = \frac{1}{(\langle c_1 \rangle + \langle c_2 \rangle)^2} \cdot \left[ \langle c_1 \rangle \prod_{i=1}^n \frac{\exp\left(-\frac{q(\Delta\mathbf{h}, \alpha)_i^2}{4D_{1,i}t(\Delta\mathbf{h}) + w_i^2}\right)}{\sqrt{\pi(4D_{1,i}t(\Delta\mathbf{h}) + w_i^2)}} + \langle c_2 \rangle \prod_{i=1}^n \frac{\exp\left(-\frac{q(\Delta\mathbf{h}, \alpha)_i^2}{4D_{2,i}t(\Delta\mathbf{h}) + w_i^2}\right)}{\sqrt{\pi(4D_{2,i}t(\Delta\mathbf{h}) + w_i^2)}} \right],$$

where  $D_{1,i}$ ,  $D_{2,i}$  are diffusion coefficients in direction  $i$  for the first and second component, respectively.

### 2.2.5 Triplet states

It is possible for a fluorescent molecule to go into a so-called triplet state from where it relaxes back to ground state after a delay much longer than it takes for the normal excitation-emission cycle to complete. This phenomenon, if ignored, could cause diffusion coefficients to be overestimated. To account for this effect, we multiply the CF function (Eq.2.9 or Eq.2.11) with a compensation factor [8, 10, 12, 31] :

$$1 + \frac{T}{1-T} \exp\left(-\frac{t}{\tau}\right), \quad (2.12)$$

where  $T$  is the fraction of molecules in triplet state and  $\tau$  the triplet state relaxation time.

### 2.3 FULL FORM OF CORRELATION FUNCTION

In this work the experimentally measured PSF was used instead of the approximated one (Eq.2.5), necessitating numerical integration for each CF evaluation:

$$G(\Delta\mathbf{h}, \alpha) = \frac{1}{\langle F_1(\mathbf{p}) + F_2(\mathbf{p}) \rangle_{\mathbf{p}}^2} \left( 1 + \frac{T}{1-T} \exp\left(-\frac{t}{\tau}\right) \right) \cdot \iint \mathcal{W}(\mathbf{r})\mathcal{W}(\mathbf{r}') (\langle c_1 \rangle \cdot g_{D1} + \langle c_2 \rangle \cdot g_{D2}) \, d\mathbf{r} \, d\mathbf{r}' \quad (2.13)$$

This is the CF form used for fitting experimental data in this work.

---

## ESTIMATION OF DIFFUSION COEFFICIENTS IN RAT CARDIOMYOCYTES

---

### 3.1 CARDIOMYOCYTE PREPARATION

**N**EITHER OF THE DYES USED in this work (ATTO633-ATP and Alexa647-dextran 10K) are able to permeate the cell membrane. This can be seen on Fig.5, where, contrary to the fluorescent signal from the membrane permeable form of Mitotracker Green dye (Fig.5A), ATTO633-ATP is not able to pass into the cytosol (Fig.5B). In order to use RICS to estimate the DCs of these dyes, they have to be allowed to enter into the cell. This can be achieved through saponin permeabilization of the cell membrane [29]. Initially, saponin permeabilization was used also in this work, but it became evident that exposure to saponin resulted in the cells hypercontracting within a few hours. The full protocol for RICS measurements, however, takes several hours to complete. This necessitated the need to come up with an alternative method of introducing the dyes into the cell.

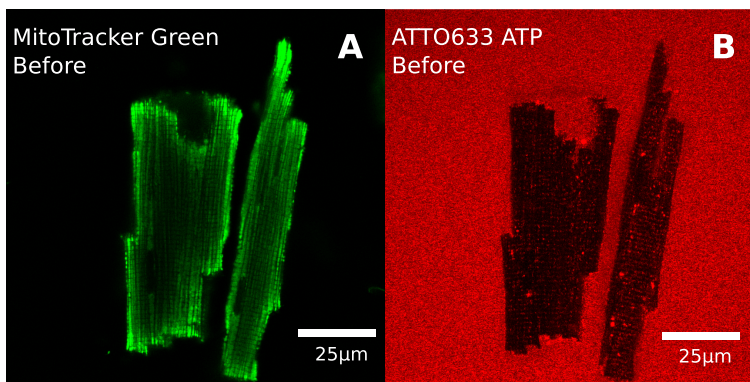


**Figure 5** – Confocal images of rat cardiomyocytes in measurement solution. On the left image (A) membrane permeable Mitotracker Green dye has permeated the membrane and accumulates in the cell. On the right image (B) ATTO633-ATP is visible in the solution outside the cell and is not able to enter the cytosol.

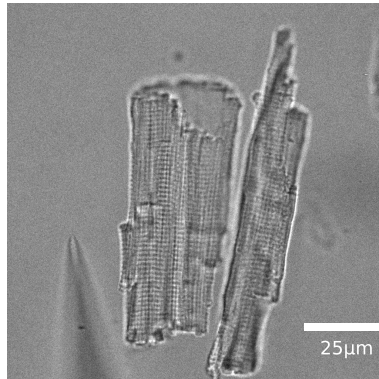


**Figure 6** – The cell membrane is permeated mechanically with a glass pipette (tip  $\varnothing 0.5 \mu\text{m}$ ). Both the pipette and the cell are shown on this transmission image.

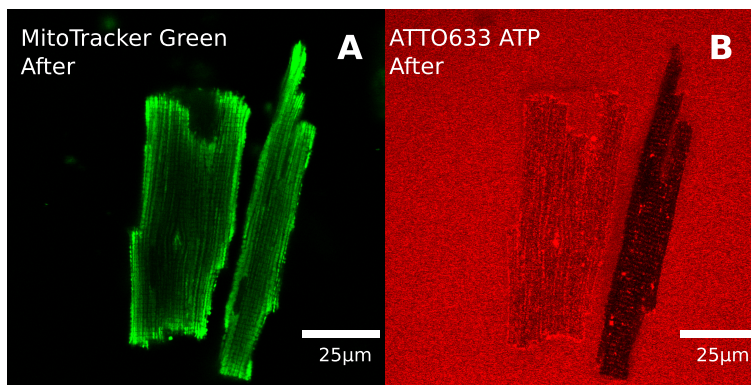


**Figure 7** – Confocal images of cardiomyocytes after “poking”. The Mitotracker Green signal is unaltered (A) but fluorescence from ATTO633-ATP is now visible in the cytosol.

In this work, viable permeabilized cells were obtained by using a glass pipette with a diameter of  $0.5 \mu\text{m}$  to mechanically “poke” 2-3 holes into the cell membrane (Fig.5). Within minutes after completing this procedure, fluorescence signal from ATTO633-ATP could be recorded from within the cell. After this the full RICS protocol was carried out. Compared to saponin permeabilization, the viability of the “poked” cells was increased by several hours.

### 3.2 DIFFUSION COEFFICIENTS IN CARDIOMYOCYTES

Diffusion coefficient estimates were obtained by fitting the experimentally calculated CF with the theoretical CF from Eq.2.13 as explained in detail in Publication III. A summary of the results obtained is presented in Table 1. The table with full experimental results is given in Publication III. The two DCs shown for

Dye	Media	Cmp.	Diffusion	
			$D_{TR}$ $\mu\text{m}^2/\text{s}$	$D_L$ $\mu\text{m}^2/\text{s}$
ATTO633-ATP	water solution		326±13	
			195±8	
	CM	1	0.7±0.3	0.8±0.2
		2	24±6	35±8
Alexa647-dextran10K	water		62±1	
	solution		53±1	
	CM		16±2	19±3
ATTO655-COOH	water		454±3	

**Table 1** – Diffusion coefficient values for ATTO633-ATP and Alexa647-dextran 10K in water, solution and cardiomyocyte. In case of anisotropic diffusion, DC values for both transverse(TR) and longitudinal(L) directions are given (DC in the z direction is assumed equal to the DC in x direction). For isotropic diffusion only one DC is shown which applies for all directions. Data shown is mean  $\pm$  standard deviation.

ATTO633-ATP in cardiomyocyte (CM) are the slow and freely diffusing forms of the dye. Separating ATTO633-ATP into two subspecies was necessary due to ATTO633-ATP probably binding to some intracellular proteins and thereby creating a second, slower diffusing form of ATTO633-ATP. For Alexa647-dextran 10K a second component was not necessary.

Also shown, are results for a third dye (Atto655-COOH) diffusing in water. The DC of this dye has been determined in water [17], allowing us to use this data to test the accuracy of our method. Our estimate of  $454\pm 3 \mu\text{m}^2/\text{s}$  obtained at  $26^\circ$  is in good agreement with published data for Atto655-COOH:  $426\pm 6 \mu\text{m}^2/\text{s}$  obtained at  $25^\circ$  [17] after correcting for the temperature difference.

On Fig.8 results for ATTO633-ATP and Alexa647-dextran 10K are presented graphically. From here the effect of anisotropy of diffusion and the reduction experienced by ATTO633-ATP and Alexa647-dextran 10K can be seen.

### 3.3 CONCLUSIONS

The most striking result of this study is the fact that the DC of ATTO633-ATP is reduced more than that of Alexa647-dextran 10K when comparing diffusion in

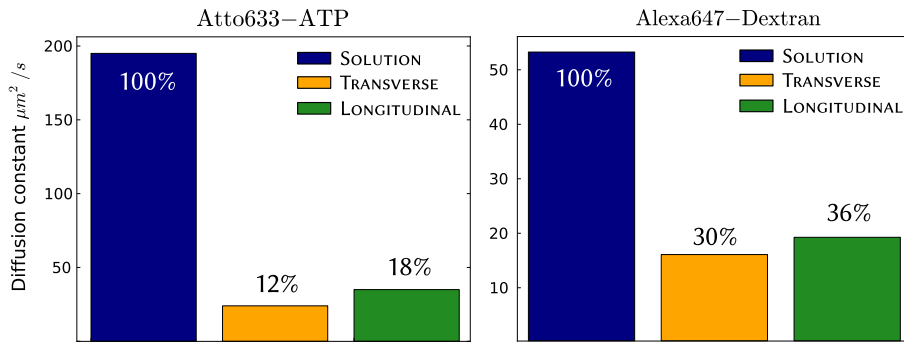


**Figure 8** – Diffusion coefficients of ATTO633-ATP and Alexa647-dextran 10K in solution and cardiomyocyte. The percentages show the DCs relative to DC in solution.

CM and solution. This is visualized in Fig.9 where the ratio of DC of ATTO633-ATP to that of Alexa647-dextran 10K is shown. As can be seen, the more than 3 time difference in solution is reduced to less than 2 in the cytoplasm, indicating that the diffusion of the smaller molecule (ATTO633-ATP) is hindered more than that of the larger one (Alexa647-dextran 10K). This is unexpected, as relative decrease of DC is usually larger for larger molecules [18].

Secondly, longer viability of the cardiomyocytes during the duration of the experimental protocol indicates that the employed “poking” technique is a good alternative to saponin permeabilization. The drawback of the method is that it is time consuming and requires more specialized equipment than is needed when using saponin permeabilization. Furthermore, depending on how well the cells attach to the laminin coated coverslip, several cells might need to be poked before the procedure is successful and a permeated CM is obtained for performing RICS measurements. A different approach of localized permeabilization can be used as

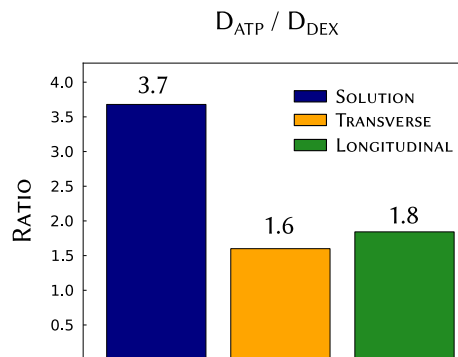


**Figure 9** – Ratio of DCs of ATTO633-ATP and Alexa647-dextran 10K in solution and in the transverse and longitudinal directions of the cell.

well. In this approach saponin is applied locally by a micropipette in only one region of the cardiomyocyte [1], whereby only a section of the cell is exposed and permeabilized. However, this would require extra equipment in addition to that used in the “poking” procedure.

Lastly, increasing the amount of physical phenomena taken into account when deriving the theoretical correlation function increases the ability of the theoretical fit to match experimental data. Addition of anisotropic diffusion, two diffusing components of the same dye and triplet state dynamics to the CF as demonstrated in Chapter 2 increases the ability to produce consistent DC estimations. Naturally, care has to be taken to avoid overparameterizing the theoretical model used for fitting experimental data. Additions to the theoretical CF are made only in cases when the physical process being observed warrants it. For example, when fitting Alexa647-dextran 10K data from cardiomyocytes, a single component model is used instead of a two component one, since the underlying physical process is deduced to be of only one species of Alexa647-dextran 10K diffusing.



---

## NUMERICAL SIMULATIONS OF RESTRICTED DIFFUSION

---

**I**N GENERAL, THE DIFFUSION COEFFICIENT of a smaller molecule is reduced less during the transition from solution to the cytosol than the DC of a larger molecule [26]. For example, if we consider the diffusion restrictions imposed by actomyosin, then the larger molecule, such as Alexa647-dextran 10K, would not be able to pass through some of the openings in the spatial structure which are traversable to smaller molecules such as ATTO633-ATP. This would result, predictably, in the DC of Alexa647-dextran 10K being reduced more in the cytosol than ATTO633-ATP. However, as can be seen from our experimental results from Chapter 3, the DC of the smaller molecule is reduced more in transition from solution to CM cytosol compared to the larger molecule. As shown by earlier modelling studies of respiration kinetics, diffusion in CMs could be restricted by local barriers [23, 30]. We explored this possibility by testing whether simple planar permeable barriers could restrict diffusion of fluorescent dyes to the extent established from experiments shown in Chapter 3.

### 4.1 COMPUTATIONAL MODEL SETUP

A stochastic computational model of diffusion was used to perform RICS experiments *in silico*.

Full details of the mathematical model are presented in Publication III. In short, the model consisted of a lattice of permeable barriers separated from each other by a certain distance (as depicted on Fig.10). Fluorescent dye molecules diffuse in the inter-barrier space (IBS) with a DC that is reduced compared to the DC in solution by a factor  $\lambda$  (i.e.,  $DC_{IBS} = \lambda \cdot DC_{solution}$ ). Barrier permeability (resulting from  $\eta$  pores of radius  $R$  nm per  $\mu m^2$  of barrier area) and barrier-to-barrier distance ( $d$ ), as well as the reduction of the DC in the inter barrier space ( $\lambda$ ) were parameters which were estimated with the aid of the computational model. Parameters were allowed to be different in different spatial directions (longitudinal - L and transverse - TR).

Together with simulating stochastic diffusion, the model generated images similar to those obtained from confocal microscopy experiments. RICS analysis was applied to these images and apparent DCs estimated. The apparent DC determined by RICS is the result of molecules diffusing in the inter-barrier space and interacting with the permeable barriers. A collection of apparent ATTO633-ATP DCs obtained from modelling are presented in Fig.11A. The dependence of the apparent DC estimated from the model is plotted as a function of barrier-to-barrier distance for various barrier permeability values. It can be seen that as barrier permeability increases, the effect of the barriers on the apparent DC decreases. Since the actual DC was estimated from experiments on cardiomyocytes as presented in Chapter 3, it is possible to find at which barrier-to-barrier distance and barrier permeability values the model produces the same apparent DC as the experiment. It is helpful to explain the procedure in terms of intersections on plots in parameter space. For this, the experimentally estimated DC is plotted on the graph of model results (the horizontal line  $D_{TR}^{exp}$  in Fig.11A). At points where model result curves and the line representing the experimental value intersect, the model yields the experimentally obtained DC. For clarity the intersection region is mag-

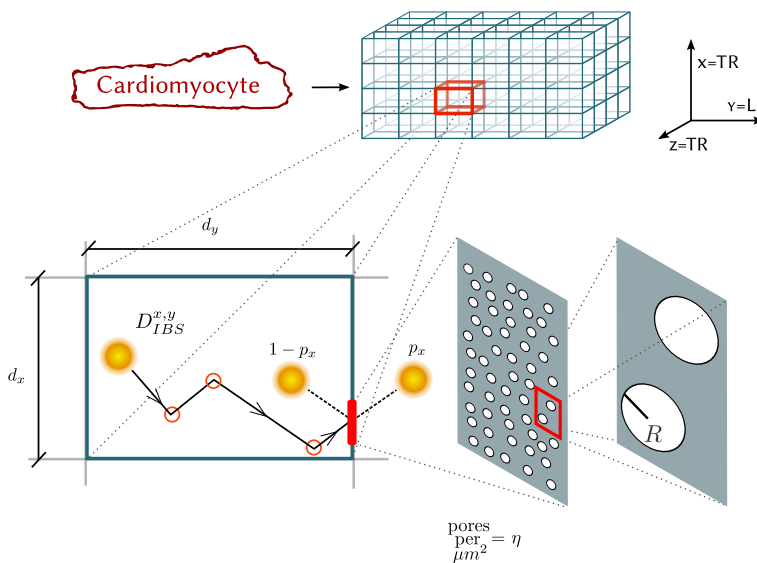


**Figure 10** – Scheme of the computational model. Intracellular structure of the cell (top left) is approximated by a 3D lattice of barriers which hinder molecule diffusion (top right). Barriers are placed, depending on direction  $\alpha$ ,  $d_\alpha$   $\mu\text{m}$  apart and have permeabilities  $p_\alpha$ . Diffusion coefficient in the space between barriers is reduced by a factor  $\lambda$  compared to solution ( $0 < \lambda \leq 1$ ). Stochastically diffusing molecules interact with barriers and have a probability  $p_\alpha$  of passing through (bottom left). Permeable barriers correspond to porous walls with  $\eta$  pores of radius  $R$  per  $\mu\text{m}^2$  of barrier area (bottom right). Apparent diffusion coefficients are estimated over the entire lattice by employing RICS analysis on images acquired from the model.

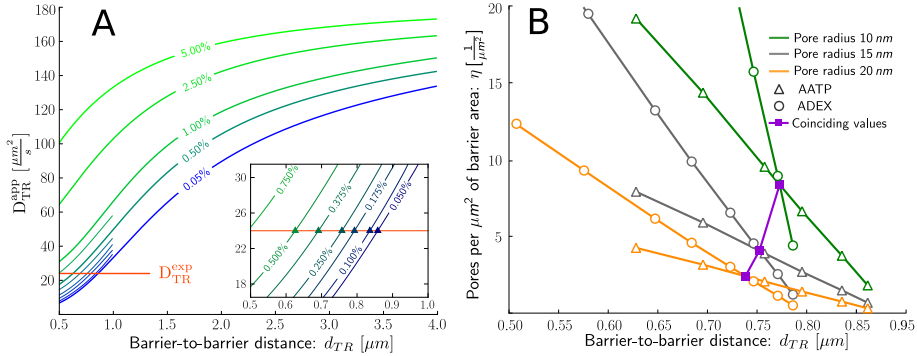


**Figure 11** – (A) Apparent diffusion constant values for ATTO633-ATP are obtained from simulations with varying barrier distances (horizontal axis) and permeabilities (indicated by values on curves). Horizontal solid line shows ATTO633-ATP diffusion coefficient estimated from experiment ( $D_{TR}^{exp}$ ). Inset covers the region  $0.5 \dots 1 \mu m$  where curves intersect with experimental data. Intersection points are marked with triangles. (B) Points of intersection from A with permeability converted to pores per  $\mu m^2$  for different pore radius values (10, 15 and 20 nm). Intersections of ATTO633-ATP ( $\Delta$ ) and Alexa647-dextran 10K (O) curves of identical pore radius values signify points where model and experiment coincide for both molecules simultaneously (■). Intersections are curves in 3D space (barrier-to-barrier distance vs. pore radius vs. pores per  $\mu m^2$ ).

nified in the inset of Fig.11A. The same procedure is performed for Alexa647-dextran 10K with the experimentally determined DC of Alexa647-dextran 10K in CM used for finding intersections.

As a result of this we obtain a set of barrier-to-barrier, permeability value pairs for both ATTO633-ATP and Alexa647-dextran 10K at which the computational model of restricted diffusion yields experimentally obtained DCs. As explained in Publication III, barrier permeability values for ATTO633-ATP and Alexa647-dextran 10K are not directly comparable. It is possible, however, to convert from barrier permeability to the number of pores per unit barrier area ( $\eta$ ) by fixing a certain pore radius ( $R$ ). These two parameters are independent of the diffusing dye, allowing the model parameter values obtained for ATTO633-ATP and Alexa647-dextran 10K to be compared. This is done by plotting them together for different pore radius values (Fig.11B). At points where ATTO633-ATP and Alexa647-dextran 10K curves intersect, the computational model is able to reproduce the experimentally estimated DCs for both ATTO633-ATP and Alexa647-dextran 10K simultaneously. From Fig.11B it is possible to establish the range of parameters ( $d$ ,  $\eta$ ,  $R$ ) at which the model is able to match results from experiments on cardiomyocytes.

Model parameter	Direction			
	transverse TR (x,z)		longitudinal L (y)	
	min	max	min	max
Distance d [ $\mu\text{m}$ ]	$0.68 \pm 0.10$	$0.87 \pm 0.07$	$0.73 \pm 0.13$	$1.02 \pm 0.10$
Pore radius R [nm]	$7.4 \pm 2.1$	$30 \pm 8$	$6.7 \pm 1.8$	$38 \pm 10$
Pore density $\eta$ [ $1/\mu\text{m}^2$ ]	$1.2 \pm 0.1$	$29 \pm 23$	$1.1 \pm 0.1$	$48 \pm 37$
$\lambda^{\text{AATP}}$	$0.78 \pm 0.13$	1.0	$0.78 \pm 0.13$	1.0
$\lambda^{\text{ADEX}}$	$0.77 \pm 0.14$	1.0	$0.77 \pm 0.14$	1.0

**Table 2** – Properties of barriers restricting diffusion predicted by stochastic model on the basis of RICS measurements. Data presented is mean $\pm$ standard deviation.

#### 4.2 BARRIER PROPERTIES ESTIMATED FROM COMPUTATIONAL MODEL

The ranges collected from intersections in Fig.11B represent parameter values where both ATTO633-ATP and Alexa647-dextran 10K are able to simultaneously match experimental DCs and are presented as the results from the computational model in Table 2. In general, barriers need to be spaced  $\sim 1 \mu\text{m}$  from each other, have a small number of nanometer scale pores, and the DC in the inter-barrier should be comparable to DC in solution in order for the model to reproduce experimental results.

Errors for the model parameters were estimated by Monte Carlo simulation outlined in the Supporting Material of Publication III. Since the minimal and maximal values of some of the parameters do not follow a normal distribution, the mean and standard deviation values are less informative than the shape of the actual distribution for which the Supporting Material of Publication III should be consulted.

#### 4.3 CONCLUSIONS

The stochastic model for simulating restricted diffusion with regular permeable barriers can match experimentally found DCs for ATTO633-ATP and Alexa647-dextran 10K in the case when:

- barriers in the model are located relatively close to each other ( $<1 \mu\text{m}$  apart)

- permeability of these barriers is relatively low (containing  $\sim 1 \dots 40$  pores of radius  $7 \dots 30$  nm per  $\mu\text{m}^2$ )
- the DC in the inter-barrier space is lower than that of diffusion in solution by a factor  $0.8 \dots 1$ .

Diffusional anisotropy results in the ranges of the parameters differing slightly in different spatial directions as visible from Table 2.

The choice of model geometry employed here, whereby regularly placed semi-permeable barriers cause restrictions to diffusion, is not the only geometry that can explain the paradoxical result where a smaller molecule is restricted more than a larger one. Our model setup was motivated by its relative simplicity compared to more complex geometries. Although already this simple geometry was able to give an answer to the raised question, more complicated model geometries with sub-volumes excluding the larger dye could be explored in the future.



---

## ONE-DIMENSIONAL COMPUTATIONAL RICS

---

ACCORDING TO OUR ANALYSIS, profound barriers to diffusion exist in cardiomyocytes. To test whether it is possible to localize such diffusion obstacles in RICS measurements we again turned to mathematical modelling.

### 5.1 MOTIVATION & MODEL SETUP

So far in this dissertation, RICS analysis has been performed and DCs estimated from the entire region acquired in either experiment or computational model. Here, a different approach is used. One-dimensional RICS simulations are performed as previously (see Chapter 4 and Publication III). Two barrier-to-barrier distances (5 and 1  $\mu\text{m}$ ) and several barrier permeabilities ( $p$ ) ranging from 0 to 75% are used as model parameters. Molecules diffuse in the inter-barrier space with a given DC ( $D_{\text{IBS}}$ ) in one dimension. When coming in contact with a barrier they can either pass through the barrier or bounce back. The probability of doing either is determined by the permeability of the barrier. The computational model produces linescan images of a 20  $\mu\text{m}$  region. In subsequent processing the region is divided into smaller subregions and RICS analysis is performed on each of these independently and apparent DCs found ( $D_{\text{app}}$ ). For comparison, analysis on the whole 20  $\mu\text{m}$  region is performed also, similarly to the analysis in Chapter 4.

### 5.2 BARRIER EFFECTS ON REGIONAL DIFFUSION COEFFICIENTS

From performing the regional analysis described above, a sequence of DCs can be obtained. An example of simulation and regional analysis results is presented on Fig. 12. Here, the DC in the IBS is set to  $D_{\text{IBS}} = 40 \mu\text{m}^2/\text{s}$  and within the 20  $\mu\text{m}$  space there are 4 barriers restricting diffusion, placed at 5  $\mu\text{m}$  from each other. The permeabilities of these barriers are varied in order to study the effect of permeability on the estimated apparent DCs obtained from RICS analysis. Results

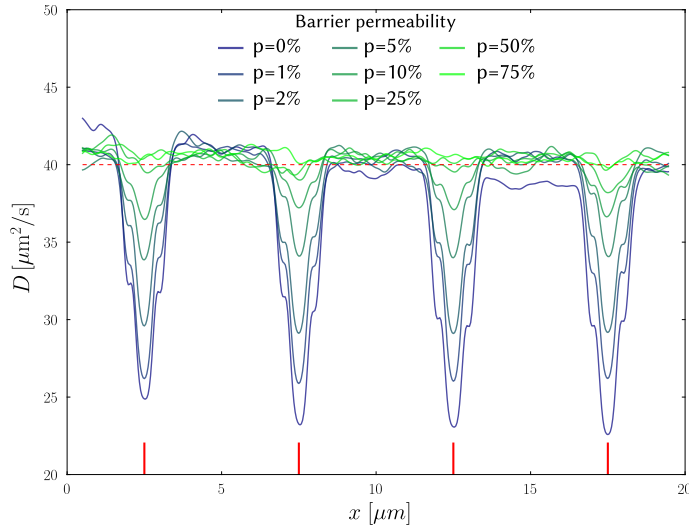


**Figure 12** – DCs obtained from regional RICS analysis of linescan data obtained from a computational model. Barriers (indicated by short vertical lines) are places 5  $\mu\text{m}$  apart and their permeability( $p$ ) is varied between model runs. DCs obtained for varying permeability values are shown with different lines. The value shown at any  $x$  location is the DC obtained from RICS analysis on the 1  $\mu\text{m}$  segment centered at that location.

obtained for a range of barrier permeability values are represented by different curves in Fig. 12. It is visible that the apparent DC reduces almost twofold in regions with a barrier in the center.

The relative decrease in DC ( $\Delta^D/D_{\text{IBS}} = (D_{\text{IBS}} - D_{\text{APP}})/D_{\text{IBS}}$ ), calculated for the region around a single barrier is averaged for equivalent neighbourhoods around each barrier and the curves shown in Fig. 13A are obtained. The solid horizontal line indicates the position of the barrier, dashed lines show the 5  $\mu\text{m}$  region centered at the barrier. It can be seen from the plot that even in cases when the region used for RICS estimation does not include the barrier (i.e., any point outside of the dashed lines), the barrier still affects the DC.

A similar analysis for a model with barriers separated by 1  $\mu\text{m}$  is shown on Fig. 13B. In this case the region used for RICS analysis is limited to 1  $\mu\text{m}$  but is plotted on the same scale as Fig. 13A to make comparison easier. Compared to the 5  $\mu\text{m}$  barrier distances on Fig. 13A, the presence of more closely placed barriers causes a decrease in the apparent DC further away from the barrier.

When the maximum relative decrease of DC relative to the DC in IBS is calculated as a function of permeability, the effect of the region size used for DC estimation in RICS becomes visible. On Fig.14 curves showing the maximum relative decrease for 3 different region sizes are plotted. From here it can be seen that as the region size increases the effect barriers have on the apparent DC is lessened.

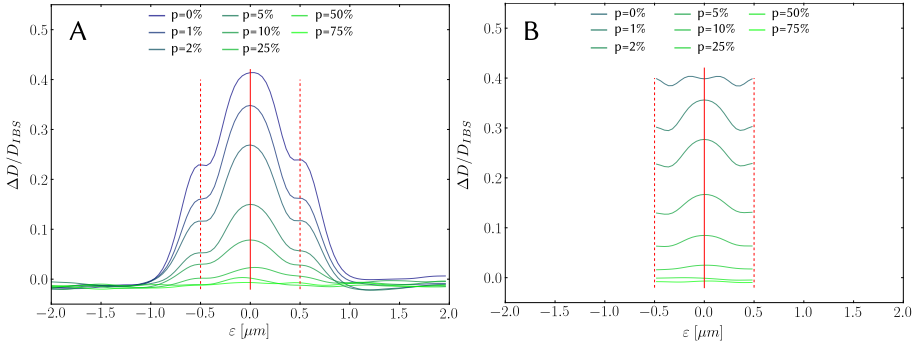


**Figure 13** – (A) Average relative decrease in DC at various barrier permeabilities in the neighbourhood around a barrier for barriers placed  $1 \mu\text{m}$  apart.  $\varepsilon$  indicates the distance of the center of the region used for DC estimation from the barrier. (B) Same as A except for barriers placed  $1 \mu\text{m}$  apart.

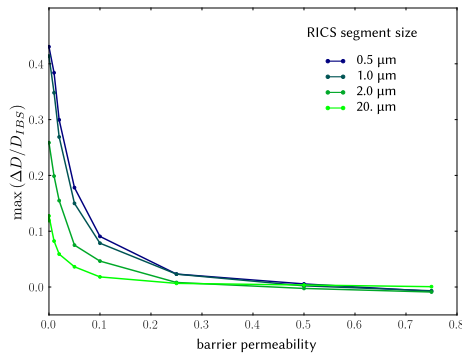


**Figure 14** – Maximum relative decrease in DC as a function of barrier permeability. Different curves indicate analysis region lengths of  $2, 1$  and  $0.5 \mu\text{m}$ . The  $20 \mu\text{m}$  region signifies analysis performed on the entire image.

When the whole image is analysed as a single  $20 \mu\text{m}$  region, the decrease in DC is reduced compared to all regional cases. Therefore, localized diffusion restrictions, represented here by barriers, result in more pronounced decreases in DCs when estimated on a smaller scale. On the large scale, however, this effect is lessened and appears as a uniform reduction in the apparent DC.

### 5.3 CONCLUSIONS

Applying RICS to 1D diffusion reveals that barriers affect estimation of DCs even if the area from which image data used for DC estimation was acquired does not contain a single barrier, but is nearby a region where a barrier is present. The distance at which this effect is observable depends on the permeability of the

barrier, the DC of the dye in the inter barrier space and the size of the segment used for apparent DC estimation.

---

## HYPERTROFIC CARDIOMYOPATHY IN RAF1 MUTANTS

---

**N**OOANAN AND LEOPARD SYNDROMES are developmental disorders characterized by distinct facial features, chest deformities, short stature and a wide array of congenital heart diseases [2]. These diseases are linked to a variety of germline gain-of-function mutations. Mutations in serine/threonine-protein kinase (RAF1) have been determined to be the cause behind 3-5% of cases of Noonan and LEOPARD syndrome in affected individuals [20]. 90-95 % of patients with Noonan RAF1 mutations exhibit hypertrophic cardiomyopathy (HCM), whereas Noonan syndrome caused by mutations in other locations often lead to different cardiac defects. This suggests an important role for RAF1 in modulation of cardiac hypertrophy. RAF1 is a serine/threonine kinase which is part of a signalling pathway involved in transducing signals from the cell membrane to the nucleus. RAF1 regulation is intricate and is affected by protein-protein interactions, localization of the protein and phosphorylation at multiple residues. In Publication II the ability of RAF1 to regulate hypertrophy in cardiomyocytes was studied.

Three common RAF1 mutations were explored in order to determine whether and how these ultimately result in hypertrophy. It was established that two of the studied mutations, S257L and L613V, localized close to phosphorylation sites S259 and S621, promote HCM. The third mutation (D486N) was found not to cause HCM. Overexpression of wild-type RAF1 also stimulated hypertrophy. Treatment with cyclosporine-A (inhibitor of calcineurin) prevented both wild-type RAF1 and L613V induced HCM.

Wild-type RAF1 overexpression and L613V both result in dysregulation of Ca<sup>2+</sup> signalling which was exemplified by spontaneous Ca<sup>2+</sup> transients, slower decay rates and, in case of L613V, an increased sarcoplasmic reticulum Ca<sup>2+</sup> load. This finding was attributed to down-regulation of sarco/endoplasmic reticulum Ca<sup>2+</sup> ATPase (SERCA) through overexpression of wild-type and L613V RAF1.

The study conducted in Publication II established a link between HCM and arrhythmogenic Ca<sup>2+</sup> dysregulation, found an interaction between calcineurin and RAF1, and identified a link for mutant RAF1 induced pathological HCM.



---

## DEVELOPMENT OF CARDIAC ENERGETICS IN POSTNATAL MOUSE HEART

---

COMPARTMENTATION OF ENERGY METABOLITES in cardiomyocytes aims to lessen the impact of abrupt changes in energy consumption and allows for high phosphorylation potential to exist where it is most required. Not much is known about the nature, structure and development of barriers responsible for such compartmentation. In the study reviewed in Publication I we summarize and comment on some of the aspects presented in a extensive investigation into how the structural and energetic properties of mouse heart muscle change during postnatal development [21].

The original paper concluded that energetic microdomains are formed very early in postnatal development and that the maturation of cellular architecture has an important role to play ensuring maximal flexibility in regulation of ATP production by mitochondria. Although an impressive amount of work had been invested by the authors of the original paper, we found several issues with the conclusions and questions left unanswered by the authors. We pointed out the misinterpretation of one derived variable used by the authors to propose an increase in the functional coupling between the adenine nucleotide translocase (ANT) and mitochondrial creatine kinase (CK). We proposed an alternative explanation of an increase in diffusion restrictions in the cytosol and suggested an experiment for measuring the coupling between ANT and mitochondrial CK. Furthermore, we used a different approach from the original authors to interpret their data and to focus on the changes of the role of energy supply pathways by eliminating auxiliary effects. We also suggested some possible directions for future research in this area. Namely, accounting for the changing role of glycolysis during maturation and employing computational models in analysing the data, which could help unravel the interplay between different factors during cell maturation.



---

## CONCLUSIONS

---

**T**HIS DISSERTATION EXPLORES VARIOUS aspects of cardiac function and dysfunction. The main conclusions deriving from this work are listed below, grouped according to the research topic.

### EXTENDED RICS TECHNIQUE

- a) The extended RICS protocol developed during these doctoral studies is a useful tool for determining concentrations, diffusion coefficients and diffusional anisotropy of fluorescent dyes in cells.
- b) The RICS method, when applied to estimating diffusion in water, is able to reproduce the known DCs of the dye ATTO655-COOH with high accuracy.
- c) The “poking” technique is a good alternative to saponin permeabilization. It requires dedicated hardware in form of controllable micromanipulators and extra preparation in order to ensure cells remain on the coverslip after mechanical permeabilization. However in cases like anisotropic RICS measurements, where one protocol run can take several hours, good viability of cells is a necessity.
- d) Taking into account the possibility of fluorescent molecules entering into a triplet state enhanced the ability of the method to estimate DCs.
- e) Assuming two sub-species of the same dye to be diffusing in the cytosol, one slowly diffusing bound form and one freely diffusing form improved the results greatly when estimating DCs of ATTO633-ATP. In case of Alexa647-dextran 10K adding a second component was not necessary and did not improve fits to CF curves. This indicates that ATTO633-ATP is more actively binding to intracellular proteins or structures, whereas Alexa647-dextran 10K remains relatively inert.

## CONCLUSIONS

### ESTIMATION OF DIFFUSION COEFFICIENTS OF FLUORESCENT DYES

- f) Employing the RICS method, DCs of ATTO633-ATP were determined to be  $326\pm 13$ ,  $195\pm 8$ ,  $24\pm 6$ ,  $35\pm 8$   $\mu\text{m}^2/\text{s}$  in water, artificial intracellular solution, transverse direction and longitudinal direction in the cardiomyocyte, respectively. Similarly, DCs of Alexa647-dextran 10K were determined to be  $62\pm 1$ ,  $53\pm 1$ ,  $16\pm 2$ ,  $19\pm 3$   $\mu\text{m}^2/\text{s}$  in water, artificial intracellular solution, transverse direction and longitudinal direction in the cardiomyocyte, respectively.
- g) The relative decline in DCs when transitioning from solution to the intracellular environment was higher for ATTO633-ATP than for Alexa647-dextran 10K. Considering the fact that the molecular mass of ATTO633-ATP is  $\sim 9$  times less than that of Alexa647-dextran 10K makes this result counterintuitive, whereby a smaller molecule is hindered more in the cytosol than the larger one.

### MATHEMATICAL MODELLING OF RESTRICTED DIFFUSION

- h) The stochastic model of restricted diffusion with regular permeable barriers is able to reproduce the experimentally found DCs for ATTO633-ATP and Alexa647-dextran 10K when: barriers in the model are placed relatively close  $< 1$   $\mu\text{m}$  apart, permeability of these barriers is low (containing  $\sim 1 \dots 40$  pores of radius  $7 \dots 30$  nm per  $\mu\text{m}^2$ ), diffusion coefficient in the inter barrier space is lower than diffusion in solution by a factor  $0.8 \dots 1$ .
- i) The model geometry used in this work is not the only one that is able to reproduce experimentally obtained DCs. Our choice was motivated by the relative simplicity of the employed geometry of the model.
- j) Computational experiments applying RICS to 1D diffusion reveal that barriers affect estimation of DCs even if the region used for estimation does not contain a barrier itself but is close to one. The distance at which this effect is observable depends on the permeability of the barrier, the DC of the dye in the inter barrier space and the size of the segment used for apparent DC estimation.

### CARDIOMYOCYTE HYPERTROPHY IN NOONAN SYNDROME

- k) The study conducted in Publication II established a link between hypertrophic cardiomyopathy (HCM) and overexpression or mutation of serine/threonine-

protein kinase. Both wild-type and L613V RAF1 signal through calcineurin to induce hypertrophy in affected cardiomyocytes.

- l) RAF1 impairs calcium signalling by down-regulating SERCA but does not affect expression levels of other proteins involved in intracellular calcium signalling.
- m) Wild-type RAF1 overexpression and L613V both result in arrhythmogenic dysregulation of calcium signalling, indicated by spontaneous calcium transients during electrical stimulation, slower decay rates and, in case of L613V, an increased sarcoplasmic reticulum calcium load.
- n) Treatment with cyclosporine-A prevented both wild-type RAF1 and L613V induced HCM.

#### DEVELOPMENT OF ENERGETIC MICRODOMAINS

- o) Regeneration of energy metabolites through glycolysis is an important factor, especially during maturation, and should be included in the analysis of developmental changes in energy transfer pathways.
- p) Computational models could help interpret existing data and could reveal novel aspects of the interplay between various factors during cell maturation. Using statistical methods, different mathematical models could be compared to establish the existence of metabolite pools or compartmentation in the CM.



## BIBLIOGRAPHY



---

## BIBLIOGRAPHY

---

- [1] M. R. Abraham, V. Selivanov, D. Hodgson, D. Pucar, L. Zingman, B. Wieringa, P. Dzeja, A. Alekseev, and A. Terzic. Coupling of cell energetics with membrane metabolic sensing. *J. Biol. Chem.*, 277(27):24427–24434, 2002.
- [2] J. E. Allanson. Noonan syndrome. *J. Med. Genet.*, 24(1):9, 1987.
- [3] C. M. Brown, R. B. Dalal, B. Hebert, M. A. Digman, A. R. Horwitz, and E. Gratton. Raster image correlation spectroscopy (RICS) for measuring fast protein dynamics and concentrations with a commercial laser scanning confocal microscope. *J. Microsc.*, 229(1):78–91, 2008.
- [4] R. de Graaf, A. van Kranenburg, and K. Nicolay. In vivo  $^{31}\text{P}$ -NMR diffusion spectroscopy of ATP and phosphocreatine in rat skeletal muscle. *Biophys. J.*, 78(4):1657–1664, 2000.
- [5] D. Del Re and J. Sadoshima. Is RAF1 a nexus for cardiac hypertrophic signaling in human disease? *J. Mol. Cell. Cardiol.*, 51(1):1–3, 2011.
- [6] M. Digman, C. Brown, P. Sengupta, P. Wiseman, A. Horwitz, and E. Gratton. Measuring fast dynamics in solutions and cells with a laser scanning microscope. *Biophys. J.*, 89(2):1317–1327, 2005.
- [7] M. A. Digman and E. Gratton. Lessons in fluctuation correlation spectroscopy. *Annu Rev Phys Chem*, 62:645–668, 2011.
- [8] N. Gröner, J. Capoulade, C. Cremer, and M. Wachsmuth. Measuring and imaging diffusion with multiple scan speed image correlation spectroscopy. *Opt. Express*, 18(20):21225, 2010.
- [9] S. Gudbjarnason, P. Mathes, and K. G. Ravens. Functional compartmentation of ATP and creatine phosphate in heart muscle. *J. Mol. Cell. Cardiol.*, 1(3):325–339, 1970.
- [10] E. Haustein and P. Schuille. Fluorescence correlation spectroscopy: novel variations of an established technique. *Annu. Rev. Biophys. Biomol. Struct.*, 36:151–169, 2007.

## Bibliography

- [11] A. Kaasik, V. Veksler, E. Boehm, M. Novotova, A. Minajeva, and R. Ventura-Clapier. Energetic crosstalk between organelles: Architectural integration of energy production and utilization. *Circ. Res.*, 89(2):153–159, 2001.
- [12] O. Krichevsky and G. Bonnet. Fluorescence correlation spectroscopy: the technique and its applications. *Reports on Prog. Phys.*, 65(2):251, 2002.
- [13] L. Kümmel. Ca,Mg-ATPase activity of permeabilized rat heart cells and its functional coupling to oxidative phosphorylation of the cells. *Cardiovasc. Res.*, 22:359–367, 1988.
- [14] F. T. Kurz, M. A. Aon, B. O'Rourke, and A. A. Armoundas. Spatio-temporal oscillations of individual mitochondria in cardiac myocytes reveal modulation of synchronized mitochondrial clusters. *Proc. Natl. Acad. Sci.*, 107(32):14315, 2010.
- [15] M. J. Kushmerick and R. J. Podolsky. Ionic mobility in muscle cells. *Science (80-)*, 166(910):1297–1298, 1969.
- [16] J. Lakowicz. *Principles of fluorescence spectroscopy*. Springer, 2006.
- [17] C. B. Müller, A. Loman, V. Pacheco, F. Koberling, D. Willbold, W. Richter, and J. Enderlein. Precise measurement of diffusion by multi-color dual-focus fluorescence correlation spectroscopy. *EPL (Europhysics Letters)*, 83:46001, 2008.
- [18] N. Muramatsu and A. Minton. Tracer diffusion of globular proteins in concentrated protein solutions. *Proc. Natl. Acad. Sci.*, 85(9):2984 –2988, 1988.
- [19] S. Neubauer. The failing heart—an engine out of fuel. *N. Engl. J. Med.*, 356(11):1140–1151, 2007.
- [20] B. Pandit, A. Sarkozy, L. A. Pennacchio, C. Carta, K. Oishi, S. Martinelli, E. A. Pogna, W. Schackwitz, A. Ustaszewska, A. Landstrom, and Others. Gain-of-function RAF1 mutations cause Noonan and LEOPARD syndromes with hypertrophic cardiomyopathy. *Nat. Genet.*, 39(8):1007–1012, 2007.
- [21] J. Piquereau, M. Novotova, D. Fortin, A. Garnier, R. Ventura-Clapier, V. Veksler, and F. Joubert. Postnatal development of mouse heart: formation of energetic microdomains. *J. Physiol. (Lond.)*, 588(13):2443–2454, 2010.
- [22] H. Ramay, O. Liu, and E. Sobie. Recovery of cardiac calcium release is controlled by sarcoplasmic reticulum refilling and ryanodine receptor sensitivity. *Cardiovasc. Res.*, 91(4):598 –605, 2011.

- [23] H. Ramay and M. Vendelin. Diffusion restrictions surrounding mitochondria: A mathematical model of heart muscle fibers. *Biophys. J.*, 97(2):443–452, 2009.
- [24] V. Saks, A. Kuznetsov, T. Andrienko, Y. Usson, F. Appaix, K. Guerrero, T. Kaambre, P. Sikk, M. Lemba, and M. Vendelin. Heterogeneity of ADP diffusion and regulation of respiration in cardiac cells. *Biophys. J.*, 84(5):3436–3456, 2003.
- [25] M. Sepp, M. Vendelin, H. Vija, and R. Birkedal. ADP compartmentation analysis reveals coupling between pyruvate kinase and ATPases in heart muscle. *Biophys. J.*, 98(12):2785–2793, 2010.
- [26] P. Shorten and J. Sneyd. A mathematical analysis of obstructed diffusion within skeletal muscle. *Biophys. J.*, 96(12):4764–4778, 2009.
- [27] M. Tartaglia, L. A. Pennacchio, C. Zhao, K. K. Yadav, V. Fodale, A. Sarkozy, B. Pandit, K. Oishi, S. Martinelli, W. Schackwitz, and Others. Gain-of-function SOS1 mutations cause a distinctive form of Noonan syndrome. *Nat. Genet.*, 39(1):75–79, 2006.
- [28] Nancy Thompson. Fluorescence correlation spectroscopy. In Joseph Lakowicz, Chris D. Geddes, and Joseph R. Lakowicz, editors, *Topics in Fluorescence Spectroscopy*, volume 1 of *Topics in Fluorescence Spectroscopy*, pages 337–378. Springer US, 2002.
- [29] M. Vendelin and R. Birkedal. Anisotropic diffusion of fluorescently labeled ATP in rat cardiomyocytes determined by raster image correlation spectroscopy. *Am. J. Physiol. Cell. Physiol.*, 295(5):C1302–1315, 2008.
- [30] M. Vendelin, M. Eimre, E. Seppet, N. Peet, T. Andrienko, M. Lemba, J. Engelbrecht, E. Seppet, and V. Saks. Intracellular diffusion of adenosine phosphates is locally restricted in cardiac muscle. *Mol. Cell. Biochem.*, 256(1/2):229–241, 2004.
- [31] J. Widengren, U. Mets, and R. Rigler. Fluorescence correlation spectroscopy of triplet states in solution: a theoretical and experimental study. *J Phys Chem*, 99(36):13368–13379, 1995.



## CURRICULUM VITAE



# Curriculum Vitae

## ARDO ILLASTE

### PERSONAL INFORMATION

---

Date of birth: 22.06.1982  
Nationality: Estonian  
Email: ardo@sysbio.ioc.ee

### EDUCATION

---

- PhD student in engineering physics, Tallinn University of Technology, Estonia  
“Determination of Restrictions to Diffusion in Cardiomyocytes” 2008 – 2012  
(currently in progress of graduating)
- Master of Natural Sciences *cum laude*, Engineering physics – “Mathematical Model of Mitochondrial Energy Metabolism”, Tallinn University of Technology 2007
- Bachelor of Natural Sciences, Engineering physics – “Cellular Automata Model of Heart Muscle”, Tallinn University of Technology 2006
- Secondary education, Tallinn English College, Estonia 2000

### RESEARCH EXPERIENCE

---

**Dr. Marko Vendelin** – Laboratory of Systems Biology, Institute of Cybernetics, Tallinn University of Technology, Estonia: Analysis of diffusion restrictions in cardiomyocytes. Experiments of confocal microscope and modeling. PhD studies 2008-2011

**Dr. Eric A. Sobie** – Department of Pharmacology and Systems Therapeutics, Mount Sinai School of Medicine, New York, USA: Calcium handling in cardiac myocytes derived from human embryonic stem cells. Performed experiments on location in New York, USA from January to August 2009 and in October 2010

### INTERNATIONAL SCIENTIFIC CONFERENCES

---

- Biophysical Society Annual Meeting, USA, posters – 2012, 2011, 2010, 2009, 2008
- 64<sup>th</sup> Harden Conference on Mitochondrial Physiology, Ambleside, UK, poster - 2007

### SCHOLARSHIPS & AWARDS

---

- DoRa scholarship from 10.2010 – 11.2010 for conducting experiments in Mount Sinai School of Medicine, New York, USA
- Archimedes scholarship from 01.2009 – 08.2009 for exchange research scholar position in Mount Sinai School of Medicine, New York, USA
- Archimedes / DoRa travel awards for attending conferences in 2007, 2008, 2010, 2012

### PUBLICATIONS

---

- Ardo Illaste, Mari Kalda, David W. Schryer, and Mervi Sepp, **Life of mice – development of cardiac energetics**, *The Journal of Physiology*, December 1, 2010 588 (23) 4617-461
- Perundurai S. Dhandapany, Frank Fabris, Rahul Tonk, Ardo Illaste, Ioannis Karakikes, Mehran Sorourian, Jipo Sheng, Roger J. Hajjar, Marco Tartaglia, Eric A. Sobie, Djamel Lebeche, Bruce D. Gelb, **Cyclosporine attenuates cardiomyocyte hypertrophy induced by RAF1 mutants in Noonan and LEOPARD syndromes**, *Journal of Molecular and Cellular Cardiology*, Volume 51, Issue 1, July 2011, Pages 4-15, ISSN 0022-2828

## Curriculum Vitae

- Ardo Illaste, Martin Laasmaa, Pearu Peterson, Marko Vendelin, **Analysis of molecular movement reveals latticelike obstructions to diffusion in heart muscle cells**, Biophysical Journal, 2012, *in press*

### TEACHING

---

- Introduction to Scientific Programming for high school students, 2008
- Seminars for beginning PhD students on basics of biochemistry, bioenergetics and biophysics, 2008-2010

### EMPLOYMENT

---

- Introduction to Scientific Programming for high school students, 2008
- Engineer/Researcher, Institute of Cybernetics, TUT, 2006 - ...
- Research Scholar, Mount Sinai School of Medicine, 01.2009-08.2009
- Programmer, Smilehouse Baltic, 2005 – 2006
- Pioneer, Estonian Armed Forces (compulsory military service), 2003-2004

### LANGUAGES

---

Estonian (mother language), English (fluent), French, Finnish, Russian (all basic)

### COMPUTER SKILLS

---

- Day-to-day usage of C++, Python and Java programming languages for writing data analysis programs
- Competent in vector and raster image creation/manipulation programs
- Good knowledge of web frameworks: HTML, CSS, Django
- Excellent knowledge of UNIX/Linux. Capable in Windows, OSX
- Routine use of LaTeX document preparation system
- Experience with computer algebra systems: Matlab, Maple, Mathematica

## Elulookirjeldus

### ARDO ILLASTE

#### ÜLDINFO

---

Sünniaeg: 22.06.1982  
Rahvus: eesti  
Email: ardo@sysbio.ioc.ee

#### HARIDUS

---

- Doktorant, Tehniline füüsika, Tallinna Tehnikaülikool, “Diffusioonitakistused südamelihaskudedes” 2008 – 2012
- Loodusteaduste magister *cum laude*, Tehniline füüsika – “Mitokondriaalse energiavahetuse matemaatiline mudel”, Tallinna Tehnikaülikool, 2007
- Loodusteaduste bakalaureus, Tehniline füüsika – “Südamelihase modelleerimine rakuautomaatidega”, Tallinna Tehnikaülikool, 2006
- Keskharidus, Tallinna Inglise Kolledž, 2000

#### TEADUSTÖÖ KOGEMUS

---

**Dr. Marko Vendelin** – Süsteemibioloogia labor, TTÜ Küberneetika Instituut: Diffusioonitakistuste uurimine südamelihaskudedes. Katsed konfokaalmikroskoobiga ja numbriline modelleerimine. Doktoriröpingud 2008-2012

**Dr. Eric A. Sobie** – Farmakoloogia teaduskond, Mount Sinai School of Medicine, New York, USA: Kaltsiumiringlus tüvirakkudest tuletatud südamelihaskudedes ja Noonani sündroomiga hüpertroofsetes südamelihaskudedes. Eksperimentaaltöö konfokaalmikroskoobiga. 01.2009 -08.2009 ja 10.2010

#### ETTEKANDED RAHVUSVAHELISTEL KONVERENTSIDEL

---

- Annual Meetings of the Biophysical Society, USA, postriid – 2011, 2010, 2009, 2008
- Harden Conference on Mitochondrial Physiology, Ambleside, UK, poster - 2007

#### STIPENDIUMID

---

- DoRa stipendium 10.2010 – 11.2010 lisaeksperimentide sooritamiseks, Mount Sinai School of Medicine, New York, USA
- Archimedese stipendium 01.2009 – 08.2009, külalisteadur (exchange research scholar), Mount Sinai School of Medicine, New York, USA
- Archimedes / DoRa stipendiumid konverentsidel osalemiseks 2007, 2008, 2010, 2012

#### PUBLIKATSIOONID

---

- Ardo Illaste, Mari Kalda, David W. Schryer, and Mervi Sepp, **Life of mice – development of cardiac energetics**, The Journal of Physiology, December 1, 2010 588 (23) 4617-461
- Perundurai S. Dhandapany, Frank Fabris, Rahul Tonk, Ardo Illaste, Ioannis Karakikes, Mehran Sorourian, Jipo Sheng, Roger J. Hajjar, Marco Tartaglia, Eric A. Sobie, Djamel Lebeche, Bruce D. Gelb, **Cyclosporine attenuates cardiomyocyte hypertrophy induced by RAF1 mutants in Noonan and LEOPARD syndromes**, *Journal of Molecular and Cellular Cardiology*, Volume 51, Issue 1, July 2011, Pages 4-15, ISSN 0022-2828
- Ardo Illaste, Martin Laasmaa, Pearu Peterson, Marko Vendelin, **Analysis of molecular**

## Elulookirjeldus

**movement reveals latticelike obstructions to diffusion in heart muscle cells,**  
Biophysical Journal, 2012, *in press*

### ÕPETUSTEGEVUS

---

- Sissejuhatus programmeerimisse keskkooliõpilastele, TTÜ Avatud Ülikool 2008
- Seminarid uutele doktorantidele biokeemias, bioenergeetikas ja biofüüsikas 2008-2010

### TÖÖKOGEVUS

---

- Insener/doktorant, TTÜ Küberneetika instituut, 2006 - ...
- Ajutine teadur (research scholar), Mount Sinai School of Medicine, 01.2009-08.2009
- Programmeerija, Smilehouse Baltic, 2005 – 2006
- Ajateenistus, 2003-2004

### KEELEOSKUS

---

Eesti(emakeel), inglise, prantsuse, soome, vene

### ARVUTIOSKUS

---

- C++, Python ja Java programmeerimiskeeled
- Vektor- ja rastergraafika programmid
- Interneti töövahendid: HTML, CSS, Django
- Operatsioonisüsteemid: UNIX/Linux, Windows, OSX
- LaTeX dokumentide ettevalmistussüsteem
- Matlab, Maple, Mathematica

## APPENDIX



---

PUBLICATION I

---

Illaste A, Kalda M, Schryer DW, Sepp M

**Life of mice - development of cardiac energetics.**

*Journal of Physiology*, 588(23), December 2010



## JOURNAL CLUB

**Life of mice – development of cardiac energetics**

Ardo Illaste, Mari Kalda,  
David W. Schryer and Mervi Sepp  
*Laboratory of Systems Biology, Institute  
of Cybernetics at Tallinn University of  
Technology, Akadeemia tee 21, 12618,  
Tallinn, Estonia*

Email: ardo@sysbio.ioc.ee

Production and transfer of metabolites like ATP and phosphocreatine within cardiomyocytes is crucial for the robust availability of mechanical work. In mammalian cardiomyocytes, mitochondria, the main suppliers of usable chemical energy in the form of ATP, are situated adjacent to both the ATPases near the mechanical apparatus, and the sarco(endo)plasmic reticulum  $\text{Ca}^{2+}$ -ATPase (SERCA) calcium pumps. Operation of these ATPases requires a high ATP/ADP ratio, which is maintained by two parallel energy transfer systems – creatine kinase (CK) and direct adenine nucleotide channelling (DANC). Compartmentation of energy metabolites works to lessen the impact of dynamic changes in the availability of usable energy on the operation of these ATPases, and allows for a higher phosphorylation potential where it is required most.

The operational mechanism, structure and development of the barriers responsible for energetic compartmentation within cardiomyocytes have yet to be elucidated despite intensive research in this area. A recent article in *The Journal of Physiology* by Piquereau *et al.* (2010) is an extensive investigation into how the structural and energetic properties of mouse heart muscle change during postnatal development. It includes observations on structural changes and cellular morphology using electron microscopy, quantification of mitochondrial, myofibrillar and SR proteins, assessment of organelle functionality, and the quantification of the energy flux in both the CK and DANC transfer systems. SERCA function was measured via calcium mediated tension generation, while myosin ATPase function was quantified by measuring rigor tension development. Total activity of CK and mitochondrial CK (mi-CK) were estimated.

The article by Piquereau *et al.* builds upon a strong research tradition at Inserm U769, Univ. Paris-Sud, which focuses on studying how cardiac mechanisms function in response to both pathological and physiological stimuli. This includes work on contractile, sarcoplasmic reticulum (SR), and mitochondrial proteins, membrane receptors, ion channels and signalling. Their work has inspired new areas of inquiry into the function of energy compartmentation in the heart with various implications for therapeutic targets to improve both function and clinical outcomes.

As main results of their recent publication, Piquereau *et al.* concluded that the formation of energetic microdomains occurs very early in postnatal development, and that the maturation of cellular architecture plays an important role in achieving maximal flexibility in regulation of ATP production by mitochondria. They found that the development of regulatory energetic pathways does not happen simultaneously. Throughput of energy transfer between mitochondria and myosin ATPases is correlated with the changes in the cytoarchitecture in contrast to the CK supported energy transfer which seems to depend on specific localization and expression of CK. Development between days 3 and 7 is crucial in increasing the capacity of energy transfer and involves major remodelling of the contacts between organelles. The density of intracellular organelles increases at the expense of free cytosolic space. Contacts between mitochondria and longitudinally oriented myofibrils and between SR and mitochondria are established to form an effective intracellular energetic unit. After the first week (*post natum*), a different phase of hypertrophy occurs without major structural changes to the contacts between organelles. After 3 weeks, the respiratory capacity of mitochondria increases, whereas heart weight to body weight ratio decreases. The main results of the article are summarized in Fig. 1.

Considerable effort has been invested by Piquereau *et al.* in determining various changes during cardiomyocyte maturation. Several questions arise, however, when comparing the publication with previous studies. Firstly, in 3-day-old cells, based on results from electron microscopy and

SR protein expression experiments, the authors deduce SR not to be present in quantities high enough to enable SR  $\text{Ca}^{2+}$  content measurement. However, volume measurements from electron microscopy are known to be very sensitive to sample preparation procedures, especially as dimensions of different organelles can change in different ratios as a result of fixation. The low level of SR protein expression in 3-day-old cells could be explained by results obtained in embryonic mouse cardiomyocytes (Takeshima *et al.* 1998), where SR  $\text{Ca}^{2+}$  release channels do not play a major role in excitation–contraction (EC) coupling but, instead, are required for cellular  $\text{Ca}^{2+}$  homeostasis. Full SR function develops rapidly in neonates, possibly explaining both the dramatic increase in SR  $\text{Ca}^{2+}$  content between day 3 and day 7 fibres, and the difficulty the authors had in conducting the experiment with fibres from 3-day-old mice.

Secondly, the authors concluded that the functional coupling of adenine nucleotide translocase (ANT) and mi-CK ('functional activity' in Piquereau *et al.* 2010) was considerably higher in adult myocytes. This conclusion, however, seems to be based on misinterpreting the  $K_{\text{mADP}}/K_{\text{Cr}}$  ratio graph (article Fig. 5F). As is evident from the  $K_{\text{m}}$  plots in the article (article Fig. 5E),  $K_{\text{mCr}}$  is constant throughout the ageing process, whereas  $K_{\text{mADP}}$  increases notably in older fibres. The increase in  $K_{\text{mADP}}/K_{\text{Cr}}$  ratio stems from the increase of  $K_{\text{mADP}}$  and is not, in this case, indicating increases in mi-CK–ANT coupling nor mi-CK activity. Rather, it can be interpreted as indication of an increase in diffusion restrictions to adenine nucleotides in the cytosol caused by changes in either mitochondrial outer membrane or myofibrillar and other cytosolic structures, or both (Vendelin & Birkedal, 2008; Sepp *et al.* 2010). In order to measure the coupling between mi-CK and ANT, different experimental techniques need to be employed, such as measuring changes in respiration in response to ATP titration.

Two observations can be made from further analysing SR calcium uptake and rigor tension sensitivity results from the article (article Figs 2 and 4). By looking at ratios of values obtained during different

conditions, it is possible to eliminate auxiliary effects and focus on how the role of energy supply pathways change in relation to one another as the cell matures. Two examples are given in Fig. 1 (bottom row). Firstly, from the difference in rigor tension levels ( $\Delta pMgATP_{50}$ ) supported by CK and ATP energy supply systems (Fig. 1, line b), it is evident that myosin ATPase activity supported by CK is consistently higher than exogenous ATP throughout the growing process. On the other hand, the capacity of the CK system to load the SR increases  $\sim 2$  times by day 61 (Fig. 1, line d). We suggest that this is further evidence of the role of SR transiting from maintaining  $Ca^{2+}$  homeostasis (Takeshima *et al.* 1998) to playing an essential role in EC coupling. A possible explanation for this could be activation of SR-bound CK by day 21, whereas myo-

fibril bound CK is already active from day three. Secondly,  $pMgATP_{50}(DANC) - pMgATP_{50}(ATP)$  (Fig. 1, line a) indicates that after an initial increase caused by changes in mitochondrial positioning, myofibrils stay constantly more sensitive to stimulation via direct channelling compared to exogenous ATP. At the same time, however, direct channelling is able to maintain an increasingly higher SR load than exogenous ATP (Fig. 1, line c). This can be explained by structural changes in the cell, whereby SR becomes more closely situated with respect to mitochondria (article Fig. 8D). Clearly, these interpretations should be verified through further experiments and modelling.

Building on results obtained by Piquereau *et al.* some directions could be explored in the future. One matter of interest would

be how the role of glycolysis changes during maturation. It has been shown that embryonic mouse heart responds in a similar manner to inhibition of either glycolysis or oxidative phosphorylation and that in early stages of postnatal development, ATP consumed by ion pumps is preferentially supplied through glycolysis (Chen *et al.* 2007). Additionally, in 1-day-old rabbit, 44% of consumed ATP comes from glycolysis, whereas by day 7 this goes down to 7% (Lopaschuk *et al.* 1992). In the paper under discussion, the possible contribution of glycolysis to ATP supply was not directly addressed. Especially in young mouse cells, the effect from this could be considerable and might impact some of the conclusions of the article.

Another possible area to explore in the future could be to analyse these results with the aid of a computational model.

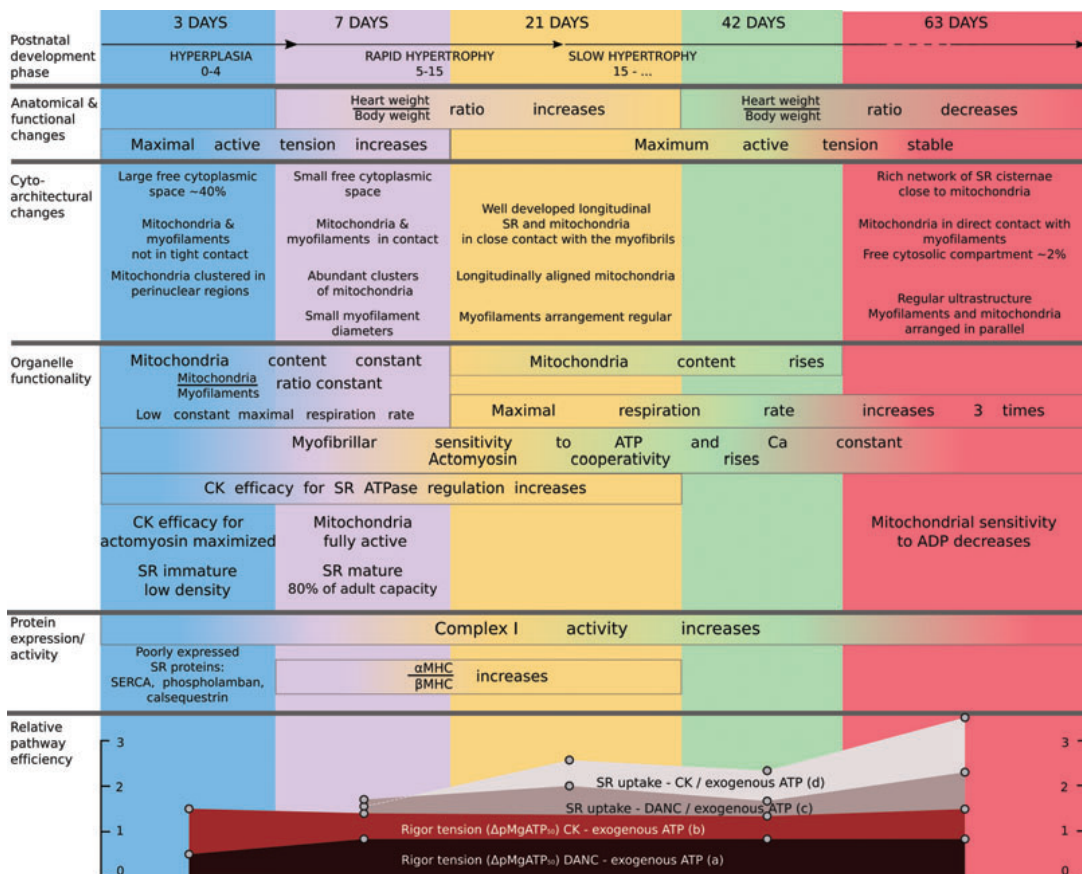


Figure 1. Summary of results from the article by Piquereau *et al.*

This would help in further unravelling the interplay between different factors during cell maturation, especially in questions where experimental methods fail to yield clear results. Different mathematical models could be compared with statistical methods in order to determine the role of various pathways and the existence of metabolite pools or spatial compartmentation in the developing cell (Sepp *et al.* 2010).

In summary, the extensive experimental work performed in the work by Piquereau *et al.* covers various aspects of energy metabolism and morphological changes in the cell during maturation. The work provides new information on postnatal development of heart energetics in mice – a popular animal model used for studying the effects of genetic manipulation.

## References

- Chen F, De Diego C, Xie L, Yang J, Klitzner T & Weiss J (2007). Effects of metabolic inhibition on conduction, Ca transients, and arrhythmia vulnerability in embryonic mouse hearts. *Am J Physiol Heart Circ Physiol* **293**, H2472–2478.
- Lopaschuk G, Collins-Nakai R & Itoi T (1992). Developmental changes in energy substrate use by the heart. *Cardiovasc Res* **26**, 1172–1180.
- Piquereau J, Novotova M, Fortin D, Garnier A, Ventura-Clapier R, Veksler V & Joubert F (2010). Postnatal development of mouse heart: formation of energetic microdomains. *J Physiol* **588**, 2443–2454.
- Sepp M, Vendelin M, Vija H & Birkedal R (2010). ADP Compartmentation analysis reveals coupling between pyruvate kinase and ATPases in heart muscle. *Biophys J* **98**, 2785–2793.
- Vendelin M & Birkedal R (2008). Anisotropic diffusion of fluorescently labeled ATP in rat cardiomyocytes determined by raster image correlation spectroscopy. *Am J Physiol Cell Physiol* **295**, C1302–C1315.
- Takehima H, Komazaki S, Hirose K, Nishi M, Noda T & Iino M (1998). Embryonic lethality and abnormal cardiac myocytes in mice lacking ryanodine receptor type 2. *EMBO J* **17**, 3309–3316.

## Acknowledgements

We are grateful to Dr Marko Vendelin and Dr Hena R. Ramay, for fruitful discussions and review of the manuscript. This work was supported by the Wellcome Trust (Fellowship No. WT081755MA) and the Estonian Science Foundation (grant No. 7344, PhD stipends for A.I., M.S. and M.K.).



---

PUBLICATION II

---

Dhandapany P, Fabris F, Tonk R, Illaste A, Karakikes I, Sorourian M, Sheng J, Hajjar R, Tartaglia M, Sobie R, Lebeche D, Gelb B

**Cyclosporine attenuates cardiomyocyte hypertrophy induced by RAF1 mutants in Noonan and LEOPARD syndromes.**

*Journal of Molecular and Cellular Cardiology*, Volume 51, Issue 1, July 2011





## Original article

## Cyclosporine attenuates cardiomyocyte hypertrophy induced by RAF1 mutants in Noonan and LEOPARD syndromes

Perundurai S. Dhandapany<sup>a</sup>, Frank Fabris<sup>b</sup>, Rahul Tonk<sup>d</sup>, Ardo Illaste<sup>b</sup>, Ioannis Karakikes<sup>c</sup>, Mehran Sorourian<sup>a</sup>, Jipo Sheng<sup>c</sup>, Roger J. Hajjar<sup>c</sup>, Marco Tartaglia<sup>e</sup>, Eric A. Sobie<sup>b</sup>, Djamel Lebeche<sup>c,\*</sup>, Bruce D. Gelb<sup>a,\*</sup>

<sup>a</sup> Departments of Pediatrics and Genetics and Genomic Sciences and the Child Health and Development Institute, Mount Sinai School of Medicine, One Gustave L. Levy Place, New York, NY 10029, USA

<sup>b</sup> Department of Pharmacology and Systems Therapeutics, Mount Sinai School of Medicine, One Gustave L. Levy Place, New York, NY 10029, USA

<sup>c</sup> Cardiovascular Research Institute, Mount Sinai School of Medicine, One Gustave L. Levy Place, New York, NY 10029, USA

<sup>d</sup> University of Medicine and Dentistry of New Jersey–Robert Wood Johnson Medical School, 675 Hoes Lane, Piscataway, NJ 08822, USA

<sup>e</sup> Dipartimento di Ematologia, Oncologia e Medicina Molecolare, Istituto Superiore di Sanità, Rome, Italy

## ARTICLE INFO

## Article history:

Received 25 October 2010

Received in revised form 11 February 2011

Accepted 1 March 2011

Available online 8 April 2011

## Keywords:

RAF1

Calcineurin

MEK1/2

ERK1/2

Hypertrophic cardiomyopathy

Noonan/LEOPARD syndrome

Cardiomyocyte hypertrophy

## ABSTRACT

RAS activation is implicated in physiologic and pathologic cardiac hypertrophy. Cross-talk between the Ras and calcineurin pathways, the latter also having been implicated in cardiac hypertrophy, has been suspected for pathologic hypertrophy. Our recent discovery that germ-line mutations in *RAF1*, which encodes a downstream RAS effector, cause Noonan and LEOPARD syndromes with a high prevalence of hypertrophic cardiomyopathy provided an opportunity to elaborate the role of *RAF1* in cardiomyocyte biology. Here, we characterize the role of *RAF1* signaling in cardiomyocyte hypertrophy with an aim of identifying potential therapeutic targets. We modeled hypertrophic cardiomyopathy by infecting neonatal and adult rat cardiomyocytes (NRCMs and ARCMs, respectively) with adenoviruses encoding wild-type *RAF1* and three Noonan/LEOPARD syndrome-associated *RAF1* mutants (S257L, D486N or L613V). These *RAF1* proteins, except D486N, engendered cardiomyocyte hypertrophy. Surprisingly, these effects were independent and dependent of mitogen activated protein kinases in NRCMs and ARCMs, respectively. Inhibiting Mek1/2 in *RAF1* overexpressing cells blocked hypertrophy in ARCMs but not in NRCMs. Further, we found that endogenous and heterologously expressed *RAF1* complexed with calcineurin, and *RAF1* mutants causing hypertrophy signaled via nuclear factor of activated T cells (Nfat) in both cell types. The involvement of calcineurin was also reflected by down regulation of *Serca2a* and dysregulation of calcium signaling in NRCMs. Furthermore, treatment with the calcineurin inhibitor cyclosporine blocked hypertrophy in NRCMs and ARCMs overexpressing *RAF1*. Thus, we have identified calcineurin as a novel interaction partner for *RAF1* and established a mechanistic link and possible therapeutic target for pathologic cardiomyocyte hypertrophy induced by mutant *RAF1*. This article is part of a Special Issue entitled 'Possible Editorial'.

© 2011 Elsevier Ltd. All rights reserved.

## 1. Introduction

Cardiac hypertrophy is elaborated via several intracellular signaling pathways including the calcineurin/nuclear factor of activated T cells (NFAT) and RAS/mitogen-activated protein kinase (MAPK) cascades [1]. Activation of RAS is implicated in cardiac hypertrophy, with cross-talk between the RAS and calcineurin pathways being suspected for pathologic hypertrophy but its basis being poorly understood [2]. Recently, *RAF1* missense mutations with gain-of-function effects on *RAF1*'s kinase activity were found to cause Noonan and LEOPARD syndromes (NS and LS, respectively) with a high prevalence of hypertrophic car-

diomyopathy (HCM) [3,4]. The majority of *RAF1* mutations causing NS and LS cluster around Ser<sup>259</sup> and Ser<sup>621</sup>. Those HCM-associated mutations exhibited high kinase activities and increased Erk activation in Cos cells highlighting the significance of those two phosphorylation sites, particularly as it pertains to cardiac hypertrophy (e.g., S257L and L613V). Mutations in the activation segment, which are infrequently associated with HCM (e.g., D486N), showed impaired kinase and reduced Erk activation in Cos cells. Here, we elucidated the role of *RAF1* in cardiac hypertrophy by expressing wild-type *RAF1* and three NS/LS-associated *RAF1* mutants representing the three mutation clusters, (S257L, D486N and L613V), in rat cardiomyocytes. Overexpression of the mutants from the Ser<sup>259</sup> and Ser<sup>621</sup> clusters (e.g., S257L or L613V) induced hypertrophy that was independent and dependent of Erk1/2 activation in NRCMs and ARCMs, respectively. The activation segment mutant, D486N, failed to induce hypertrophy. By analyzing various

\* Corresponding authors. Tel.: 212 241 3302; fax: 212 241 3310.

E-mail addresses: [djamel.lebeche@mssm.edu](mailto:djamel.lebeche@mssm.edu) (D. Lebeche), [bruce.gelb@mssm.edu](mailto:bruce.gelb@mssm.edu) (B.D. Gelb).

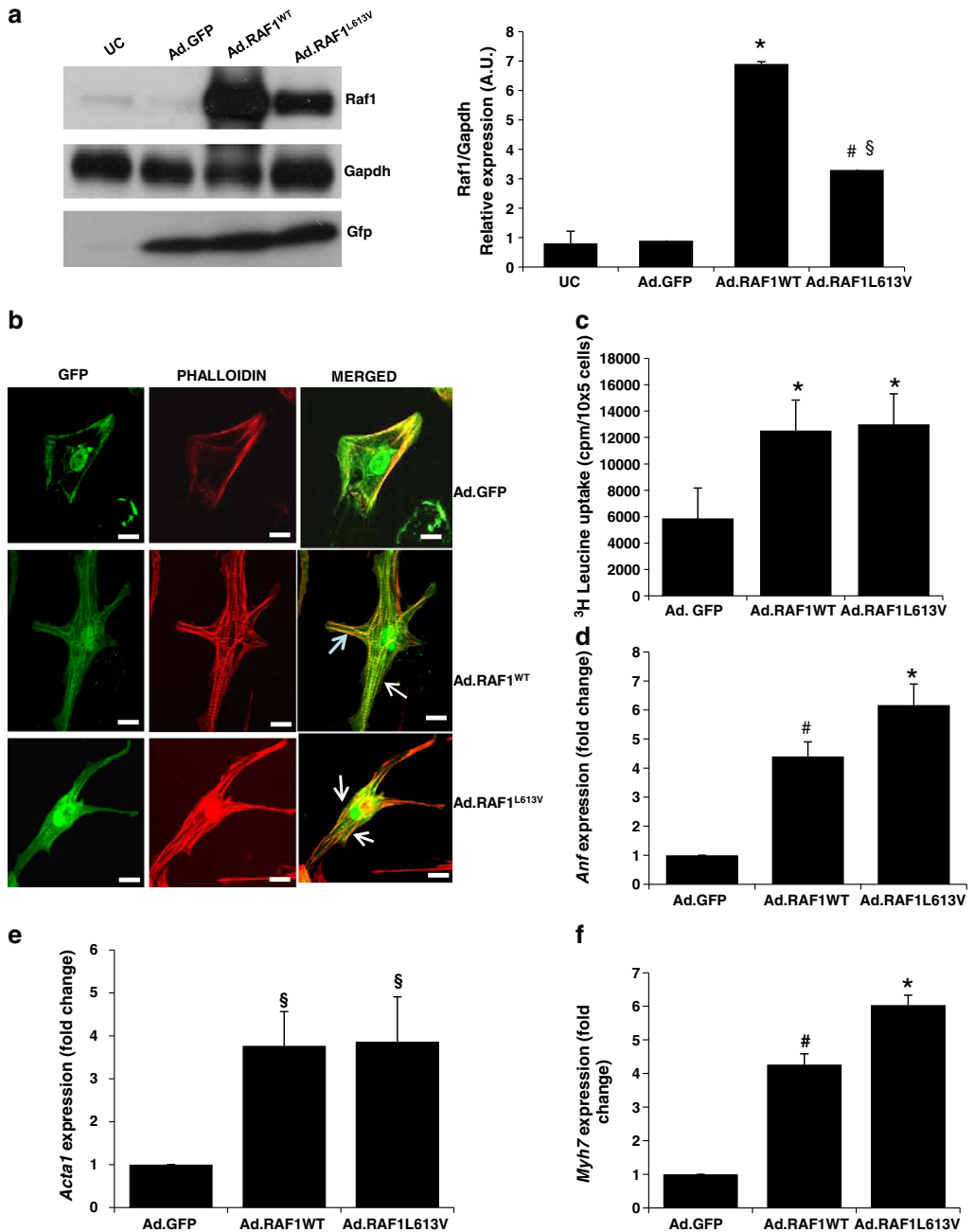


**Fig. 1.** Overexpression of wild-type and L613V RAF1 proteins induces cardiomyocyte hypertrophy. Neonatal rat cardiomyocytes were infected with adenoviruses encoding GFP alone (Ad.GFP), wild type RAF1 (Ad.RAF1<sup>WT</sup>) or a mutant RAF1 (Ad.RAF1<sup>L613V</sup>) and harvested after 72 hours. (a) Representative immunoblots with total lysates that were probed with anti-Raf1 (top panel), anti-Gapdh (middle panel) and anti-Gfp (lower panel) antibodies. Gapdh levels were used as loading control and Gfp levels were indicative of the efficiency of viral production. Uninfected cardiomyocytes (UC) were used as a negative control. Protein expression levels were normalized to respective Gapdh and expressed as relative expression. Data are mean values  $\pm$  SD of three independent experiments <sup>§</sup> $p < 0.05$  vs. Ad.GFP; \* $p < 0.01$  vs. Ad.GFP; # $p < 0.05$  vs. WT (b) Cardiomyocytes infected with the viruses indicated at the right expressing GFP (left column) and stained with phalloidin to detect sarcomeric  $\alpha$ -actinin (middle column) and merged (right column). Cells were imaged with confocal laser microscopy. Scale bar- 387  $\times$  387 nm. (c) [<sup>3</sup>H]-leucine incorporation in infected cardiomyocytes as an assessment of protein synthesis rates. \* $p < 0.001$  vs Ad.GFP. Data are mean values  $\pm$  SD of three independent experiments. (d-f) Quantitative reverse transcription PCR analysis of fetal gene re-activation. Steady-state mRNA levels of (d) atrial natriuretic factor (Anf), (e)  $\alpha$ -skeletal actin (Acta1) and (f)  $\beta$ -myosin heavy chain (Myh7) were performed. Expression levels were normalized to  $\beta$ -actin and expressed as fold change compared to level in the Ad.GFP cells. The mean fold induction  $\pm$  SD of three independent experiments is shown. <sup>§</sup> $p < 0.05$  vs. Ad.GFP; \* $p < 0.001$  vs. Ad.GFP; # $p < 0.01$  vs. Ad.GFP.

hypertrophic signaling pathways to identify molecules that RAF1 may regulate in cardiomyocytes, we identified calcineurin (also known as protein phosphatase 2B) as a major interacting partner of RAF1 in cardiomyocytes in NRCMs and ARCMs. Strikingly, the wild type and the mutants (S257L or L613V) RAF1-calcineurin complexes regulated calcium signaling and initiated hypertrophy in NRCMs and ARCMs. However, wild-type RAF1 signals through Mef2 in NRCMs but not in ARCMs. L613V RAF1 signals through Nfat in both cell types. In contrast, D486N RAF1 failed to activate Nfat or Mef2. Blocking the Erk pathway using a dominant negative form of Mek1 blocked hypertrophy in ARCMs, but not in NRCMs, overexpressing RAF1. In contrast, inhibiting calcineurin with cyclosporine blocked the induction of cardiomyocyte hypertrophy in NRCMs and ARCMs. Thus, we have identified calcineurin as a novel interaction partner for RAF1 and established a novel interaction between two nodal pathways in hypertrophy that has therapeutic implications for pathological cardiomyocyte hypertrophy induced by RAF1 mutants.

## 2. Methods

All animal procedures were performed with the approval of IACUC at the Mount Sinai School of Medicine and in accordance with the National Institute of Health's Guide for the Care and Use of Laboratory Animals. The methods used in this study are detailed in [5] and in the online data as supplement methods.

## 3. Results

### 3.1. Effect of a RAF1 mutant at the Ser<sup>621</sup> cluster (Ad.RAF1<sup>L613V</sup>) in NRCMs

We infected NRCMs with recombinant adenoviruses encoding either wild-type or L613V RAF1. After 72 h, Ad.RAF1<sup>WT</sup> and Ad.RAF1<sup>L613V</sup> infections resulted in increased RAF1 protein levels compared to control cells infected with Ad.GFP. Of note, RAF1 levels in NRCMs expressing the L613V mutant were lower than in those expressing the wild-type protein, which was not due to a difference in infection efficiency or expression from that virus since GFP levels were comparable among all infected cells (Fig. 1a). Treatment with the proteasomal inhibitor, MG132, equalized RAF1 levels among infected NRCMs (Supplementary Fig. 1a). Since the stability of RAF1 is dependent upon the phosphorylation of Ser<sup>621</sup> [6], which is near the mutation site, we considered the possibility that the L613V substitution might affect the phosphorylation status of that regulatory residue. Using phospho-specific antibodies, we found that Ser<sup>621</sup> of L613V RAF1 was minimally phosphorylated, which was different from wild-type RAF1, while the phosphorylation status of

Ser<sup>259</sup>, a residue that cooperatively regulates RAF1's function with Ser<sup>621</sup>, was normally phosphorylated (Supplementary Fig. 1b and c). Collectively, these data suggest that the L613V mutation negatively affects the phosphorylation of Ser<sup>621</sup> in cardiomyocytes, resulting in enhanced proteasomal degradation of this mutant RAF1 protein.

### 3.2. RAF1 overexpression induces cardiomyocyte hypertrophy with cell elongation in NRCMs

To determine whether expression of the L613V RAF1 in NRCMs promoted cardiomyocyte hypertrophy, modeling the HCM observed in NS and LS patients, cell surface area, sarcomeric organization, protein synthesis rate and fetal gene expression were analyzed. Seventy-two hours after adenoviral infection, NRCMs overexpressing wild-type and L613V RAF1 had significantly increased average surface areas compared to Ad.GFP-infected NRCMs, attributable to dramatic increases in cell length (Table 1, Fig. 1b and Supplementary Fig. 1d and e). As generally observed with cardiomyocyte hypertrophy, NRCMs overexpressing wild-type RAF1 showed an increase in sarcomeric reorganization but those overexpressing the mutant RAF1 showed a disorganized and diffused pattern of sarcomeric architecture, which were not present in GFP-overexpressing cells (Fig. 1b and Supplementary Fig. 1d). We examined protein synthesis rates of NRCMs overexpressing wild-type and L613V RAF1 using the [<sup>3</sup>H]-leucine incorporation method and observed marked increases compared to GFP-expressing cells (Fig. 1c). We also found that the steady-state expression levels of atrial natriuretic factor (*Anf*),  $\alpha$ -skeletal actin (*Acta1*) and  $\beta$ -myosin heavy chain (*Myh7*) were increased significantly in NRCMs overexpressing wild-type and L613V RAF1 compared to GFP-expressing cells (Fig. 1d–f), evidence of re-activation of the fetal gene program. Collectively, these data support the conclusion that overexpression of wild-type and L613V RAF1 promotes cardiomyocyte hypertrophy, but only L613V RAF1 causes sarcomeric disorganization.

### 3.3. RAF1 overexpression induces cardiomyocyte hypertrophy independent of Mapk activation in NRCMs

RAF1 phosphorylates Mek1/2, which then activate Erk1/2. To test our hypothesis that Erk activation was modulating the hypertrophy in cardiomyocytes overexpressing RAF1 proteins, we assessed the phosphorylation status of Erk1/2. Surprisingly, we observed that the ratio of phospho Erk1/2 to total Erk1/2 was unchanged in NRCMs overexpressing wild-type and L613V RAF1 compared to GFP-expressing cells respectively (Fig. 2a). Since this result was unexpected, we considered the possibility that RAS signaling was being desensitized

**Table 1**  
Morphometric analysis of cardiomyocytes.

Cell treatment	Area ( $\mu\text{m}^2$ )	Major axis ( $\mu\text{m}$ )	Minor axis ( $\mu\text{m}$ )	Major/minor
Ad.GFP	2123 $\pm$ 632	62 $\pm$ 11	40 $\pm$ 10	1.42 $\pm$ 0.32
Ad.RAF1 <sup>WT</sup>	3540 $\pm$ 1050	136 $\pm$ 35	33 $\pm$ 13	4.70 $\pm$ 1.98*
Ad.RAF1 <sup>L613V</sup>	3821 $\pm$ 1000	140 $\pm$ 38	32 $\pm$ 13	4.98 $\pm$ 2.15*
Ad.GFP + Ad.MEK <sup>DN</sup>	1982 $\pm$ 870	6515.34	43 $\pm$ 17.62	1.00 $\pm$ 0.41
Ad.RAF1 <sup>WT</sup> + Ad.MEK <sup>DN</sup>	3780 $\pm$ 1100	142 $\pm$ 37.02	35 $\pm$ 11.43	4.50 $\pm$ 2.00*
Ad.RAF1 <sup>L613V</sup> + Ad.MEK <sup>DN</sup>	3928 $\pm$ 1032	141 $\pm$ 40	34 $\pm$ 13.72	4.62 $\pm$ 2.15*
Ad.GFP + Ad.ASK <sup>DN</sup>	1962 $\pm$ 670	54 $\pm$ 15	44 $\pm$ 13.56	1.00 $\pm$ 0.21
Ad.RAF1 <sup>WT</sup> + Ad.ASK <sup>DN</sup>	3092 $\pm$ 890	142 $\pm$ 37.73	37 $\pm$ 9.2	4.60 $\pm$ 2.05*
Ad.RAF1 <sup>L613V</sup> + Ad.ASK <sup>DN</sup>	3789 $\pm$ 980	136 $\pm$ 43.98	34 $\pm$ 13	4.90 $\pm$ 4.15*
Ad.GFP + Ad.VIVIT	1937 $\pm$ 423	51 $\pm$ 02	41 $\pm$ 11	1.20 $\pm$ 0.01
Ad.RAF1 <sup>WT</sup> + Ad.VIVIT	3370 $\pm$ 992	132 $\pm$ 41	34 $\pm$ 11.2	4.59 $\pm$ 1.88*
Ad.RAF1 <sup>L613V</sup> + Ad.VIVIT	2003 $\pm$ 312	59 $\pm$ 13	39 $\pm$ 15	1.35 $\pm$ 0.12
Ad.GFP + Ad.MEF2 <sup>DN</sup>	1999 $\pm$ 356	49 $\pm$ 3	40 $\pm$ 8	1.01 $\pm$ 0
Ad.RAF1 <sup>WT</sup> + Ad.MEF2 <sup>DN</sup>	1890 $\pm$ 567	49 $\pm$ 02	39 $\pm$ 6.87	0.99 $\pm$ 0.2
Ad.RAF1 <sup>L613V</sup> + Ad.MEF2 <sup>DN</sup>	3800 $\pm$ 890	141 $\pm$ 33	29 $\pm$ 12	4.99 $\pm$ 1.68*

Values are means of SD of three independent experiments.

\*  $P \leq 0.01$  versus GFP cells.

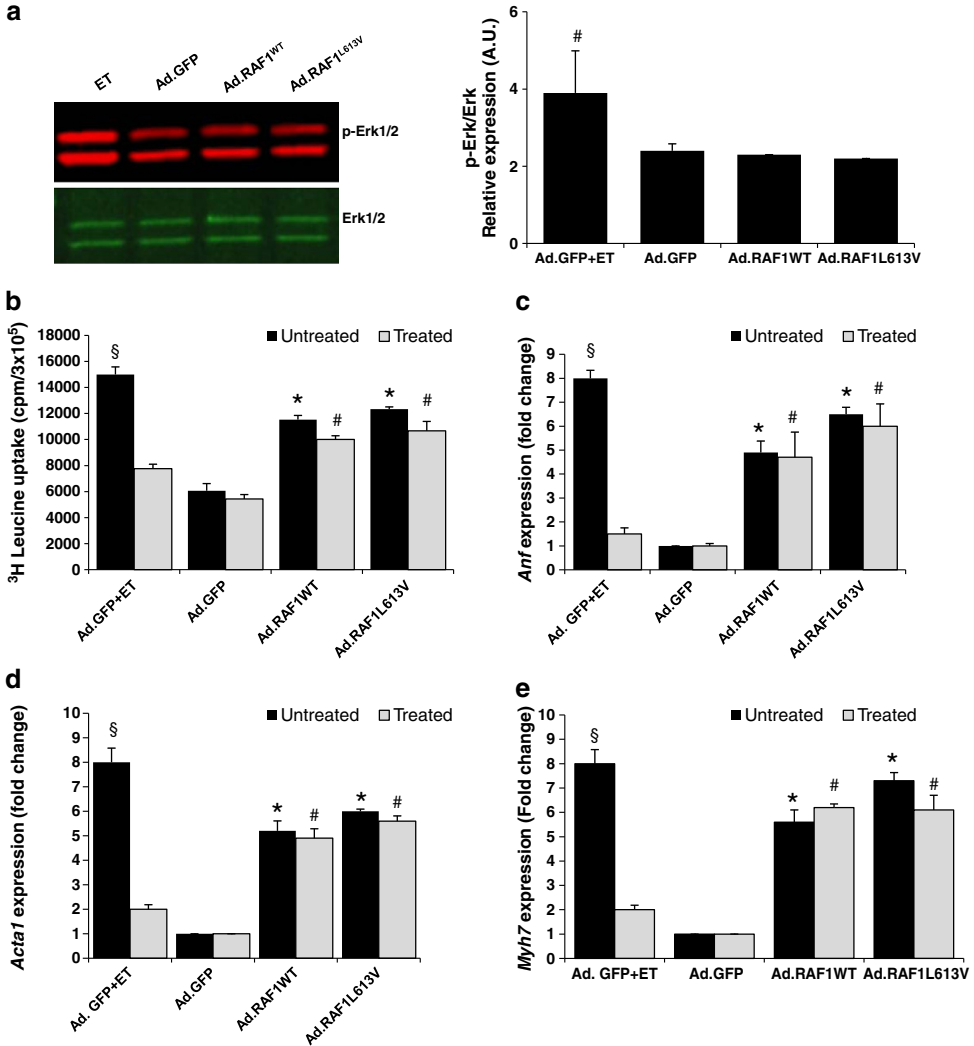


**Fig. 2.** Wild-type and L613V RAF1 does not cause cardiomyocyte hypertrophy via the mitogen-activated protein kinases (Mapk), Erk1/2. (a) Representative immunoblot analysis of phospho-Erk1/2 in neonatal rat cardiomyocytes infected with Ad.GFP, Ad.RAF1<sup>WT</sup> and Ad.RAF1<sup>L613V</sup>. A Mapk agonist, endothelin-1 (ET), that induces cardiac hypertrophy via Erk1/2, served as the positive control. Protein expression levels were normalized to total Erk and expressed as relative expression. Data are mean values  $\pm$  SD of three independent experiments. #*p* < 0.05 vs. Ad.GFP (b–e) To show that signaling via Erk1/2 was not necessary for RAF1-induced cardiomyocyte hypertrophy, a dominant-negative form of Mek1 was co-expressed using Ad.MEK<sup>DN</sup>. Co-infected cardiomyocytes were analyzed 72 hours post infection for (b) protein synthesis rates and steady-state expression levels of (c) *Anf*, (d) *Acta1* and (e) *Myh7*. Data are mean values  $\pm$  SD of three independent experiments. \**p* < 0.01 vs. untreated Ad.GFP; #*p* < 0.01 vs. treated Ad.GFP; §*p* < 0.001 vs. untreated Ad.GFP.

as cardiomyocyte hypertrophy progressed. To test this, we expressed a dominant-negative form of Mek1 along with the RAF1 proteins to block signaling to Erk1/2 and found no abrogation of the cardiomyocyte hypertrophy (Table 1 and Fig. 2b–e). Since overexpressed RAF1 proteins were able to induce cardiomyocyte hypertrophy independently of Erk1/2 activation in NRCMs, we explored whether activation of other Mapks was mediating this effect. Activation of Jnk (c-Jun N-terminal kinase) and p38 Mapk was similar and decreased, respectively, in NRCMs overexpressing wild-type and L613V RAF1 as compared to GFP-expressing cardiomyocytes (Supplementary Figs. 2 and 3). We then examined the status of Erk5 because its activation has been associated with cardiomyocyte elongation [7], but found that it was also unchanged in RAF1-expressing NRCMs (Supplementary Fig. 4a). Thus, we concluded that the overexpressed RAF1 proteins were able to signal independently of Mapk to engender NRCM hypertrophy.

### 3.4. Search for the mechanism underlying RAF1-Induced hypertrophy in NRCMs

Next, we assessed the status of several phosphoproteins participating in signaling pathways previously implicated in cardiac hypertrophy. We observed that the levels of phospho-Stat3 (Signal transducers and activators of transcription), -Akt (Protein kinase B), -Gsk3 $\beta$  (Glycogen synthase kinase), and -Acc (Acetyl-CoA carboxylase) (Supplementary Figs. 4b, 5a–b & 6) were not altered in NRCMs expressing wild-type or L613V RAF1 compared to GFP-expressing cells. These results suggested that signaling through the Jak-Stat, Akt-Gsk3 $\beta$ , and Ampk-Acc pathways was not engendering the RAF1-induced cardiomyocyte hypertrophy.

Ask1 (Apoptosis signal-regulating kinase 1) is known to interact directly with Raf1 and has roles in cardiomyocyte cell death and, possibly,

hypertrophy [8–10]. Calcineurin dephosphorylates Ask1 at Ser<sup>967</sup>, resulting in a loss of 14-3-3 binding and Ask1 activation [9]. We observed that NRCMs overexpressing L613V RAF1 had notably lower levels of pAsk1 (Ser<sup>967</sup>) compared to those overexpressing wild-type RAF1 or GFP (Fig. 3a) suggesting that Ask1 was activated by the mutant. However, co-expression of a dominant-negative form of Ask1 with RAF1 L613V failed to suppress cardiomyocyte hypertrophy (Table 1, Fig. 3b–e). Therefore, we concluded that Ask1 activation was not mediating this phenomenon.

### 3.5. Wild-type and L613V RAF1 signal through calcineurin to induce cardiomyocyte hypertrophy

Next, we explored a possible role of the calcineurin–Nfat pathway in RAF1-mediated cardiomyocyte hypertrophy since signaling through the Nfat transcription factors has been associated with pathologic cardiac hypertrophy. This seemed particularly plausible since p38 Mapk, which

can inhibit signaling via Nfat [11,12], showed reduced activity in NRCMs overexpressing wild-type and L613V RAF proteins (Supplementary Fig. 2). Using a luciferase reporter with nine multimerized Nfat binding sites, we observed that the Nfat activity in NRCMs expressing the L613V RAF1 was increased approximately 16 fold compared to cells infected with Ad.GFP or Ad.RAF1<sup>WT</sup> (Fig. 4a). To determine whether the increased transcriptional activity of Nfat was necessary for RAF1 L613V-induced cardiomyocyte hypertrophy, we co-infected cells with an adenovirus expressing VIVIT (Ad.VIVIT), a peptide that selectively blocks calcineurin's Nfat binding site without affecting its phosphatase activity. VIVIT expression nearly completely abrogated cardiomyocyte hypertrophy for NRCMs expressing L613V RAF1 but not for those expressing wild-type RAF1 and had minimal effect on cardiomyocytes expressing only GFP (Table 1 and Fig. 4b–e).

Since the cardiomyocyte hypertrophy engendered by overexpression of wild-type RAF1 could not be attributed to signaling through Nfat,

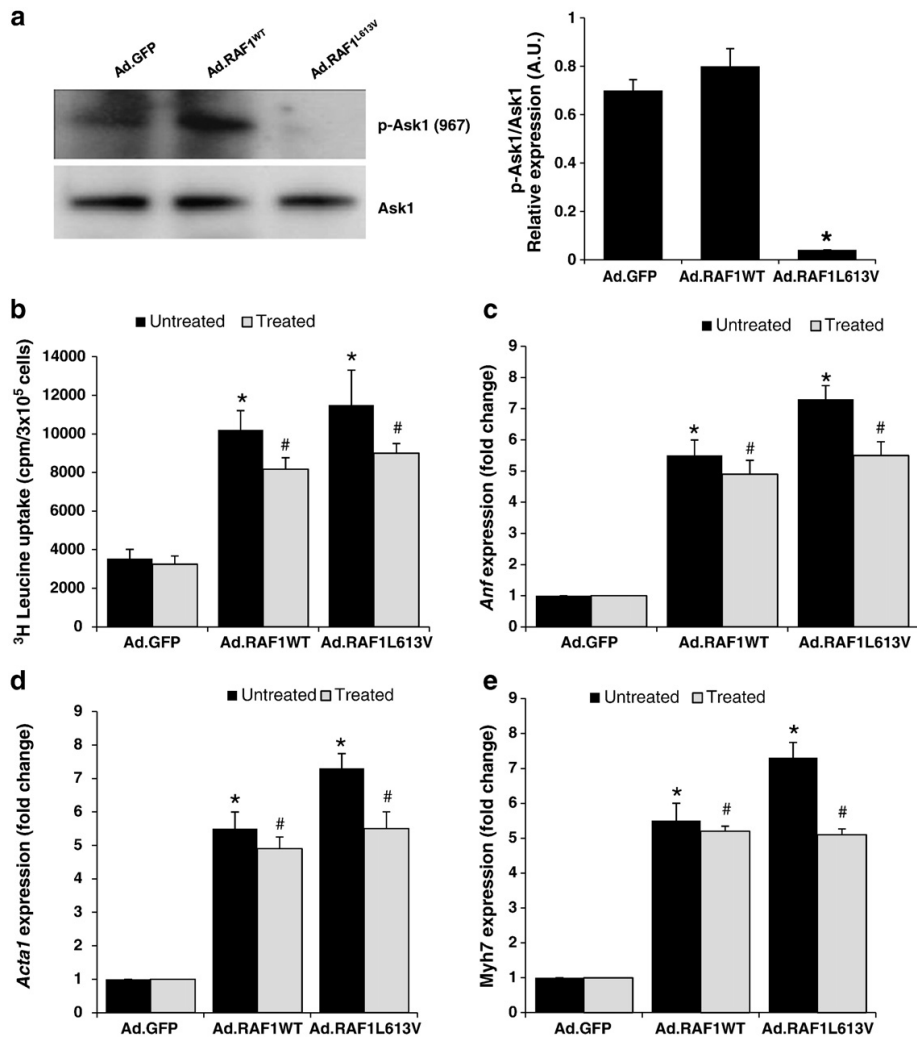


**Fig. 3.** ASK1 is not involved in RAF1-induced cardiomyocyte hypertrophy. (a) Representative immunoblots analysis of phospho-Ask1 (Ser967) and total Ask1 in neonatal rat cardiomyocytes overexpressing GFP, wild-type RAF1 and L613V RAF1. Protein expression levels were normalized to total Erk and expressed as relative expression. Data are mean values  $\pm$  SD of three independent experiments. \* $p < 0.01$  vs. Ad.GFP. Neonatal rat cardiomyocytes were infected with Ad.GFP, Ad.RAF1<sup>WT</sup> and Ad.RAF1<sup>L613V</sup> along with Ad.ASK1<sup>DN</sup> (treated). Seventy-two hours post infection, the cardiomyocytes were analyzed for protein synthesis rates (b) and steady-state mRNA levels of *Anf* (c), *Acta1* (d) and *Myh7* (e). \* $p < 0.01$  vs. untreated Ad.GFP; # $p < 0.01$  vs. treated Ad.GFP. Mean values  $\pm$  SD of three independent experiments are shown.

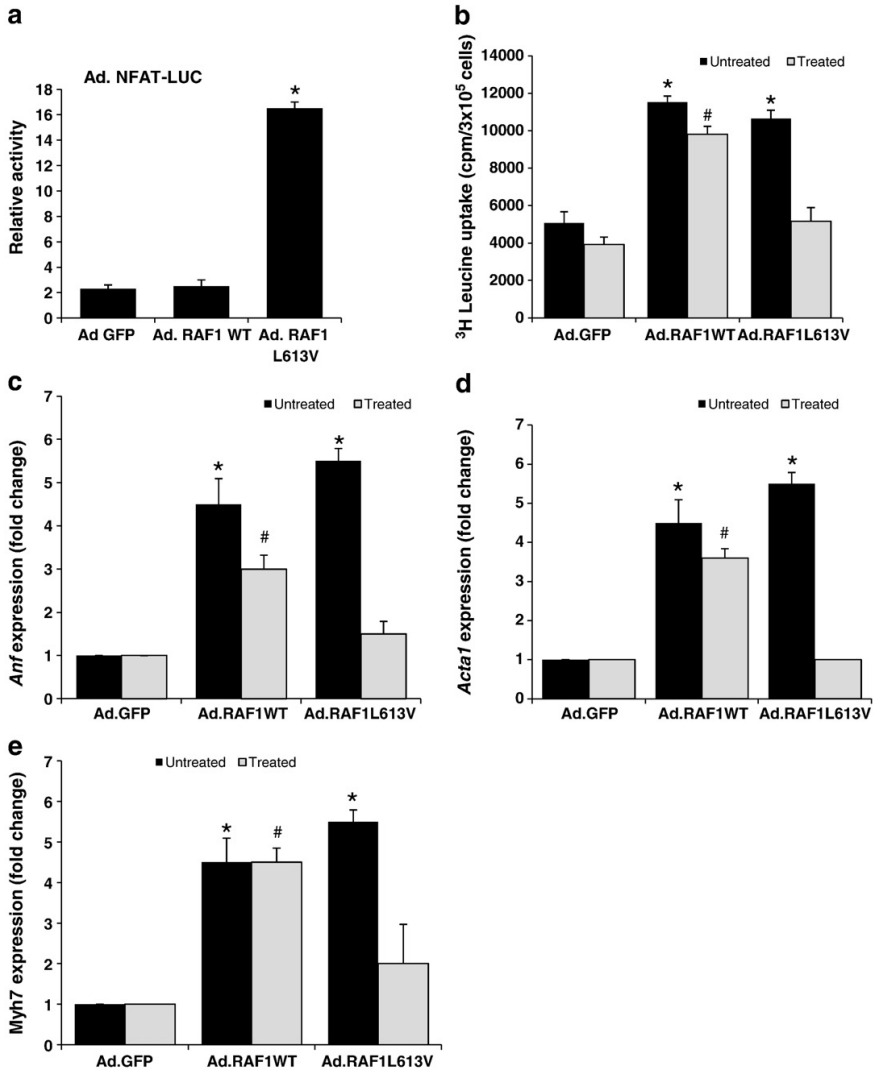


**Fig. 4.** L613V RAF1 but not wild-type RAF1 causes cardiomyocyte hypertrophy via Nfat. (a) Nfat activity was determined in neonatal rat cardiomyocytes infected with Ad.GFP, Ad.RAF1<sup>WT</sup> and Ad.RAF1<sup>L613V</sup> along with Ad.NFAT-LUC. Luciferase activity shown as relative light units (RLU) represent mean values ± SD of three independent experiments. \**p* < 0.001 vs Ad.GFP. Neonatal rat cardiomyocytes were co-infected with Ad.GFP, Ad.RAF1<sup>WT</sup> and Ad.RAF1<sup>L613V</sup> along with Ad.VIVIT (treated) that blocks NFAT specifically. Seventy-two hours post infection, cardiomyocytes were analyzed for protein synthesis rates (b) and steady-state mRNA levels of *Anf* (c), *Acta1* (d) and *Myh7* (e). \**p* < 0.01 vs. untreated Ad.GFP; #*p* < 0.01 vs. treated Ad.GFP. Mean values ± SD of three independent experiments are shown.

we considered the possibility that Mef2, another major downstream effector of calcineurin, was relevant [13]. Using a luciferase reporter with eight multimerized Mef2 binding sites, we observed that the Mef2 activity in NRCMs expressing wild-type RAF1 was increased approximately 15 fold compared to cells that were expressing GFP or L613V RAF1 (Fig. 5a). To determine whether the increased transcriptional activity of Mef2 was necessary for cardiomyocyte hypertrophy induced by wild-type RAF1, we co-infected cells with an adenovirus expressing dominant-negative Mef2. Dominant-negative Mef2 nearly completely abrogated cardiomyocyte hypertrophy for NRCMs expressing wild-type RAF1 but not for those expressing L613V RAF1 and had minimal effect on cells expressing only GFP (Table 1 and Fig. 5b–e).

The foregoing results support the idea that wild-type and L613V RAF1 induce cardiac hypertrophy by signaling through calcineurin,

albeit through different effectors (Mef2 and Nfat, respectively). To provide evidence that this signaling required calcineurin, we used a pharmacologic approach. Treatment with the calcineurin-inhibitor, cyclosporine A, eliminated cardiomyocyte hypertrophy for NRCMs expressing wild-type or L613V RAF1 as assessed by cell area, protein synthesis rate and re-expression of fetal markers (Table 1, Fig. 6a–d).

### 3.6. RAF1 directly interacts with calcineurin

Since wild-type and L613V RAF1 proteins were signaling through calcineurin, we considered the possibility that there was a physical interaction between the RAF1 and calcineurin. Using co-immunoprecipitation, we detected RAF1 and calcineurin immunologically in

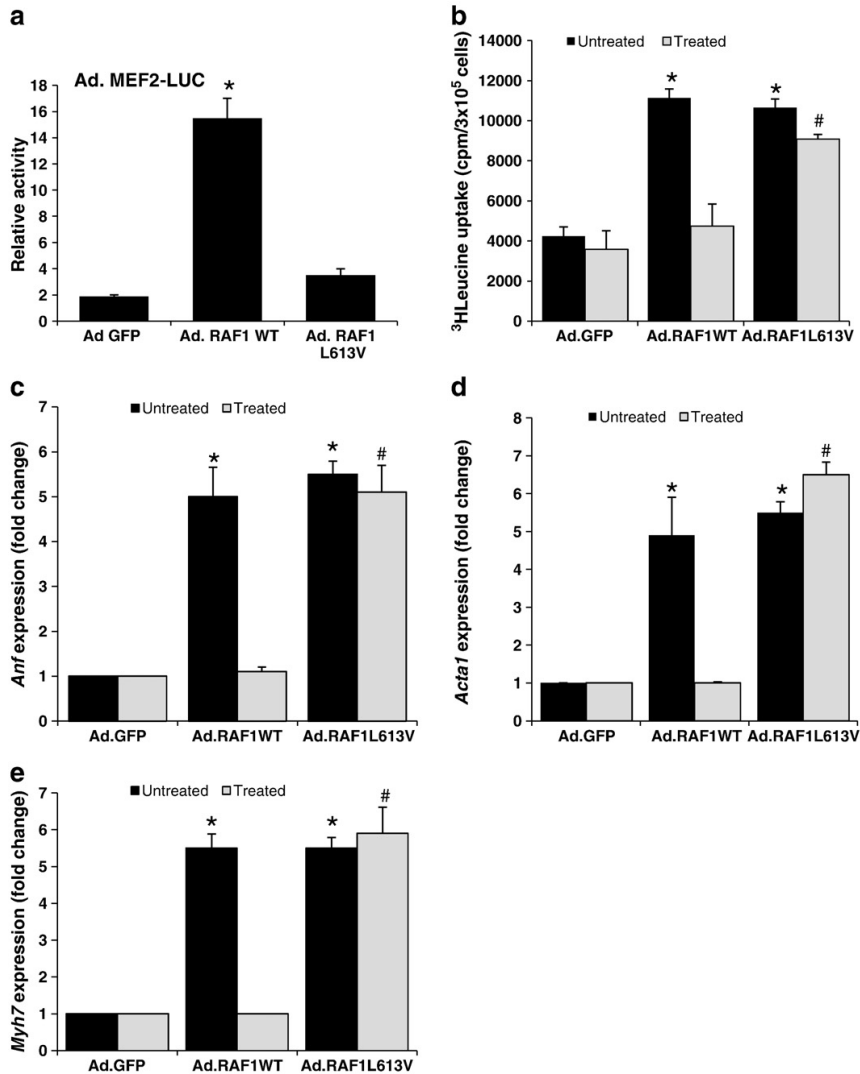


**Fig. 5.** Wild-type RAF1 but not L613V RAF1 causes cardiomyocyte hypertrophy via Mef2. (a) Mef2 activity was determined in neonatal rat cardiomyocytes infected with Ad.GFP, Ad.RAF1<sup>WT</sup> and Ad.RAF1<sup>L613V</sup> along with Ad.MEF2-LUC. Luciferase activity shown as relative light units (RLU) represent mean values  $\pm$  SD of three independent experiments. \* $p < 0.001$  vs Ad.GFP. Neonatal rat cardiomyocytes were co-infected with Ad.GFP, Ad.RAF1<sup>WT</sup> and Ad.RAF1<sup>L613V</sup> along with Ad.MEF2<sup>DN</sup> (treated). Seventy-two hours post infection, cardiomyocytes were analyzed for protein synthesis rates (b) and steady-state mRNA levels of *Anf* (c), *Acta1* (d) and *Myh7* (e). \* $p < 0.01$  vs. untreated Ad.GFP; # $p < 0.01$  vs. treated Ad.GFP. Mean values  $\pm$  SD of three independent experiments are shown.

immunoprecipitates from cells overexpressing RAF1 (Fig. 6e and f). More importantly, we detected Raf1-calcineurin complexes in uninfected NRCMs, documenting that this interaction was not an artifact of RAF1 overexpression. Taken together, these data suggest that the interaction of Raf1 and calcineurin is likely to mediate physiological and pathological signaling in cardiomyocytes.

### 3.7. RAF1 impairs calcium signaling by down-regulating sarco/endoplasmic reticulum $Ca^{2+}$ -ATPase 2a (SERCA2a)

Calcineurin/Nfat signaling has been implicated as a critical transducer that uniquely links changes in intracellular calcium handling in cardiac hypertrophy [14,15]. Thus, the observed interac-

tion also pointed to the possibility that RAF1 might target components of calcium regulatory proteins through calcineurin and regulate calcium activity. We measured the total expression levels of several proteins (Serca2a, sodium-calcium exchanger (Ncx1) and inositol 1, 4, 5-triphosphate (Ip3)) that are known to play vital roles in calcium signaling in conjunction with calcineurin. We found that Serca2a was significantly down regulated in NRCMs overexpressing wild-type and L613V RAF1 but that the other proteins were unchanged (Fig. 7a–c). To evaluate whether altered signaling through the RAF1-calcineurin complex perturbed intracellular  $Ca^{2+}$  handling, intracellular cytoplasmic  $Ca^{2+}$  transients were measured. With slow pacing at 0.2 Hz,  $Ca^{2+}$  transients in cardiomyocytes expressing GFP followed electrical stimuli with a 1:1 correspondence, whereas the RAF1-

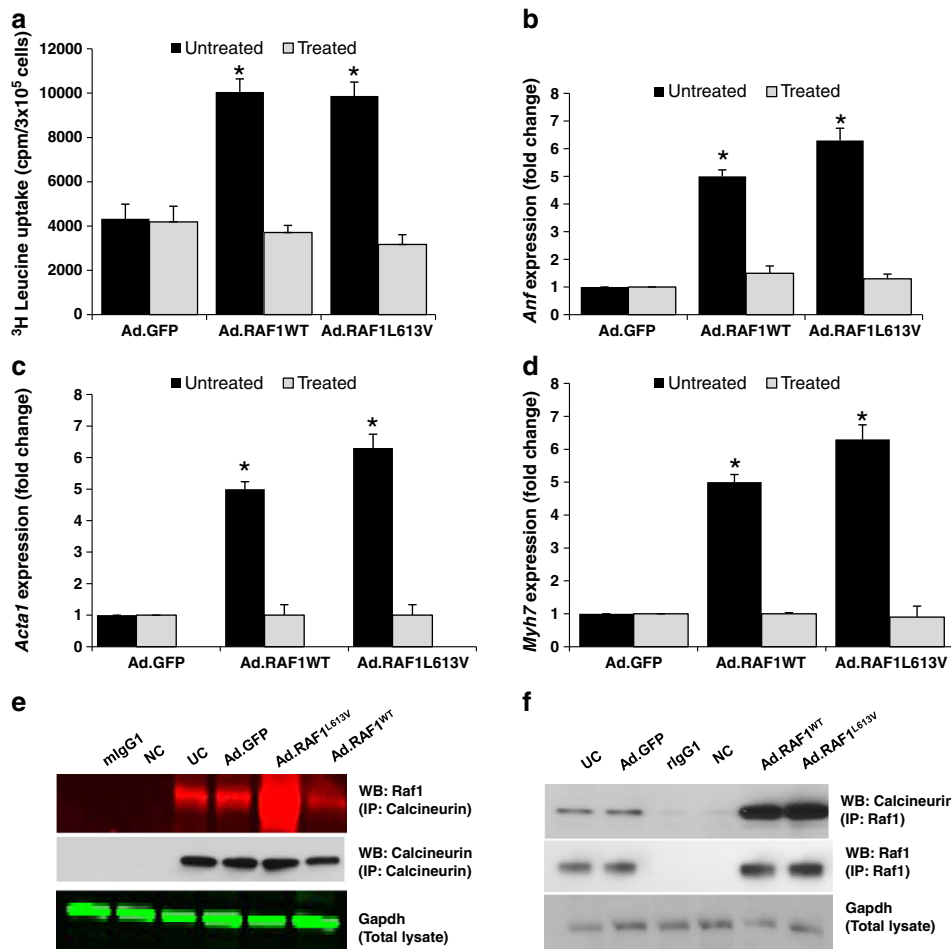


**Fig. 6.** Calcineurin inhibition blocks the hypertrophy induced by wild-type and L613V RAF1 proteins. Neonatal rat cardiomyocytes were infected with Ad.GFP, Ad.RAF1<sup>WT</sup> and Ad.RAF1<sup>L613V</sup> and treated with cyclosporine after 48 hours. Seventy-two hours post infection, cardiomyocytes were analyzed for protein synthesis rates (a) and steady-state mRNA levels of *Anf* (b), *Acta1* (c) and *Myh7* (d). \* $p < 0.01$  vs untreated Ad.GFP. Mean values  $\pm$  SD of three independent experiments are shown. Raf1 complexes with calcineurin (e) Immunoblots with the indicated antibodies after immunoprecipitation with anti-calcineurin antibody, rabbit pre-immune IgG (rlgG1) or Gapdh as negative control (NC) and reprobbed for calcineurin (e) Immunoblots with the indicated antibodies after immunoprecipitation with anti-RAF1 antibody, mouse pre-immune IgG (mlgG1) or Gapdh as negative control (NC) and reprobbed for Raf1 (f).

overexpressing cells exhibited spontaneous  $\text{Ca}^{2+}$  transients that were unassociated with electrical stimuli, indicative of unstable  $\text{Ca}^{2+}$  handling (Fig. 8a–c). To quantify the degree of  $\text{Ca}^{2+}$  handling dysfunction, we computed three measures as described in Methods and Supplementary Methods. During 0.2-Hz pacing, the wild-type and L613V RAF1-overexpressing cardiomyocytes exhibited slower average  $\text{Ca}^{2+}$  transient rates of decay (Fig. 8d) and greater percentages of cells exhibiting spontaneous  $\text{Ca}^{2+}$  transients (Fig. 8e) compared to control cardiomyocytes expressing GFP. Pacing at 2 Hz induced irregular  $\text{Ca}^{2+}$  transients to a greater extent in the wild-type and L613V RAF1-overexpressing cardiomyocytes than in control cells (Fig. 8f). Further, the sarcoplasmic reticulum (SR) calcium load in the L613V RAF1-overexpressing cardiomyocytes was increased compared to wild type and GFP (Fig. 8g). Thus, the present data establish a potential link between signaling from RAS through RAF1 for pathologic hypertrophy and calcium dysregulation, which could be potentially arrhythmogenic.

### 3.8. Effects of RAF1 mutations at the Ser<sup>259</sup> cluster and activating segment

The L613V mutation is representative of the HCM-associated mutations that cluster at the C-terminus near Ser<sup>621</sup>. To understand the effects of mutations at the Ser<sup>259</sup> cluster and the activating segment, we infected NRCMs with representative recombinant adenoviruses encoding either S257L or D486N RAF1 and performed key experiments including assessments of the phosphorylation status of RAF1, Erk1/2 activation, cellular hypertrophy, Nfat and Mef2 signaling, and RAF1-calcineurin complexing as well as determining the effect of treating with cyclosporine to rescue the hypertrophic phenotype. As anticipated, we found that S257L RAF1 negatively affected the phosphorylation of Ser<sup>259</sup> but phosphorylation of that residue was normal in the D486N protein (Supplementary Fig. 7). The levels of pErk1/2 activation were unchanged in NRCMs overexpressing the S257L or D486N RAF1 proteins (Supplementary Fig. 8). Overexpression of the S257L RAF1 induced cardiac hypertrophy similarly to L613V protein whereas the kinase-dead mutant,

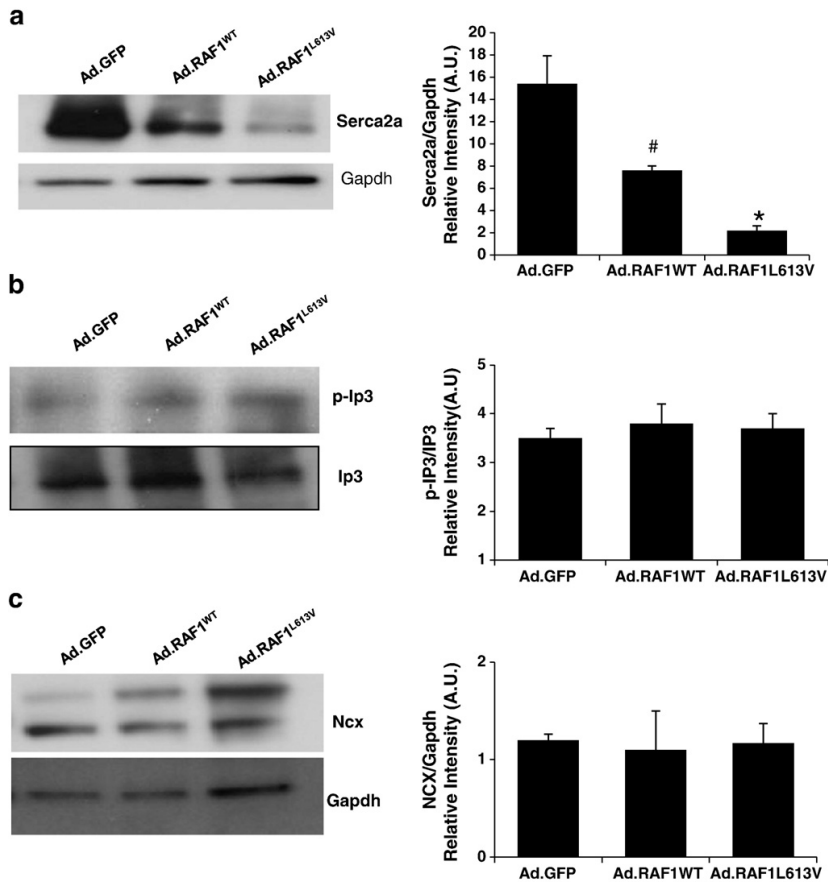


**Fig. 7.** Serca2a is downregulated, but other calcium regulatory proteins are unchanged, in cardiomyocytes expressing RAF1. Representative immunoblots with total lysates from neonatal rat cardiomyocytes expressing GFP, wild-type RAF1 or L613V RAF1 that were probed with anti-Serca2a, -Gapdh, p-Ip3, -Ip3, -Ncx, and -Gapdh antibodies in panels from top to bottom (a–c). Protein expression levels were normalized to indicated antibodies and expressed as Relative Expression. Data are mean values  $\pm$  SD of three independent experiments. <sup>\*</sup> $p < 0.01$  and <sup>#</sup> $p < 0.01$  vs. Ad.GFP.

D486N, failed to induce hypertrophy as assessed by protein synthesis rate and fetal gene expression (Supplementary Fig. 9a–c). Further, transcription activity from Nfat, but not Mef2, was increased in cardiomyocytes overexpressing S257L RAF1 whereas overexpression of D486N protein failed to induce Nfat or Mef2 activity (Supplementary Fig. 10a and b). As with endogenous Raf1 and overexpressed wild-type and L613V RAF1 proteins, S257L RAF1 complexed with calcineurin; that interaction was abrogated for overexpressed D486N RAF1 (Supplementary Fig. 11). Finally, we were able to rescue the hypertrophic phenotype engendered by S257L RAF1 overexpression using cyclosporine (Supplementary Fig. 9). Collectively, these results suggest that RAF1 mutations at the Ser<sup>259</sup> and Ser<sup>621</sup> clusters in NRCMs mediate cardiomyocyte hypertrophy through a comparable mechanism dependant upon signaling through calcineurin but not Erk1/2 and also explain the negative association of HCM with RAF1 mutations residing in the activation loop.

### 3.9. Effects of RAF1 mutant (L613V) on adult cardiomyocytes (ARCMs)

To understand the effects of the RAF1 mutations in ARCMs, we infected those cells with representative recombinant adenoviruses encoding either WT or L613V RAF1 and performed key experiments including assessments of the cell surface area, phosphorylation status of

RAF1, Erk1/2 activation, cellular hypertrophy, Nfat and Mef2 signaling, and RAF1-calcineurin complexing as well as determining the effect of treating with cyclosporine to rescue the hypertrophic phenotype. Cell surface areas were increased in the ARCMs overexpressing WT and L613V compared to GFP (Supplementary Fig. 12 a and b). As observed with NRCMs, the overexpression of L613V was low compared to WT (Supplementary Fig. 13a) and phosphorylation was reduced at S621 but unchanged at S259 (Supplementary Fig. 13b). In contrast to the findings with NRCMs, overexpression of L613V RAF1 increased the levels of pErk1/2 in ARCMs (Supplementary Fig. 14). Overexpression of the WT and L613V RAF1 induced cardiac hypertrophy as assessed by fetal gene expression (Supplementary Fig. 15a, b and c). Further, transcription activity from Nfat was increased in cardiomyocytes overexpressing L613V RAF1 whereas overexpression of WT failed to induce Nfat or Mef2 activity (Supplementary Fig. 16a). WT and L613V RAF1 interact with calcineurin in ARCMs as had been observed in NRCMs (Supplementary Fig. 16b). Finally, we were able to rescue the hypertrophic phenotype engendered by RAF1 overexpression by co-expressing a dominant negative form of MEK or by treating with cyclosporine (Supplementary Figs. 15 and 17 a, b and c). Collectively, these results suggest that the hypertrophic effects of RAF1 in ARCMs depend upon signaling through Mek/Erk and calcineurin.

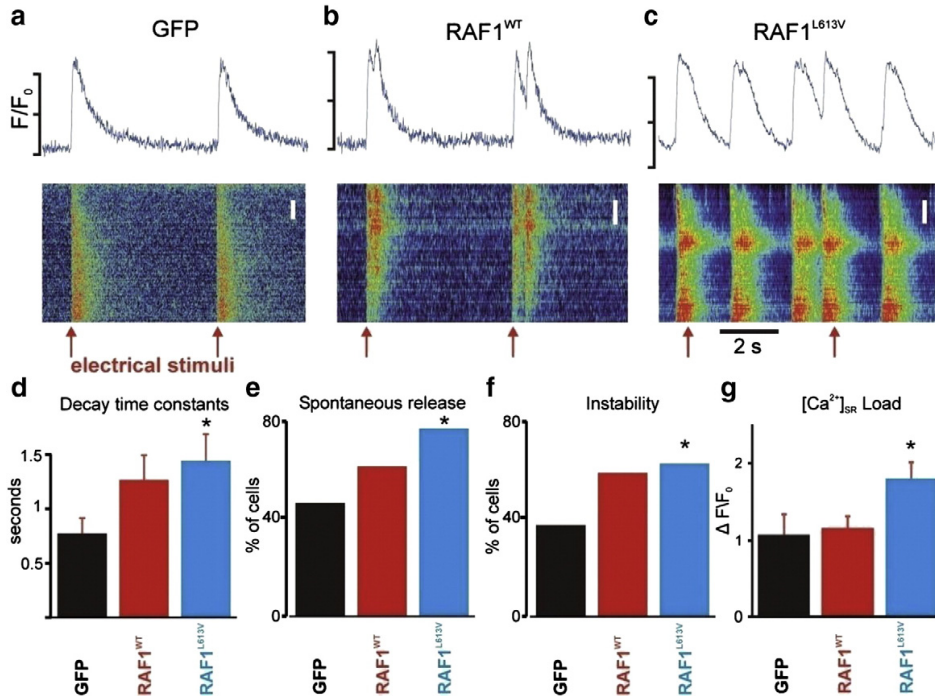


**Fig. 8.** Intracellular calcium handling is dysregulated in neonatal rat cardiomyocytes expressing wild-type and L613V RAF1. (a–c) Intracellular Ca<sup>2+</sup> transients from the three groups, as indicated, expressed as space–time images (bottom) and average intracellular fluorescence (units of F/F<sub>0</sub>, top). Image scaling and Ca<sup>2+</sup> transient scale bars are different in the three cases because of different baseline Ca<sup>2+</sup> transient amplitudes. Top scale bars indicate F/F<sub>0</sub> ranges of 1.0–1.5 (left), 1.0–2.0 (middle), and 1.0–2.0 (right). Red arrows indicate timing of electrical stimuli, here delivered every 5 seconds. Spatial scale bars indicate 2 μm in all cases. (d) Ca<sup>2+</sup> transient decay time constants, calculated from the following numbers of cells: n = 42 (GFP), n = 39 (WT RAF1) and n = 36 (L613V RAF1). \*p < 0.05 vs. GFP by two-tailed Student's t-test. (e) Percentage of cells in each group exhibiting spontaneous Ca<sup>2+</sup> release when paced at 0.2 Hz. \*p < 0.05 vs. GFP by two-tailed Fisher's exact test. (f) Percentage of cells in each group showing unstable beat-to-beat Ca<sup>2+</sup> release when paced at 2 Hz. \*p < 0.05 vs. GFP by two-tailed Fisher's exact test. (g) SR Ca<sup>2+</sup> load, quantified as peak ΔF/F<sub>0</sub> in response to 20 mM caffeine. Bars calculated from n = 30 cells from each group. \*p < 0.05 vs. GFP by two-tailed Student's t-test. See Supplementary Methods for details of calculation of these metrics.

#### 4. Discussion

Collectively, our results provide important, molecular and clinically-relevant insights into the signaling pathways leading to cardiac hypertrophy. Cardiac hypertrophy is stimulated by biomechanical and neurohumoral mechanisms. Neurohumoral stimuli include ligands such as growth factors, hormones and cytokines that utilize G-protein-coupled receptors, gp-130-linked receptors and receptors kinases, particularly receptor tyrosine kinases (RTKs). Activation of RAS, which is a well-described result of RTK stimulation, occupies a critical role in cardiac hypertrophy as first established with *in vitro* studies with cardiomyocytes and *in vivo* studies with transgenic mice expressing constitutively active Hras (G12V) [16,17]. Transgenic mice with cardiac-specific expression of Hras G12V developed HCM with myofibrillary disarray and *Anf* re-expression, phenocopying human HCM observed in individuals with sarcomeric gene defects as well in NS.

The canonical signaling pathway downstream from RAS is RAF–MEK–ERK. Numerous studies have examined the role of this pathway in cardiac hypertrophy with interesting, if complex, results. Overexpression of activated Mek1 in the mouse heart resulted in concentric hypertrophy with Erk1/2 activation and re-activation of *Anf* expression but did not cause cardiac fibrosis, diastolic dysfunction or lethality, consistent with physiologic rather than pathologic hypertrophy [18]. Pharmacologic inhibition of Raf and Mek in cultured cardiomyocytes blocked endothelin-1 and phenylephrine-induced hypertrophy and Mek inhibition prevented L-NAME-induced hypertrophy in rats [19,20]. Transgenic expression of a dominant-negative Raf1 in mouse heart

resulted in a reduced hypertrophic response to pressure overload with diminished Erk1/2 activation and no re-activation of *Anf* expression [21]. In contrast, genetic reduction of Erk activation *per se* (*Erk1*<sup>−/−</sup> and *Erk2*<sup>+/-</sup> mice as well as *Dusp6* transgenic mice) did not abrogate the hypertrophic response to pressure overload [22]. Recently, Erk1/2 has also been shown to be a critical regulator of cell growth and size in cardiac hypertrophy. Eccentric (elongated) hypertrophy does not involve Erk1/2 whereas concentric (width wise) hypertrophy requires Erk1/2 [23]. Our data are consistent with these findings as overexpression of RAF1 proteins induced elongated growth without Erk1/2 activation in NRCMs but concentric growth with Erk1/2 activation in ARCMs. Taken as a whole, it appears that signaling from RAS to ERK1/2 plays some role in cardiac hypertrophy but the involvement of other pathways is suggested.

Our results provide new insights into how RTK activation signaling through RAS induces hypertrophy. We showed that overexpression of wild-type and gain-of-function RAF1 in ARCMs caused cardiomyocyte hypertrophy by activating the Erk1/2 and calcineurin pathways whereas similar RAF1 overexpression in NRCMs only activated calcineurin signaling. Activation of multiple pathways either in parallel or independently by RAS–MAPK members including RAS, SOS1 and MEK are widely observed. For example, overexpression of Hras G12V in NRCMs resulted in increased Jnk and Nfat activity [24]. Also, activated Mek expression in NRCMs and in transgenic mice increased Erk1/2 [23] and Nfat activity in a calcineurin-independent manner [7]. Interestingly, cardiac tissue from *Sos1* mouse model also showed upregulation of multiple pathways including Erk1/2, Rac and Stat3

[25]. Our observations that RAF1 overexpression induced hypertrophy via multiple pathways (Erk1/2 and calcineurin) depending on the developmental stage of heart, and that RAF1 and calcineurin interact directly outlines a crucial role for these pathways in the pathogenesis of cardiomyopathy in NS. Following the seminal discovery of the role of signaling via calcineurin–NFAT in pathologic hypertrophy [26], interactions between that pathway and RAS signaling have been contemplated. Based on our present data, we suggest that the level of cross-talk between the RAS and calcineurin pathways might be crucial at the RAF1 level. However, RAF1 regulation is highly intricate, depending upon various factors including the type of cardiomyocyte, localization, time, dose, type of stimulus and feedback mechanisms. Further adding to the complexity, NRCMs and ACMs have overlapping and significant physiological and functional differences as reviewed [27]. Thus, it is possible that *in vitro* overexpression may result in complex results. Clearly, additional studies using a Raf1 mouse model at various cardiac developmental stages addressing the differences in the activation of Erk1/2 and/or calcineurin–NFAT pathways will shed light on this particular hypertrophic signaling pathway.

Clinical observations concerning inherited RAS pathway disorders correlate well with the experimental data about the roles of specific proteins in that pathway vis à vis cardiac hypertrophy. To date, germline *MEK1* and *MEK2* mutations have been identified in 28 individuals with cardio-facio-cutaneous syndrome, of whom 8 (29%) had HCM [28–31]. Data about HCM severity or its outcome were not provided save the single case described by Dentici et al., in which the HCM was described as mild [31]; no arrhythmia has been associated with a *MEK* mutation. Of note, all *MEK* mutants that have been characterized biochemically demonstrate increased kinase activity with some being constitutively active [31,32]. The prevalence of HCM among patients with Noonan syndrome caused by *RAF1* defects is considerably higher 27/35 (77%) if all mutations are included and 26/29 (90%) for gain-of-function mutations clustering near Ser<sup>259</sup> and Ser<sup>621</sup> [3,4,32,33]. Moreover, the severity of the HCM appears to be greater with several instances of sudden death and one of atrial ectopic tachycardia [34]. Of interest, *HRAS* Gly<sup>12</sup> and Gly<sup>13</sup> missense mutations underlying Costello syndrome also engender HCM and atrial arrhythmias (19 and 17 of 40 patients for prevalence rates of 47% and 42%, respectively) [35]. The commonest allele, constituting 82% of cases, is G12S, which has substantially less GTPase activity than the G12V allele that caused remarkable hypertrophy in NRCMs and transgenic mice. Thus, germline gain-of-function *RAF1* and *MEK1/2* mutations in humans are experiments of nature that provide evidence that RAF1 occupies a more important role in pathologic cardiac hypertrophy than do *MEK1/2*. These clinical observations are consistent with our current findings showing that RAF1 can signal through multiple pathways depending on the developmental stage of the heart to induce pathologic hypertrophy, even bypassing the Erk1/2

Finally, calcium handling in cardiomyocytes with increased Ras signaling has previously been shown to be altered. In transgenic mice expressing Hras G12V in the myocardium, Serca2a protein levels were modestly depressed [36]. These findings are consistent with our observations with NRCMs overexpressing gain-of-function RAF1, in which Serca2a was also reduced and there was decreased decay of calcium transients with spontaneous calcium transients. These abnormalities in calcium handling may provide the rationale for the atrial arrhythmias observed in Costello syndrome and *RAF1*-associated Noonan syndrome as well as the sudden death risk associated with the latter.

Supplementary materials related to this article can be found online at doi:10.1016/j.yjmcc.2011.03.001.

## Disclosures

Drs. Gelb and Tartaglia have a patent pending for genetic testing for *RAF1* mutations causing Noonan and LEOPARD syndromes.

## Acknowledgments

This work was supported in part by grants from the Children's Cardiomyopathy Foundation (B.D.G.), the National Institutes of Health (HL071207 to B.D.G.; R01HL078731, R01HL080498, R01HL083156, R01HL093183, R01HL088434 and P20HL100396 to R.J.H.; HL076659 to D.L.; HL076230 to E.A.S.), the Transatlantic Leducq Foundation (R.J.H.), the ERA-Net for research programmes on rare diseases 2009 (M.T.) and Telethon-Italy GGP10020 (M.T.).

## References

- Heineke J, Molkenin JD. Regulation of cardiac hypertrophy by intracellular signalling pathways. *Nat Rev Mol Cell Biol* 2006;7(8):589–600.
- Molkenin JD. Calcineurin–NFAT signaling regulates the cardiac hypertrophic response in coordination with the MAPKs. *Cardiovasc Res* 2004;63(3):467–75.
- Pandit B, Sarkozy A, Pennacchio LA, Carta C, Oishi K, Martinelli S, et al. Gain-of-function *RAF1* mutations cause Noonan and LEOPARD syndromes with hypertrophic cardiomyopathy. *Nat Genet* 2007;39(8):1007–12.
- Razzaque MA, Nishizawa T, Komoike Y, Yagi H, Furutani M, Amo R, et al. Germline gain-of-function mutations in *RAF1* cause Noonan syndrome. *Nat Genet* 2007;39(8):1013–7.
- Kim M, Oh JK, Sakata S, Liang I, Park W, Hajjar RJ, Lebecke D. Role of resistin in cardiac contractility and hypertrophy. *J Mol Cell Cardiol* 2008;45(2):270–80.
- Noble C, Mercer K, Hussain J, Carragher L, Giblett S, Hayward R, et al. CRAF autophosphorylation of serine 621 is required to prevent its proteasome-mediated degradation. *Mol Cell* 2008;31(6):862–72.
- Nicol RL, Frey N, Pearson G, Cobb M, Richardson J, Olson EN. Activated MEK5 induces serial assembly of sarcomeres and eccentric cardiac hypertrophy. *EMBO J* 2001;20(11):2757–67.
- Liu Q, Sargent MA, York AJ, Molkenin JD. ASK1 regulates cardiomyocyte death but not hypertrophy in transgenic mice. *Circ Res* 2009;105(11):1110–7.
- Liu Q, Wilkins BJ, Lee YJ, Ichijo H, Molkenin JD. Direct interaction and reciprocal regulation between ASK1 and calcineurin–NFAT control cardiomyocyte death and growth. *Mol Cell Biol* 2006;26(10):3785–97.
- Chen J, Fujii K, Zhang L, Roberts T, Fu H. Raf-1 promotes cell survival by antagonizing apoptosis signal-regulating kinase 1 through a MEK–ERK independent mechanism. *Proc Natl Acad Sci USA* 2001;98(14):7783–8.
- Sanna B, Bueno OF, Dai YS, Wilkins BJ, Molkenin JD. Direct and indirect interactions between calcineurin–NFAT and MEK1–extracellular signal-regulated kinase 1/2 signaling pathways regulate cardiac gene expression and cellular growth. *Mol Cell Biol* 2005;25(3):865–78.
- Braz JC, Bueno OF, Liang Q, Wilkins BJ, Dai YS, Parsons S, et al. Targeted inhibition of p38 MAPK promotes hypertrophic cardiomyopathy through upregulation of calcineurin–NFAT signaling. *J Clin Invest* 2003;111(10):1475–86.
- Wu H, Rothermel B, Kanatous S, Rosenberg P, Naya FJ, Shelton JM, et al. Activation of MEF2 by muscle activity is mediated through a calcineurin-dependent pathway. *EMBO J* 2001;20(22):6414–23.
- Colella M, Pozzan T. Cardiac cell hypertrophy in vitro: role of calcineurin/NFAT as Ca<sup>2+</sup> signal integrators. *Ann NY Acad Sci* 2008;1123:64–8.
- Colella M, Grisan F, Robert V, Turner JD, Thomas AP, Pozzan T. Ca<sup>2+</sup> oscillation frequency decoding in cardiac cell hypertrophy: role of calcineurin/NFAT as Ca<sup>2+</sup> signal integrators. *Proc Natl Acad Sci USA* 2008;105(8):2859–64.
- Hoshijima M, Sah VP, Wang Y, Chien KR, Brown JH. The low molecular weight GTPase Rho regulates myofibril formation and organization in neonatal rat ventricular myocytes. Involvement of Rho kinase. *J Biol Chem* 1998;273(13):7725–30.
- Hunter JJ, Tanaka N, Rockman HA, Ross Jr J, Chien KR. Ventricular expression of a MLC-2v–ras fusion gene induces cardiac hypertrophy and selective diastolic dysfunction in transgenic mice. *J Biol Chem* 1995;270(39):23173–8.
- Bueno OF, De Windt LJ, Tymitz KM, Witt SA, Kimball TR, Klevisky R, et al. The MEK1–ERK1/2 signaling pathway promotes compensated cardiac hypertrophy in transgenic mice. *EMBO J* 2000;19(23):6341–50.
- Wang L, Proud CG. Ras/Erk signaling is essential for activation of protein synthesis by Gq protein-coupled receptor agonists in adult cardiomyocytes. *Circ Res* 2002;91(9):821–9.
- Sanada S, Node K, Minamoto T, Takahima S, Ogai A, Asanuma H, et al. Long-acting Ca<sup>2+</sup> blockers prevent myocardial remodeling induced by chronic NO inhibition in rats. *Hypertension* 2003;41(4):963–7.
- Harris IS, Zhang S, Treskov I, Kovacs A, Weinheimer C, Muslin AJ. Raf-1 kinase is required for cardiac hypertrophy and cardiomyocyte survival in response to pressure overload. *Circulation* 2004;110(6):718–23.
- Purcell NH, Wilkins BJ, York A, Saba-El-Leil MK, Meloche S, Robbins J, Molkenin JD. Genetic inhibition of cardiac ERK1/2 promotes stress-induced apoptosis and heart failure but has no effect on hypertrophy in vivo. *Proc Natl Acad Sci USA* 2007;104(35):14074–9.
- Kehat I, Davis J, Tiburcy M, Accornero F, Saba-El-Leil MK, Maillet M, et al. Extracellular signal-regulated kinases 1 and 2 regulate the balance between eccentric and concentric cardiac growth. *Circ Res* 2011;108(2):176–83.
- Ichida M, Finkel T. Ras regulates NFAT3 activity in cardiac myocytes. *J Biol Chem* 2001;276(5):3524–30.

- [25] Chen PC, Wakimoto H, Conner D, Araki T, Yuan T, Roberts A, et al. Activation of multiple signaling pathways causes developmental defects in mice with a Noonan syndrome-associated *Sos1* mutation. *J Clin Invest* 2010;120(12):4353–65.
- [26] Molkenkin JD, Lu JR, Antos CL, Markham B, Richardson J, Robbins J, Grant SR, Olson EN. A calcineurin-dependent transcriptional pathway for cardiac hypertrophy. *Cell* 1998;93(2):215–28.
- [27] Molkenkin JD, Robbins J. With great power comes great responsibility: using mouse genetics to study cardiac hypertrophy and failure. *J Mol Cell Cardiol* 2009;46(2):130–6.
- [28] Nava C, Hanna N, Michot C, Pereira S, Pouvreau N, Niihori T, et al. Cardio-facio-cutaneous and Noonan syndromes due to mutations in the RAS/MAPK signalling pathway: genotype-phenotype relationships and overlap with Costello syndrome. *J Med Genet* 2007;44(12):763–71.
- [29] Armour CM, Allanson JE. Further delineation of cardio-facio-cutaneous syndrome: clinical features of 38 individuals with proven mutations. *J Med Genet* 2008;45(4):249–54.
- [30] Rodriguez-Viciana P, Tetsu O, Tidyman WE, Estep AL, Conger BA, Cruz MS, et al. Germline mutations in genes within the MAPK pathway cause cardio-facio-cutaneous syndrome. *Science* 2006;311(5765):1287–90.
- [31] Dentici ML, Sarkozy A, Pantaleoni F, Carta C, Lepri F, Ferese R, et al. Spectrum of MEK1 and MEK2 gene mutations in cardio-facio-cutaneous syndrome and genotype-phenotype correlations. *Eur J Hum Genet* 2009;17(6):733–40.
- [32] Rodriguez-Viciana P, Rauen KA. Biochemical characterization of novel germline BRAF and MEK mutations in cardio-facio-cutaneous syndrome. *Meth Enzymol* 2008;438:277–89.
- [33] Ko JM, Kim JM, Kim GH, Yoo HW. PTPN11, SOS1, KRAS, and RAF1 gene analysis, and genotype-phenotype correlation in Korean patients with Noonan syndrome. *J Hum Genet* 2008;53(11–12):999–1006.
- [34] Kobayashi T, Aoki Y, Niihori T, Cavé H, Verloes A, Okamoto N, et al. Molecular and clinical analysis of RAF1 in Noonan syndrome and related disorders: dephosphorylation of serine 259 as the essential mechanism for mutant activation. *Hum Mutat* 2010 Mar;31(3):284–94.
- [35] Gripp KW, Lin AE, Stables DL, Nicholson L, Scott Jr CI, Doyle D, et al. HRAS mutation analysis in Costello syndrome: genotype and phenotype correlation. *Am J Med Genet A* 2006;140(1):1–7.
- [36] Zheng M, Dilly K, Dos Santos Cruz J, Li M, Gu Y, Ursitti JA, et al. Sarcoplasmic reticulum calcium defect in Ras-induced hypertrophic cardiomyopathy heart. *Am J Physiol Heart Circ Physiol* 2004;286(1):H424–33.

---

PUBLICATION III

---

Illaste A, Laasma M, Peterson P, Vendelin M

**Analysis of molecular movement reveals latticelike obstructions to diffusion in heart muscle cells.**

*Biophysical Journal*, 2012, *in press*



# Analysis of molecular movement reveals latticelike obstructions to diffusion in heart muscle cells

Ardo Illaste, Martin Laasmaa, Pearu Peterson and Marko Vendelin\*  
Laboratory of Systems Biology, Institute of Cybernetics, Tallinn University of  
Technology, Estonia

\* corresponding author

Intracellular diffusion in muscle cells is known to be restricted. While characteristics and localization of these restrictions is yet to be elucidated, it has been established that ischemia-reperfusion injury reduces the overall diffusion restriction. Here we apply an extended version of raster image correlation spectroscopy to determine directional anisotropy and coefficients of diffusion in rat cardiomyocytes. Our experimental results indicate that diffusion of a smaller molecule (1127 MW fluorescently labeled ATTO633-ATP) is restricted more than that of a larger one (10000 MW Alexa647-dextran), when comparing diffusion in cardiomyocytes to that in solution. We attempt to provide a resolution to this counterintuitive result by applying a quantitative stochastic model of diffusion. Modeling results suggest the presence of periodic intracellular barriers situated  $\sim 1\mu\text{m}$  apart having very low permeabilities and a small effect of molecular crowding in volumes between the barriers. Such intracellular structuring could restrict diffusion of molecules of energy metabolism, reactive oxygen species and apoptotic signals, enacting a significant role in normally functioning cardiomyocytes as well as in pathological conditions of the heart.

**Keywords:** rat cardiomyocytes; raster image correlation spectroscopy; fluorescence correlation spectroscopy; mathematical modeling

## INTRODUCTION

Of the different processes active in a functioning cell, there are not many which are unaffected by diffusion. The composition, geometry and solvent properties of the intracellular environment determine the characteristics of diffusion for everything from the smallest signalling molecules to enzymes to DNA/RNA. Generally three restrictions for diffusion are considered: viscosity of the fluid phase, binding of the diffusing molecule to other molecules or structures, and molecular crowding which effectively reduces the volume available for diffusion (1). In heart and oxidative skeletal muscle cells diffusion of smaller molecules, such as ADP, has been found to be severely restricted when analyzing kinetics of respiration in permeabilized fibers or cells in respirometer (2, 3), autofluorescence of single cells (4), sarcoplasmic reticulum  $\text{Ca}^{2+}$  ATPase (5), and response of ATP-sensitive  $\text{K}^+$  channel (6). Diffusion restrictions estimated from mitochondrial respiration kinetics have partially been attributed to mito-

chondrial outer membrane (3, 7, 8). In addition to outer membrane and sub-membrane diffusion restrictions (6), there are diffusion obstacles in cardiomyocytes that group ATPases and mitochondria (5). Those diffusion obstacles have been attributed to the regular arrangement of intracellular organelles such as mitochondria (9, 10) leading to anisotropic diffusion in rat cardiomyocytes (11) as well as dependence of apparent diffusion coefficient (DC) on diffusion time in lobster muscle fibers (12). The role of diffusion obstacles in heart regulation is not clear. However, it has been established that ischemia-reperfusion injury reduces the overall diffusion restriction regardless of whether ischemia is induced globally (13) or regionally (14), an effect that can be reduced by ischemic preconditioning (15). Such correlation between the state of the heart muscle and diffusion obstacles suggests that obstacles to diffusion play an important role in regulation of intracellular processes and could be a target of therapies in heart failure treatment.

So far, diffusion restrictions have been suggested from indirect measurements such as kinetics of mitochondrial respiration in permeabilized cells and fibers. Although for larger molecules, diffusion has been found to be significantly restricted (1, 16–18), direct assessment of diffusion in muscle cells has not confirmed the existence of large diffusion restrictions for smaller molecules, for which intracellular DC was found to be  $\sim 2\times$  smaller than in water (19). In experiments performed using  $^{31}\text{P}$ -NMR, a small reduction of DC was observed for ATP and phosphocreatine (PCr) when compared to DC in solution at short diffusion distances. It was found, however, that the transverse DC was dependent on diffusion time (12, 20). To reproduce  $^{31}\text{P}$ -NMR data, it was suggested that the diffusion is mainly restricted by intracellular structures with overall cylindrical orientation (12, 20), such as sarcoplasmic reticulum (12). Such intracellular diffusion obstacles were not identified in a recent  $^{31}\text{P}$ -NMR study of the human calf muscle (21). Large influence of intracellular structures on diffusion of smaller molecules in cytoplasm has not been demonstrated using fluorescence-based methods either.

Recently, we extended raster image correlation spectroscopy (RICS) (22–24) to take into account possible anisotropy of diffusion and determined the diffusion coefficient for fluorescently labelled ATP (11). We found only a small reduction of the DC attributable to anisotropy. In that study, however, several limitations emanated from using a commercial confocal microscope. In particular, using an analog photomultiplier tube as a detector demands that long pixel acquisition times be used to avoid interference between pixels (11, 23). As a result, only a small amount of pixels is acquired at relatively slow laser scanning speeds, limiting correlation analysis to pixels in the same image line. In this paper, we custom built a confocal microscope that allowed us to significantly increase the precision of DC estimation. We determined DCs for two different molecules of different size and found that the diffusion of a larger molecule (Alexa647-dextran 10K) was hindered less than of a smaller one (ATTO633-ATP). To explain such counterintuitive result, we composed a mathematical model that mimics the diffusion pathway in the heart muscle cell and found parameters describing intra-

cellular diffusion obstacles. Whereas our main results are discussed in this text, we provide an extensive Supporting Material giving an introduction to the RICS method; extended experimental and mathematical method descriptions and a section on statistical analysis of model parameter estimates.

## **MATERIALS AND METHODS**

### **Experimental procedures**

Adult outbred Wistar rats of both sexes weighing 300-500g were used in the experiments. Animal procedures were approved by Estonian National Committee for Ethics in Animal Experimentation (Estonian Ministry of Agriculture). Cardiomyocytes (CMs) were isolated as described in (3).

### **Solutions and chemicals**

The following fluorescent dyes were used in this work: ATTO633-ATP (Cat.no:NU-808-633, Jena Bioscience GmbH, Germany), Alexa647-dextran 10K(Cat.no: D-22914, Invitrogen, USA), ATTO655-COOH (Cat.no: AD655-21, ATTO-TEC GmbH, Germany), MitoTracker Green (Cat.no: M-7514, Invitrogen, USA) Mitotracker Green was used in concentration of 0.25  $\mu$ M. Dyes for which DCs were estimated were used in a concentration of 8 nM and 16 nM for ATTO633-ATP and Alexa647-dextran 10K respectively. Solutions are described in detail in the Supporting Material.

### **Determination of diffusion coefficients using RICS**

To perform imaging for RICS, we designed and built a confocal microscope. This allowed us to automate image acquisition under varying laser scanning angles and frequencies. For analysis, triplet states and experimentally obtained point spread function (PSF) were taken into account. See the Supporting Material for the mathematical and experimental details of RICS analysis and for the setup of the confocal microscope.

### **Statistics**

Raw data were analyzed using homemade software. All results are shown as mean  $\pm$  std. dev.

### **Mathematical model**

Stochastic diffusion simulations and data analysis were performed using custom written Python and C++ code on a computational cluster (96 dual-core AMD Opteron 2216 CPU's). Diffusion in three dimensions was simulated to establish independence

of DCs in  $x, y$  and  $z$  directions. A faster 1D model was then used for each spatial direction separately. Diffusion was simulated inside a  $20 \mu\text{m} \times 20 \mu\text{m} \times 5 \mu\text{m}$  region for the 3D model and a  $20 \mu\text{m}$  region for the 1D model. Possible intracellular structures in direction  $\alpha$  ( $\alpha$  represents any of the directions  $x, y$  and  $z$ ) were approximated with periodically placed barriers  $d_\alpha \mu\text{m}$  apart, having permeabilities  $p_\alpha$  (probability for a particle to traverse the wall after an interaction). Diffusion in direction  $\alpha$  in the inter barrier space (IBS) was assumed to be reduced by a factor of  $0 < \lambda_\alpha \leq 1$  compared to that in free intracellular solution. Reduction factors  $\lambda$  were considered to be different for ATTO633-ATP and Alexa647-dextran 10K and for distinct spatial directions. At each timestep  $\Delta t = 1 \mu\text{s}$ , every simulated particle undertook a random displacement in all of the directions  $x, y$  and  $z$ , drawn from a normal distribution  $\mathcal{N}(0, \sqrt{2D_\alpha \Delta t})$ , where  $D_\alpha$  is the DC in direction  $\alpha$ . Timestep value  $1 \mu\text{s}$  was chosen to match pixel acquisition timestep in experiments so as to obtain similar images from the stochastic model. Also, a timestep of  $1 \mu\text{s}$  ensured that diffusing particles would have a very low probability of diffusing out of the PSF during acquisition. This was estimated by using the relation of root mean square displacement to time and diffusion coefficient of the dye in water. If a particle's trajectory intersected with a barrier it had a probability  $p_\alpha$  of passing that barrier and  $1 - p_\alpha$  of bouncing back elastically. Concurrent to simulating diffusion, confocal microscope image acquisition with various scanning speeds and pixel sizes was simulated using in order to obtain images for use in RICS analysis. For the 3D model, analysis methods identical to those used analysing experimental data were used. For the 1D model, theoretical 1D autocorrelation functions used in fitting were derived (see the Supporting Material for details). Obtained apparent DCs in direction  $\alpha$  were functions of barrier parameters  $p_\alpha$ ,  $d_\alpha$  and  $\lambda_\alpha$  values. Comparison of simulated and experimental results yielded sets of model parameters with which simulations for both molecules simultaneously matched experimental data. In subsequent analysis permeability values were reinterpreted as  $\eta$  pores of radius  $R$  per  $\mu\text{m}^2$  of barrier surface. This interpretation required knowledge of radii of the diffusing molecules. These were estimated from DCs in salt solution using the Stokes-Einstein relationship, yielding  $0.92 \text{ nm}$  for the radius of ATTO633-ATP and  $4.1 \text{ nm}$  for Alexa647-dextran 10K.

## RESULTS

### RICS extensions

RICS was extended by using multiple scanning speeds and angles during imaging with the aim of altering the contribution of diffusional anisotropy in acquired images. For image acquisition we used 19 angles uniformly spanning the range from  $0$  to  $360$  degrees. Scanning resolution was altered in tandem with scanning axes rotation. This was all done in a random sequence in order to eliminate bias. As explained in the Supporting Material, these additions were done in order to maximize the amount of data for fitting with theoretical correlation curves.

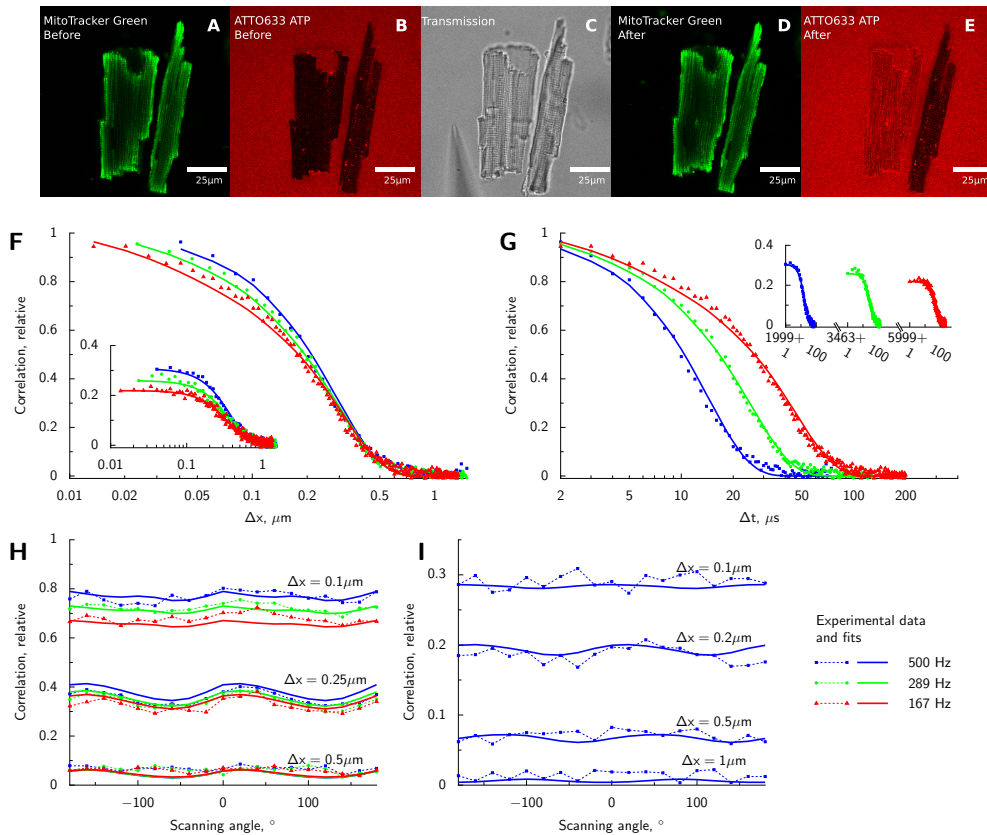


FIGURE 1: Diffusion of ATTO633-ATP in rat CM analyzed by RICS. In the beginning of the experiment, intact rat CMs labeled with Mitotracker Green are positioned into solution containing ATTO633-ATP (confocal images A,B). Since cells are intact, ATTO633-ATP does not penetrate sarcolemma and fluorescence is recorded in solution surrounding the cells as well as T-tubules (B). Holes are introduced into sarcolemma by poking one of the cells with a glass pipette (transmission image of approaching pipette in C). As a result, ATTO633-ATP is able to diffuse into the cell (E) while the structure of the cell is intact (D). RICS analysis is presented in F, G, H, and I. Experimental data (points) acquired at different laser scanning frequencies and directions are fitted by a model (lines). Spatial and temporal components of the correlation function are shown in F and G, respectively. On F and G, imaging was performed with the laser scanning along a line parallel to axis  $x$  at different frequencies (frequencies noted in legend on the right bottom). Correlation along the same line is shown in the main graphs (F,G) while correlation of the signal between pixels in adjacent lines is shown in the insets. Due to the laser backtracking and variation in scan frequencies, temporal component has gaps visible in the inset of G. Due to asymmetry of PSF, laser scanning in different directions leads to modification of correlation function between pixels in the same line (H) and in the adjacent lines (I). Note how the slow component leads to significant correlation in pixels in adjacent lines (I and insets of F and G).

We tested the method by estimating DCs of ATTO633-ATP, Alexa647-dextran 10K

TABLE 1: Diffusion constants ( $D_{TR}$  and  $D_L$  in transverse and longitudinal directions, respectively) obtained from raster image correlation spectroscopy at 26°C. Listed values were obtained in water, measurement solution (solution), or CMs. On the basis of  $n$  experiments, several parameters were determined in addition to diffusion coefficient(s): concentration, triplet time constant  $\tau$  and triplet state contribution  $T$ . Correlations between fluctuation of fluorescence signal were fitted by isotropic model (diffusion coefficient specified only as  $D_{TR}$ ), anisotropic model ( $D_{TR}$  and  $D_L$  specified), or model with two components (Cmp).

Dye	Media	$n$	Cmp.	Concentration nM	Diffusion		Triplet	
					$D_{TR}$ $\mu\text{m}^2/\text{s}$	$D_L$ $\mu\text{m}^2/\text{s}$	$T$ relative	$\tau$ $\mu\text{s}$
ATTO655-COOH	water	4		21±2	454±3		0.08±0.01	3.3±0.1
	water	4		21±2	442±4	483±7	0.08±0.01	3.1±0.1
	solution	4		22±4	362±4		0.10±0.01	4.3±0.7
	solution	4		22±4	348±2	403±10	0.09±0.01	3.8±0.7
ATTO633-ATP	water	4		16±4	326±13		0.10±0.01	4.3±0.1
	water	4		16±4	322±15	337±12	0.10±0.01	4.2±0.1
	solution	4		21±4	195±8		0.14±0.01	5.6±0.3
	solution	4		21±4	183±11	222±3	0.14±0.01	5.5±0.3
	CM	5		86±12	4.0±0.6	4.6±0.9	0.39±0.10	45±5
	CM	5	{ 1 2	19±4 41±10	0.7±0.3 24±6	0.8±0.2 35±8	0.23±0.04	5.2±2.5
Alexa647-dextran10K	water	4		12±3	62±1		0.23±0.01	3.8±0.7
	water	4		12±3	60±2	65±2	0.23±0.01	3.8±0.7
	solution	4		12±2	53±1		0.23±0.00	4.0±0.2
	solution	4		12±2	51±2	57±1	0.23±0.00	4.0±0.2
	CM	7		13±3	16±2	19±3	0.34±0.02	6.6±1.1

and ATTO655-COOH in water and measurement solution. The estimated DC for ATTO655-COOH in water,  $454\pm3 \mu\text{m}^2/\text{s}$  at 26°C, is in good agreement with published data:  $426\pm8 \mu\text{m}^2/\text{s}$  at 25°C (25). Full results are given in Table 1. According to our results, small anisotropy of diffusion (<20%) is not resolvable with this method. Further technical details concerning our extension to RICS can be found in the Supporting Material.

## Experimental results

To determine the intracellular DCs of ATTO633-ATP and Alexa647-dextran 10K, the dye has to be present inside the cell. For both our dyes, which are not able to permeate intact sarcolemma, we used a “poking” procedure demonstrated in Fig.1A-E. In short, we introduced small holes (of diameter  $\sim 1 \mu\text{m}$ ) into the cell membrane with a glass pipette, leading to diffusion of the dye from the surrounding solution into the cell. These small holes were open throughout the experiment resulting in constant exchange of solution with the intracellular environment. For Alexa647-dextran 10K, a higher concentration had to be used in order to get a sufficient signal for RICS analysis.

Representative correlation functions (CFs) estimated for ATTO633-ATP in the cell and the fit with two components are shown in Fig.1 F-I. The two components repre-

sent a slower, bound form of the dye and the freely diffusing form. In case of one component, only the free form is present. See Supporting Material on how the number of components modifies the form of the theoretical CF. Slower diffusion in the cell can be seen from the relatively high correlation (especially when comparing to CFs in water, see the Supporting Material) between pixels in adjacent lines (inset in Fig.1F,G). A slight lack of fit observable in Fig.1F,G is caused by the fact that the fit for only one of the 19 angles recorded in experiment is shown. The optimization process attempts to fit all angles simultaneously (Fig.1H,I), resulting in slight per-angle deviations.

Summary of the DCs determined by anisotropic models is presented in Table 1. Note that when fitting ATTO633-ATP data using a single component model, triplet state time constant increases to more than 40  $\mu\text{s}$  and has a large contribution to the CF (39%). Such triplet state parameters in the fit can be explained by an additional diffusing component that is not accounted for in the single component model. When a two-component model is used, more acceptable triplet state parameters are obtained. In the two component model, contribution of the very slow fraction (probably bound fraction) is  $\sim 30\%$  with the rest attributed to freely moving ATTO633-ATP.

As can be seen from Table 1, the triplet state time constant for Alexa647-dextran 10K in cells is not as large as obtained with single-component model for ATTO633-ATP and the single component fit is sufficient for Alexa647-dextran 10K data. Using saponin permeabilization in lieu of “poking” did not result in markedly different results from Table 1. DCs obtained with saponin permeabilization were  $15 \pm 2 \mu\text{m}^2/\text{s}$  in the transverse and  $19 \pm 1 \mu\text{m}^2/\text{s}$  in the longitudinal directions ( $n=7$ ).

On the basis of our analysis, we conclude that the DC of the freely moving fraction of ATTO633-ATP in CMs is 5.6–8.1 $\times$  reduced (depending on direction) compared to the coefficient in the measurement solution. For Alexa647-dextran 10K, reduction of the DC was considerably smaller: 2.8–3.5 times. Thus, our experimental results indicate, that the diffusion of a smaller molecule is restricted more in the intracellular environment than the larger molecule.

## Analysis by stochastic model

In order to find an explanation for our counterintuitive experimental results, we turned to computational modelling. Diffusion of ATTO633-ATP and Alexa647-dextran 10K was simulated in three dimensions with periodically placed permeable barriers in **x**, **y** and **z** directions using a stochastic computational model (Fig.2A). This geometry was chosen as the simplest and least computationally intensive approximation to intracellular diffusion restrictions. Concurrently with the processes of molecule diffusion and interaction with barriers, confocal microscope data acquisition was simulated and images similar to those in physical experiments were obtained. Apparent diffusion coefficients in the 3 dimensions were calculated from simulated results by applying numerical methods identical to those employed on experimental data. Our goal was to

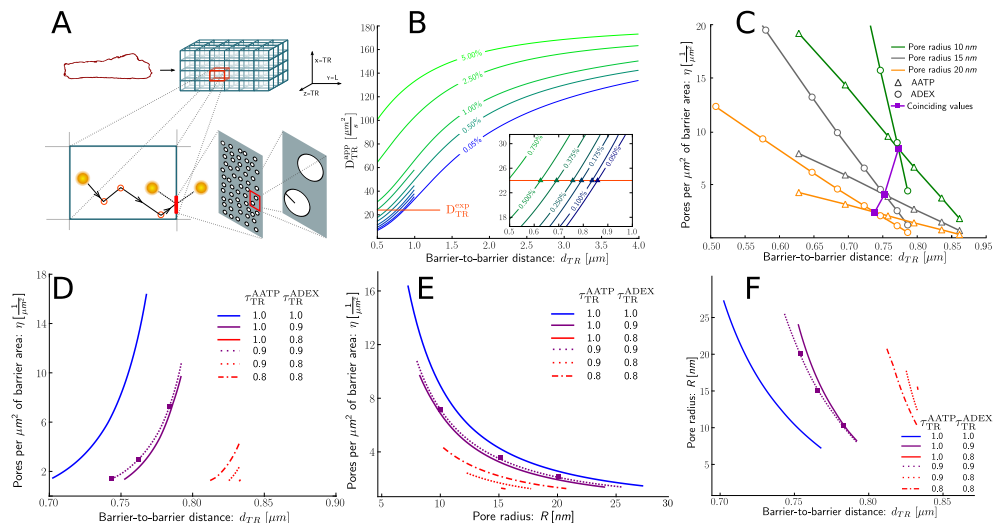


FIGURE 2: Analysis of diffusion in the cell using the stochastic model. (A) Scheme of the computational model. Intracellular structure of the cell (top left) is approximated by a 3D lattice of barriers which hinder molecule diffusion (top right). Barriers are placed, depending on direction  $\alpha$ ,  $d_\alpha$   $\mu m$  apart and have permeabilities  $p_\alpha$ . Diffusion coefficient in the space between barriers is reduced by a factor  $\lambda$  compared to solution ( $0 < \lambda \leq 1$ ). Stochastically diffusing molecules interact with barriers and have a probability  $p_\alpha$  of passing through (bottom left). Permeable barriers correspond to porous walls with  $\eta$  pores of radius  $R$  per  $\mu m^2$  of barrier area (bottom right). Apparent diffusion coefficients are estimated over the entire lattice. (B) Apparent diffusion constant values for ATTO633-ATP are obtained from simulations with varying barrier distances (horizontal axis) and permeabilities (indicated by values on curves). Horizontal solid line shows ATTO633-ATP diffusion coefficient estimated from experiment ( $D_{TR}^{exp}$ ). Inset covers the region  $0.5 \dots 1 \mu m$  where curves intersect with experimental data. Intersection points are marked with triangles. (C) Points of intersection from B with permeability converted to pores per  $\mu m^2$  for different pore radius values (10, 15 and 20 nm). Intersections of ATTO633-ATP ( $\Delta$ ) and Alexa647-dextran 10K ( $\circ$ ) curves of identical pore radius values signify points where model and experiment coincide for both molecules simultaneously ( $\blacksquare$ ). Intersections are curves in 3D space (barrier-to-barrier distance vs. pore radius vs. pores per  $\mu m^2$ ). (D) View of intersection curves from C in barrier-to-barrier distance and pores per  $\mu m^2$  axes. Lines indicate different  $\lambda_{TR}^{AATP}$  and  $\lambda_{TR}^{ADEX}$  values. Squares show the example intersection points from C. (E): Same as D, but for pore radius and pores per  $\mu m^2$  values. (F): Same as D, but for barrier-to-barrier distance and pore radius values. AATP and ADEX represent ATTO633-ATP and Alexa647-dextran 10K, respectively.

determine barrier parameters with which DC values obtained from the model coincide with those from experiments.

The apparent DC estimated by RICS is a macroscopic variable comprised of two components: diffusion in inter-barrier space (IBS) and restrictions from barriers. We assume the  $x$  and  $z$  axis (both represented by the transverse  $TR$  direction) to have identical diffusion restrictions and, consequently, identical barrier parameters. The

y axis corresponds to the longitudinal **L** direction and can have barrier parameters different from the transverse direction.

Barriers in spatial direction  $\alpha$  ( $\alpha$  is **TR** or **L**) are described by two parameters - their permeability ( $p_\alpha$ ) and barrier-to-barrier distance ( $d_\alpha$ ). DC in IBS is reduced compared to solution,  $D_{IBS} = \lambda_\alpha \cdot D_{sol}$ , where the reduction factor  $\lambda_\alpha$  depends on the direction  $\alpha$  and the diffusing molecule. In our simulations we scan IBS diffusion reduction factors in the whole range  $0 \dots 1$  for all directions and molecules.

We estimated apparent DC values ( $D_\alpha^{app}$ ) for various barrier distances, permeabilities and IBS diffusion reduction factors. From calculations performed with the 3D model we determined that diffusion in any spatial direction is dependent on barrier parameters in that direction only and is not affected by the existence or properties of barriers in any orthogonal direction. This allowed us to derive and use a computationally faster 1D RICS model to study diffusion in the transverse and longitudinal directions separately.

Results for simulations performed with  $\lambda_{TR}^{AATP} = 0.9$  are shown in Fig.2B. Points where computational results intersect with the experimentally obtained  $D_{TR}^{exp}$  values give us a combination of barrier parameters in the transverse direction at which the stochastic model is able to reproduce experimental results. Surprisingly, in order for the model to match experimentally obtained  $D_{TR}^{app}$  values, very small permeabilities ( $p < 0.1\%$ ) and closely spaced barriers ( $d < 1\mu m$ ) are necessary.

We performed analogous numerical experiments and analysis for Alexa647-dextran 10K with the intention of: finding parameters where simulation results for both ATTO633-ATP and Alexa647-dextran 10K simultaneously match experimental data; and relating these values to physical barrier characteristics. Permeability values obtained for ATTO633-ATP and Alexa647-dextran 10K are not directly comparable. They can, however, be related to the radius of the diffusing molecule ( $r$ ), the radii of permeable pores in the barriers ( $R$ ) and the number of pores per  $\mu m^2$  ( $\eta$ ) by:  $p = \pi\eta(R - r)^2$  (see the Supporting Material for derivation).

TABLE 2: Diffusion obstacles predicted by stochastic model on the basis of RICS measurements

Barrier	Direction			
	transverse TR (x,z)		longitudinal L (y)	
	min	max	min	max
Distance $d$ [ $\mu m$ ]	$0.68 \pm 0.10$	$0.87 \pm 0.07$	$0.73 \pm 0.13$	$1.02 \pm 0.10$
Pore radius $R$ [ $nm$ ]	$7.4 \pm 2.1$	$30 \pm 8$	$6.7 \pm 1.8$	$38 \pm 10$
Pore density $\eta$ [ $\frac{1}{\mu m^2}$ ]	$1.2 \pm 0.1$	$29 \pm 23$	$1.1 \pm 0.1$	$48 \pm 37$
$\lambda_\alpha^{AATP}$	$0.78 \pm 0.13$	1.0	$0.78 \pm 0.13$	1.0
$\lambda_\alpha^{ADEX}$	$0.77 \pm 0.14$	1.0	$0.77 \pm 0.14$	1.0

Fixing a particular  $R$  value for the pore radius we can convert  $p$  values to  $\eta$  and compare barrier characteristics obtained for ATTO633-ATP and Alexa647-dextran 10K (Fig. 2C). Intersections between ATTO633-ATP and Alexa647-dextran 10K curves now indicate physical parameter values where computational and experimental constraints are satisfied for both molecules simultaneously. By varying  $R$  values we get a range of suitable parameters for a combination of  $\lambda^{AATP}$  and  $\lambda^{ADEX}$  in both transverse and longitudinal directions. Some combinations of  $\lambda^{AATP}$  and  $\lambda^{ADEX}$  do not result in intersections and are therefore discarded as unsuitable. In addition, we assumed that  $\lambda^{AATP} \geq \lambda^{ADEX}$ , as diffusion of larger molecules is restricted more by molecular crowding than the small ones (18).

The relationship between  $R$  and  $\eta$  values in the transverse direction is shown on Fig. 2D,E,F for  $\lambda_{TR}^{AATP}$ ,  $\lambda_{TR}^{ADEX}$  values where intersections occur. Summary of parameters satisfying all constraints is shown in Table 2. Error estimates for the table entries were obtained from Monte Carlo (MC) simulations detailed in the Supporting Material. Data in the table represent the mean and standard deviation obtained from MC simulations. A number of parameter estimates do not follow a normal distribution. For those the mean and standard deviation do not illustrate the actual distribution well and the histograms given in the Supporting Material should be consulted instead. For DC reduction ratio the maximum estimate no error is given as the result was always 100% of the DC in solution for both ATTO633-ATP and Alexa647-dextran 10K.

## DISCUSSION

The major experimental finding of the present study is that the diffusion of the freely moving fraction of a smaller molecule (ATTO633-ATP) is hindered considerably more by intracellular diffusion obstacles than the diffusion of a larger molecule (Alexa647-dextran 10K). In general, fractional reduction of the diffusion coefficient is expected to be larger for larger molecules (18). To explain our counterintuitive result, we assumed that diffusion obstacles are formed by permeable barriers arranged in a 3D lattice. The major finding from numerical simulations performed with this assumption is that such diffusion barriers can reproduce the overall DCs of ATTO633-ATP and Alexa647-dextran 10K estimated from experiments conducted on rat CMs. According to our simulations, the diffusion barriers are  $\leq 1 \mu\text{m}$  apart with relatively few small openings ( $\sim 1 \dots 30$  openings per  $\mu\text{m}^2$  of radius  $7 \dots 30$  nm).

### Intracellular structures acting as diffusion obstacles

Barrier parameters obtained from our computational model imply that only  $\sim 0.3\%$  of barrier surface is covered with pores. Intuitively this would appear a prohibitively small percentage for diffusion to be able to have a significant role in cellular metabolism. However, it can be shown that if there are  $(4R \cdot d)^{-1}$  pores of radius  $R$  per unit area in a barrier that is at distance  $d$  from neighbouring barriers, then the diffusion current

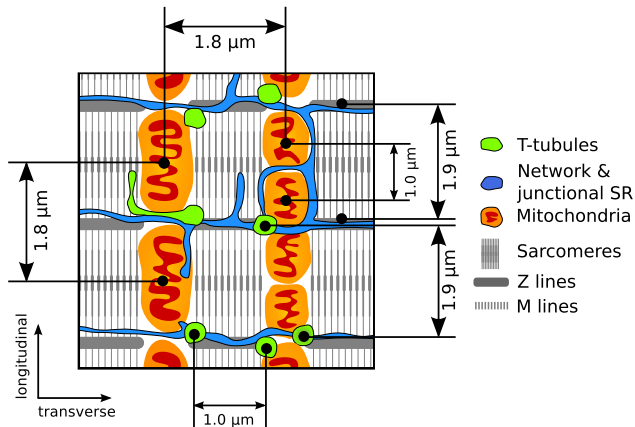


FIGURE 3: Internal structure of the cardiac muscle cell. A regular arrangement of intracellular structures and organelles is present (26–28). Mitochondria are separated  $1.8 \mu\text{m}$  in the transverse direction and  $1.0$  or  $1.8 \mu\text{m}$  (depending on whether there are one or two mitochondria per sarcomere) in the longitudinal direction (9). Sarcomere Z lines are separated by  $1.9 \mu\text{m}$  in the longitudinal direction identically with t-tubules, whereas in the transverse direction t-tubules are  $1.0 \mu\text{m}$  apart on average (29–31).

through the barrier is half of what it would be if there was no barrier at all (32). Substituting our parameters this means that just  $\sim 1.2\%$  of the barrier would need to be penetrable to obtain half maximal diffusion current.

The distances found between barriers are consistent with the morphology of rat CMs (Fig.3). The predicted distance between barriers ( $\sim 0.8 \mu\text{m}$ ) is in agreement with the reported transverse distance between t-tubules (26, 29–31). In transversal direction, the distance between centers of adjacent mitochondria is  $\sim 1.8 \mu\text{m}$  (9) indicating that there are two barriers at this distance. In longitudinal direction, two possible distances between adjacent mitochondria have been found ( $\sim 1 \mu\text{m}$  and  $\sim 1.8 \mu\text{m}$ ) due to the difficulty of distinguishing whether there is one or two mitochondria per sarcomere (9). It is possible to make this distinction, however, from following reactive oxygen species (ROS) induced depolarization of mitochondria. While ROS-induced mitochondrial depolarization typically occurs synchronously for mitochondria within the same sarcomere (33), depolarization of a single mitochondrion with half-sarcomere length can occasionally be observed (34). This suggests that there is a pair of mitochondria per sarcomere with  $\sim 1 \mu\text{m}$  between the centers, similarly to the distance between barriers predicted for longitudinal direction in this work. Thus, distances between diffusion barriers are consistent with the internal periodicity of rat CM morphology.

It is not clear, however, which structures can cause such obstacles to diffusion. It has been shown that internal membranes can have an effect on intracellular diffusion (35). This raises the possibility that in restricting diffusion a role is played by sarcoplasmic reticulum (SR), which can form planular cisternae (26) and invaginate the space between sarcomeres (28), or the t-tubular system, both of which are found

with periodicity (Fig.3) similar to that determined by us. As we found very dense placement of diffusion barriers, we suggest that intracellular proteins in the heart cells could be associated with SR and other inner membrane structures leading to such profound diffusion obstacles. Additionally, enzymes can be associated with M and Z lines of sarcomeres (36, 37). This suggestion is in line with our previous analysis of permeabilized fiber measurements using a 3D mathematical model which predicted very small permeability for restrictions imposed by the SR (8).

### **Model geometry**

The model geometry used by us is not the only one able to explain our experimental data. Other more complex geometries can be conceived and modelled. For example, a geometry with volumes accessible only to the smaller molecule could result in the apparent DC reducing more than the DC of a molecule that can not access these volumes leading to the same paradoxical smaller relative decrease in DC of a larger molecule. Our choice was motivated by the relative simplicity of the geometry employed and, stemming from this, relatively fast computation times. However, already for this basic model, calculations on our cluster of 96 dual core machines took several months. More complex geometries would increase this time manifold. We consider our result not be the definitive indication of wall-like porous barriers in cardiomyocytes, but a useful approximation presenting new questions to be investigated.

### **Diffusion between barriers**

According to Sneyd (38), the reduction factors of diffusion ( $\lambda$ -s) of ATTO633-ATP-sized molecule in sarcomeres are 0.6 and 0.8 in transverse and longitudinal directions, respectively. We consider IBS to contain sarcomeres, mitochondria and free cytosolic space (up to 11 %, (39)) and, based on this, expect hindrance to diffusion in IBS to be less than or equal to that in sarcomeres. As in our study, viscosity in mitochondria has been found to be moderate when intramitochondrial structure with internal membranes is taken into account (40). Our results suggest moderate crowding in IBS leading to a small influence of crowding on kinetics of reactions in the cell. Additionally, our results are in agreement with the small (5-15%) reduction of DC of unbound PCr and ATP in rat skeletal muscle compared to the value in solution, determined by  $^{31}\text{P}$ -NMR diffusion spectroscopy (20).

### **Overall diffusion coefficient**

The overall reduction of DC found in this work was larger than the DC reduction determined in (19). The reasons for the differences in results could be related to our use of larger molecules or the morphological differences between rat CMs and frog skeletal muscle. Reduction of ATTO633-ATP DC was considerably larger than the one we previously found for Alexa647-ATP (11). This is probably due to the use of

dedicated confocal setup in this work, leading to a more accurate determination of CFs used in analysis.

In this paper we were able to use dedicated hardware which allowed us to obtain data at a faster time resolution, which made it possible to fit several lines of the CF, compared to just one line as it was done in (11). Additionally, faster scan speeds that we can now obtain increase the amount of data that can be fitted. We have also included triplet states to the CF analysis, which were missing earlier. Furthermore, in our earlier study, saponin was kept in the solution throughout the experiment. We speculate that all these aspects contribute to the smaller reduction in DC obtained in (11)

While in several studies diffusion of ATP or PCr has been found to be anisotropic in skeletal muscle (12, 20), diffusion of larger molecules has been found to be isotropic in rat CMs (16). Here, diffusion was found to be moderately anisotropic for both studied molecules. As a result, distances and permeabilities of diffusion barriers differed for different directions.

We found that ATTO633-ATP has two components when diffusing in the cell: a bound form and a freely diffusing form. This partitioning is indicated by large triplet state time-constant when using only one component in the fit (Table 1). For Alexa647-dextran 10K only a single, freely diffusing component was necessary. Adding a second component resulted in the slow component having a small contribution to overall signal ( $\sim 5\%$  from total concentration, results not shown). Thus, while properties of the used dyes are different, we compared only freely diffusing components in our analysis which should remove possible bias.

## Used technique

In our analysis we fitted CFs found by RICS using a one- or two-component model, taking into account triplet states of the molecule. During measurements, we varied scanning speed and direction to determine how correlation relates to temporal and spatial components. With this approach, anisotropy of diffusion can be assessed and two DCs can be determined. However, there are several aspects that make the application of our technique non-trivial. For smaller molecules with fast diffusion rates, photon counting detectors are required to increase the number of acquired data points used in fitting. When studying anisotropic diffusion, measurements have to be performed at different scanning angles. Due to the variation of scanning speeds and angles, measurements take a long time, with typical experiments lasting for 2-3 hours. Our measurements were performed on a dedicated microscope with a custom built confocal detection unit that allowed us to automate measurements, to randomize scanning speed and angle sequences to avoid bias, and to track movements of the cell in order to acquire images in the same region. The main advantage of having a custom-built confocal arises from the ability to program it ourselves. Although some commercial confocal software allows writing macros, the extendability of such solu-

tions is limited. While there are several solutions that allow automating aspects of image acquisition on commercial confocal microscopes, we are not aware of any solution that allows the level of control we require. Furthermore, RICS analysis benefits greatly from having a photon counter instead of an analog detector (11, 23). However, we expect that for studying diffusion of larger molecules, commercial microscopes with analog detectors can be adequate and would allow to determine DCs also in an anisotropic case.

When analysing the CFs found in RICS measurements, we used the actual PSF of the optical system (41), rather than approximate analytical functions, as PSF asymmetry was found to influence CF's dependence on scanning direction. In calculations of RICS analysis, knowledge of correlation of fluctuations in concentration is required. This information is conveyed by the so-called propagator, which determines the form of the diffusional correlation term  $G_D$  given in Eq. 2 in Supporting Materials. The propagator is a function that makes it possible to determine the probability of finding a diffusing particle at a distance from the starting position after a given time period. While the propagator for the case pertinent to this work is described by simple analytical functions, it may not always be applicable. For example, when employing anomalous diffusion, one has to find solutions for the fractional Fokker-Planck equation or apply numerical approximations (42) in order to find the propagator. This may be an important limitation that has to be considered when applying our approach.

## Physiological implications

Our results suggest small distances between intracellular barriers to diffusion and a limited amount of holes in them in rat CMs. Such partitioning of the cell may have important physiological and pathophysiological implications. Energy transfer can be influenced if the localization of the barriers is such that ATP-consuming and ATP-producing parts of the cell are separated. Such separation would indicate a prominent role for energy transfer systems, such as the creatine kinase shuttle. Since diffusion restrictions are expected to decrease after ischemia (13, 14), such positioning of barriers could lead to a change in the role of energy transfer system in pathologies. Whether it is consistent with modulation of energy transfer depending on the workload, as shown in the analysis of  $^{31}\text{P}$ -NMR inversion and saturation transfer experiments (43), is not clear and requires further studies. Alternatively, barriers could group ATP-producing and ATP-consuming parts of the cell together, as suggested by coupling between ATPases and mitochondrial respiration (3, 5). In this case, barriers would influence synchronization between different parts of the cell and would restrict local ATP production to local consumption. Prominent diffusion obstacles separating the cell into smaller segments are also consistent with formation of clusters during mitochondrial oscillations (44, 45) and may play an important role in pathologies by restricting diffusion of ROS, apoptosis signals and  $\text{Ca}^{2+}$  waves (46).

## SUPPORTING MATERIAL & CITATIONS

The supporting material contains extra information: a brief overview of the RICS method and our extensions to it; description of experimental methods, including confocal microscope setup; description of the analysis of RICS images and demonstration by analysis of diffusion of molecules in water and measurement solution; description of stochastic computational model together with derivations used to relate barrier permeability to physical parameters of the barrier and molecule size; statistical analysis of model parameters estimation.

References (47–55) appear in the Supporting Material.

## ACKNOWLEDGMENTS

We would like to thank Mervi Sepp and Natalja Jepihhina for providing cardiomyocytes, Merle Mandel for technical assistance, and Rikke Birkedal, Hena R. Ramay, Päävo Simson (all from Laboratory of Systems Biology, Institute of Cybernetics, Tallinn University of Technology, Estonia) and Peeter Illaste for discussions.

## SOURCES OF FUNDING

This work was supported by the Wellcome Trust [Fellowship No. WT081755] and Estonian Science Foundation [grants no 7344 and 8041, PhD stipends for A.I. and M.L. respectively].

## REFERENCES

1. Verkman, A. S., 2002. Solute and macromolecule diffusion in cellular aqueous compartments. *Trends Biochem Sci* 27:27–33.
2. Kümmel, L., 1988. Ca,Mg-ATPase activity of permeabilized rat heart cells and its functional coupling to oxidative phosphorylation of the cells. *Cardiovasc. Res.* 22:359–367.
3. Sepp, M., M. Vendelin, H. Vija, and R. Birkedal, 2010. ADP compartmentation analysis reveals coupling between pyruvate kinase and ATPases in heart muscle. *Biophys J* 98:2785–2793.
4. Jepihhina, N., N. Beraud, M. Sepp, R. Birkedal, and M. Vendelin, 2011. Permeabilized rat cardiomyocyte response demonstrates intracellular origin of diffusion obstacles. *Biophys. J.* 101:2112–2121.
5. Kaasik, A., V. Veksler, E. Boehm, M. Novotova, A. Minajeva, and R. Ventura-Clapier, 2001. Energetic crosstalk between organelles: architectural integration of energy production and utilization. *Circ Res* 89:153–159.
6. Abraham, M. R., V. A. Selivanov, D. M. Hodgson, D. Pucar, L. V. Zingman, B. Wieringa, P. P. Dzeja, A. E. Alekseev, and A. Terzic, 2002. Coupling of cell energetics with membrane metabolic sensing. Integrative signaling through creatine kinase phosphotransfer disrupted by M-CK gene knock-out. *J Biol Chem* 277:24427–24434.

7. Rostovtseva, T. K., K. L. Sheldon, E. Hassanzadeh, C. Monge, V. Saks, S. M. Bezrukov, and D. L. Sackett, 2008. Tubulin binding blocks mitochondrial voltage-dependent anion channel and regulates respiration. *Proc Natl Acad Sci U S A* 105:18746–18751.
8. Ramay, H. R., and M. Vendelin, 2009. Diffusion restrictions surrounding mitochondria: a mathematical model of heart muscle fibers. *Biophys J* 97:443–452.
9. Birkedal, R., H. A. Shiels, and M. Vendelin, 2006. Three-dimensional mitochondrial arrangement in ventricular myocytes: from chaos to order. *Am J Physiol Cell Physiol* 291:C1148–C1158.
10. Vendelin, M., N. Beraud, K. Guerrero, T. Andrienko, A. Kuznetsov, J. Olivares, L. Kay, and V. A. Saks, 2005. Mitochondrial regular arrangement in muscle cells: a 'crystal-like' pattern. *Am J Physiol Cell Physiol* 288:C757–C767.
11. Vendelin, M., and R. Birkedal, 2008. Anisotropic diffusion of fluorescently labeled ATP in rat cardiomyocytes determined by raster image correlation spectroscopy. *Am J Physiol Cell Physiol* 295:C1302–C1315.
12. Kinsey, S. T., and T. S. Moerland, 2002. Metabolite diffusion in giant muscle fibers of the spiny lobster *Panulirus argus*. *J Exp Biol* 205:3377–3386.
13. Kay, L., V. A. Saks, and A. Rossi, 1997. Early alteration of the control of mitochondrial function in myocardial ischemia. *J Mol Cell Cardiol* 29:3399–3411.
14. Boudina, S., M. N. Laclau, L. Tariosse, D. Daret, G. Gouverneur, S. Bonoron-Adele, V. A. Saks, and P. D. Santos, 2002. Alteration of mitochondrial function in a model of chronic ischemia in vivo in rat heart. *Am J Physiol Heart Circ Physiol* 282:H821–H831.
15. Laclau, M. N., S. Boudina, J. B. Thambo, L. Tariosse, G. Gouverneur, S. Bonoron-Adele, V. A. Saks, K. D. Garlid, and P. D. Santos, 2001. Cardioprotection by ischemic preconditioning preserves mitochondrial function and functional coupling between adenine nucleotide translocase and creatine kinase. *J Mol Cell Cardiol* 33:947–956.
16. Papadopoulos, S., V. Endeward, B. Revesz-Walker, K. D. Jürgens, and G. Gros, 2001. Radial and longitudinal diffusion of myoglobin in single living heart and skeletal muscle cells. *Proc Natl Acad Sci U S A* 98:5904–5909.
17. Papadopoulos, S., K. D. Jürgens, and G. Gros, 2000. Protein diffusion in living skeletal muscle fibers: dependence on protein size, fiber type, and contraction. *Biophys J* 79:2084–2094.
18. Muramatsu, N., and A. P. Minton, 1988. Tracer diffusion of globular proteins in concentrated protein solutions. *Proc Natl Acad Sci U S A* 85:2984–2988.
19. Kushmerick, M. J., and R. J. Podolsky, 1969. Ionic mobility in muscle cells. *Science* 166:1297–1298.
20. de Graaf, R. A., A. van Kranenburg, and K. Nicolay, 2000. In vivo (31)P-NMR diffusion spectroscopy of ATP and phosphocreatine in rat skeletal muscle. *Biophys J* 78:1657–1664.
21. Gabr, R., A. El-Sharkawy, M. Schar, R. Weiss, and P. Bottomley, 2011. High-energy phosphate transfer in human muscle: diffusion of phosphocreatine. *Am. J. Physiol. Cell. Physiol.* 301:C234–C241.
22. Digman, M. A., C. M. Brown, P. Sengupta, P. W. Wiseman, A. R. Horwitz, and E. Gratton, 2005. Measuring fast dynamics in solutions and cells with a laser scanning microscope. *Biophys J* 89:1317–1327.
23. Brown, C. M., R. B. Dalal, B. Hebert, M. A. Digman, A. R. Horwitz, and E. Gratton, 2008. Raster image correlation spectroscopy (RICS) for measuring fast protein dynamics and concentrations with a commercial laser scanning confocal microscope. *J Microsc* 229:78–91.

24. Rossow, M. J., J. M. Sasaki, M. A. Digman, and E. Gratton, 2010. Raster image correlation spectroscopy in live cells. *Nat Protoc* 5:1761–1774.
25. Müller, C. B., A. Loman, V. Pacheco, F. Koberling, D. Willbold, W. Richtering, and J. Enderlein, 2008. Precise measurement of diffusion by multi-color dual-focus fluorescence correlation spectroscopy. *EPL (Europhysics Letters)* 83:46001.
26. Hayashi, T., M. Martone, Z. Yu, A. Thor, M. Doi, M. Holst, M. Ellisman, and M. Hoshijima, 2009. Three-dimensional electron microscopy reveals new details of membrane systems for Ca<sup>2+</sup> signaling in the heart. *J. Cell Sci.* 122:1005.
27. Fawcett, D., and N. McNutt, 1969. The ultrastructure of the cat myocardium. *J. Cell. Biol.* 42:1.
28. Muir, A., 1967. The effects of divalent cations on the ultrastructure of the perfused rat heart. *Journal of Anatomy* 101:239.
29. Chen-Izu, Y., S. McCulle, C. Ward, C. Soeller, B. Allen, C. Rabang, M. Cannell, C. Balke, and L. Izu, 2006. Three-dimensional distribution of ryanodine receptor clusters in cardiac myocytes. *Biophys. J.* 91:113.
30. Salnikov, V., Y. Lukyanenko, W. Lederer, and V. Lukyanenko, 2009. Distribution of ryanodine receptors in rat ventricular myocytes. *J. Muscle Res. Cell. Motil.* 30:161170.
31. Soeller, C., and M. Cannell, 1999. Examination of the transverse tubular system in living cardiac rat myocytes by 2-photon microscopy and digital imageprocessing techniques. *Circ. Res.* 84:266.
32. Berg, H., 1993. Random walks in biology. Princeton Univ Pr.
33. Zorov, D. B., C. R. Filburn, L. O. Klotz, J. L. Zweier, and S. J. Sollott, 2000. Reactive oxygen species (ROS)-induced ROS release: a new phenomenon accompanying induction of the mitochondrial permeability transition in cardiac myocytes. *J Exp Med* 192:1001–1014.
34. Juhaszova, M., D. B. Zorov, S.-H. Kim, S. Pepe, Q. Fu, K. W. Fishbein, B. D. Ziman, S. Wang, K. Ytrehus, C. L. Antos, E. N. Olson, and S. J. Sollott, 2004. Glycogen synthase kinase-3 $\beta$  mediates convergence of protection signaling to inhibit the mitochondrial permeability transition pore. *J Clin Invest* 113:1535–1549.
35. Novak, I. L., P. Kraikivski, and B. M. Slepchenko, 2009. Diffusion in cytoplasm: effects of excluded volume due to internal membranes and cytoskeletal structures. *Biophys J* 97:758–767.
36. Wegmann, G., E. Zanolla, H. M. Eppenberger, and T. Wallimann, 1992. In situ compartmentation of creatine kinase in intact sarcomeric muscle: the acto-myosin overlap zone as a molecular sieve. *J Muscle Res Cell Motil* 13:420–435.
37. Sullivan, D. T., R. MacIntyre, N. Fuda, J. Fiori, J. Barrilla, and L. Ramizel, 2003. Analysis of glycolytic enzyme co-localization in Drosophila flight muscle. *J Exp Biol* 206:2031–2038.
38. Shorten, P., and J. Sneyd, 2009. A mathematical analysis of obstructed diffusion within skeletal muscle. *Biophys. J.* 96:47644778.
39. Page, E., 1978. Quantitative ultrastructural analysis in cardiac membrane physiology. *Am J Physiol Cell Physiol* 235:C147.
40. Dieteren, C. E. J., S. C. A. M. Gielen, L. G. J. Nijtmans, J. A. M. Smeitink, H. G. Swarts, R. Brock, P. H. G. M. Willems, and W. J. H. Koopman, 2011. Solute diffusion is hindered in the mitochondrial matrix. *Proc Natl Acad Sci U S A* 108:8657–8662.
41. Laasmaa, M., M. Vendelin, and P. Peterson, 2011. Application of regularized Richardson-Lucy algorithm for deconvolution of confocal microscopy images. *J Microsc* 243:124–140.

42. Weiss, M., M. Elsner, F. Kartberg, and T. Nilsson, 2004. Anomalous subdiffusion is a measure for cytoplasmic crowding in living cells. *Biophys J* 87:3518–3524.
43. Vendelin, M., J. A. Hoerter, P. Mateo, S. Soboll, B. Gillet, and J.-L. Mazet, 2010. Modulation of energy transfer pathways between mitochondria and myofibrils by changes in performance of perfused heart. *J Biol Chem* 285:37240–37250.
44. Romashko, D. N., E. Marban, and B. O'Rourke, 1998. Subcellular metabolic transients and mitochondrial redox waves in heart cells. *Proc Natl Acad Sci U S A* 95:1618–1623.
45. Kurz, F. T., M. A. Aon, B. O'Rourke, and A. A. Armoundas, 2010. Spatio-temporal oscillations of individual mitochondria in cardiac myocytes reveal modulation of synchronized mitochondrial clusters. *Proc Natl Acad Sci U S A* 107:14315–14320.
46. Venetucci, L., A. Trafford, S. O'Neill, and D. Eisner, 2008. The sarcoplasmic reticulum and arrhythmogenic calcium release. *Cardiovasc. Res.* 77:285–292.
47. Elson, E., 2011. Fluorescence Correlation Spectroscopy: Past, Present, Future. *Biophys. J.* 101:2855–2870.
48. Haustein, E., and P. Schwille, 2007. Fluorescence correlation spectroscopy: novel variations of an established technique. *Annu. Rev. Biophys. Biomol. Struct.* 36:151–169.
49. Lakowicz, J., 2006. Principles of fluorescence spectroscopy. Springer.
50. Thompson, N., 2002. Fluorescence Correlation Spectroscopy. In J. Lakowicz, C. D. Geddes, and J. R. Lakowicz, editors, Topics in Fluorescence Spectroscopy, Springer US, volume 1 of *Topics in Fluorescence Spectroscopy*, 337–378.
51. Gröner, N., J. Capoulade, C. Cremer, and M. Wachsmuth, 2010. Measuring and imaging diffusion with multiple scan speed image correlation spectroscopy. *Opt. Express* 18:21225.
52. Krichevsky, O., and G. Bonnet, 2002. Fluorescence correlation spectroscopy: the technique and its applications. *Reports on Progress in Physics* 65:251.
53. Widengren, J., U. Mets, and R. Rigler, 1995. Fluorescence correlation spectroscopy of triplet states in solution: a theoretical and experimental study. *J Phys Chem* 99:13368–13379.
54. Moré, J. J., D. C. Sorensen, K. E. Hillstrom, and B. S. Garbow, 1984. The MINPACK Project. In W. J. Cowell, editor, Sources and Development of Mathematical Software, Prentice-Hall.
55. Dertinger, T., V. Pacheco, I. von der Hocht, R. Hartmann, I. Gregor, and J. Enderlein, 2007. Two-focus fluorescence correlation spectroscopy: a new tool for accurate and absolute diffusion measurements. *Chemphyschem* 8:433–443.

## Supporting material:

### Analysis of molecular movement reveals latticelike obstructions to diffusion in heart muscle cells

Ardo Illaste, Martin Laasmaa, Pearu Peterson and Marko Vendelin  
Laboratory of Systems Biology, Institute of Cybernetics, Tallinn University of  
Technology, Estonia

The supporting material is split into several sections. First, a brief overview of the RICS method and our extensions to it is given. Second, description of experimental methods, including confocal microscope setup is presented. Then, description of the analysis of RICS images is described and demonstrated by analyzing diffusion of molecules in water and measurement solution. Forth, description of stochastic computational model is given together with derivations used to relate barrier permeability to physical parameters of the barrier and molecule size. Lastly statistical analysis of model parameters estimation is presented.

#### Contents

<b>1 Raster image correlation spectroscopy</b>	<b>S2</b>
1.1 Basics . . . . .	S2
1.2 Time delay between pixels . . . . .	S5
1.3 Motivation for modifications . . . . .	S6
1.4 Changes in scanning angle . . . . .	S6
1.5 Scanning resolution . . . . .	S7
1.6 Two diffusing species . . . . .	S7
1.7 Triplet states . . . . .	S8
1.8 Full form of correlation function . . . . .	S8
<b>2 Detailed methods</b>	<b>S8</b>
2.1 Confocal setup . . . . .	S8
2.2 Determination of diffusion coefficients using RICS . . . . .	S10
2.3 Solutions . . . . .	S11
<b>3 Mathematical model</b>	<b>S12</b>
3.1 Relation of barrier permeability to barrier and molecule properties . . . . .	S12
3.2 Theoretical correlation function for 1D RICS . . . . .	S15
<b>4 Supporting results</b>	<b>S16</b>
4.1 RICS extensions . . . . .	S16
4.2 Diffusion obstacle parameter sensitivity . . . . .	S19
<b>Supporting references</b>	<b>S23</b>

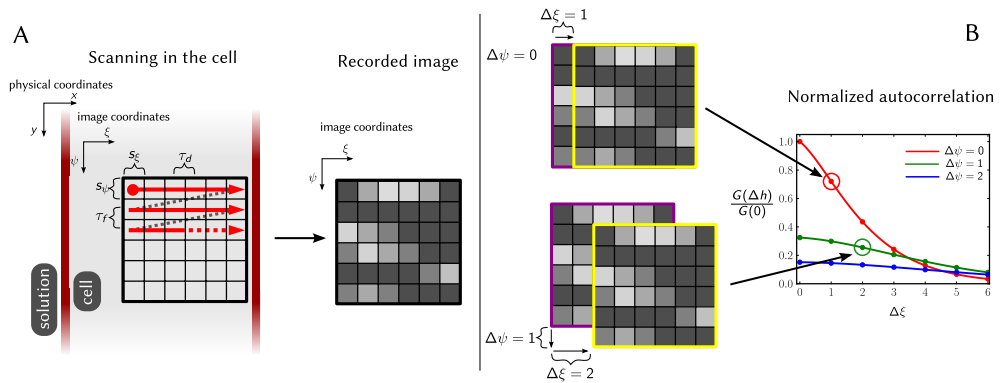


FIGURE S1: Explanation of the RICS protocol.(A) A raster image consisting of a grid of pixels is acquired within a cell. Pixels are separated by  $s_\xi, s_\psi$   $\mu\text{m}$  spatially and by  $\tau_d, n_\xi \times \tau_d + \tau_f$   $\mu\text{s}$  temporally in the  $\xi$  and  $\psi$  directions, respectively. In the default case the image coordinates  $\xi, \psi$  align with the physical coordinates  $x, y$ . The image obtained shows traces of diffusing molecules within the cell. (B)The CF  $G(\boldsymbol{\rho})$  for the shift  $\boldsymbol{\rho} = (\Delta\xi, \Delta\psi)$  is calculated by shifting a copy of the original image, multiplying the fluorescence values and averaging over the entire image. Arrows indicate the location of the correlation value for the shifts shown. The CF here is normalized to the zero-shift correlation  $G(0)$  from Eq.7

## 1 RASTER IMAGE CORRELATION SPECTROSCOPY

### 1.1 Basics

Raster image correlation spectroscopy (RICS) is based on merging the concepts of scanning confocal microscopy, FCS and image correlation spectroscopy (1, 2). While more detailed reviews are available covering the method and how it relates to other FCS-based methods (3, 4), we here present a brief overview of the concepts behind RICS and to our modification to this method.

The fundamental idea behind RICS is the realization that in an image obtained by a laser scanning confocal microscope, pixels on the image are not only separated in space but also in time (2). Photons emitted by excited fluorescent molecules are recorded as raster images as the mirrors scan the laser beam on the specimen. When recording a two dimensional raster image, the laser beam moves along one image axis ( $\xi$ ), spending  $\tau_d$  seconds acquiring each pixel on the line (dwell time), then flies back to the beginning of the line with flyback time  $\tau_f$ , moves one pixel forward in the other axis ( $\psi$ ) and records the second line. This sequential processes is repeated until the whole image has been scanned line by line (Fig. S1A), resulting in a rectangular grid of pixels separated in space and time. By calculating the correlation function (CF) of the scanned image it is possible to extract information about the space-time relationship between the pixels and to characterize, for example, reaction kinetics, translational and rotational diffusion, conformational dynamics, molecular flow, etc. (3–5). This can be done by fitting experimentally obtained CFs with theo-

retical CFcurves derived for the phenomenon being observed. In this paper we focus on applying RICS on analysis of diffusion of fluorescent dyes.

The correlation function  $G(\Delta\xi, \Delta\psi, \Delta\zeta)$  indicates the similarity of an image to a copy of itself shifted by  $\Delta\xi$  in the  $\xi$  direction,  $\Delta\psi$  in the  $\psi$  direction (see Fig. S1B) and, in case a 3D stack of images is analyzed,  $\Delta\zeta$  in the  $\zeta$  direction (otherwise  $\Delta\zeta = 0$ ).

The CF for a given shift is calculated by multiplying the fluorescence values in the original image with values in the shifted image and averaging over all the pixels. The result is normalized to average image fluorescence squared:

$$G(\Delta\xi, \Delta\psi, \Delta\zeta) = \frac{\langle F(\xi, \psi, \zeta) \cdot F(\xi + \Delta\xi, \psi + \Delta\psi, \zeta + \Delta\zeta) \rangle_{\xi, \psi, \zeta}}{\langle F \rangle_{\xi, \psi, \zeta}^2} - 1, \quad (1)$$

where  $\langle \dots \rangle$  signifies averaging over the whole image.

The CF can also be calculated in terms of fluorescence fluctuations from the average  $\delta F = F - \langle F \rangle$  by substituting  $F = \delta F + \langle F \rangle$  into Eq.1:

$$G(\Delta\xi, \Delta\psi, \Delta\zeta) = \frac{\langle \delta F(\xi, \psi, \zeta) \cdot \delta F(\xi + \Delta\xi, \psi + \Delta\psi, \zeta + \Delta\zeta) \rangle_{\xi, \psi, \zeta}}{\langle F \rangle_{\xi, \psi, \zeta}^2}.$$

It is more convenient to present the CF in vector form with image shift vector  $\boldsymbol{\rho} = [\Delta\xi, \Delta\psi, \Delta\zeta]$  and position vector  $\mathbf{h} = [\xi, \psi, \zeta]$ :

$$G(\boldsymbol{\rho}) = \frac{\langle \delta F(\mathbf{h}) \cdot \delta F(\mathbf{h} + \boldsymbol{\rho}) \rangle_{\mathbf{h}}}{\langle F \rangle_{\mathbf{h}}^2}. \quad (2)$$

The physical coordinates corresponding to image coordinates  $\mathbf{h}$  are  $\mathbf{p} = \mathbf{p}_0 + \mathbf{h}\mathbf{S}$ . Here,  $\mathbf{p}_0$  is the physical location at the 0-th pixel and  $\mathbf{S} = \text{diag}(s_\xi, s_\psi, s_\zeta)$  is a diagonal matrix containing pixel sizes in each image dimension. Shift  $\boldsymbol{\rho}$  in image coordinates converts to a shift  $\mathbf{q} = [\Delta x, \Delta y, \Delta z]$  in the physical coordinate system:

$$\begin{aligned} \mathbf{q}(\boldsymbol{\rho}) &= \boldsymbol{\rho}\mathbf{S} = [\Delta\xi, \Delta\psi, \Delta\zeta] \begin{pmatrix} s_\xi & 0 & 0 \\ 0 & s_\psi & 0 \\ 0 & 0 & s_\zeta \end{pmatrix} \\ &= [\Delta\xi \cdot s_\xi, \Delta\psi \cdot s_\psi, \Delta\zeta \cdot s_\zeta] = [\Delta x, \Delta y, \Delta z]. \end{aligned}$$

For simplicity we consider that the fluorescence signal recorded at location  $\mathbf{p}$  is obtained from the convolution of the point spread function (PSF) of the microscope and the concentration of the fluorescent dye ( $c$ ) in the PSF volume.

$$F(\mathbf{p}) = B \int W(\mathbf{r}) \cdot c(\mathbf{p} - \mathbf{r}) \, d\mathbf{r},$$

where  $W$  is the PSF and  $B$  a parameter called brightness given by  $B = q\sigma Q$  (5). Here  $q$  is the quantum efficiency of detecting emitted photons,  $\sigma$  the cross-section of absorption and  $Q$  the emission quantum yield of the fluorescent molecule. Employing this relationship between recorded fluorescence and concentration, Eq.2 can be used to connect the fluctuations of fluorescence visible on the recorded image to fluctuations in concentration of the diffusing dye:

$$\begin{aligned} G(\boldsymbol{\varrho}) &= \frac{\langle \delta F(\mathbf{p}) \cdot \delta F(\mathbf{p} + \mathbf{q}(\boldsymbol{\varrho})) \rangle_{\mathbf{p}}}{\langle F(\mathbf{p}) \rangle_{\mathbf{p}}^2} \\ &= \frac{1}{\langle c(\mathbf{p}) \rangle_{\mathbf{p}}^2} \iint W(\mathbf{r})W(\mathbf{r}')G_D(\mathbf{r}, \mathbf{r}', \boldsymbol{\varrho}) \, d\mathbf{r} \, d\mathbf{r}'. \end{aligned} \quad (3)$$

$G_D$  is the correlation due to diffusion and can be calculated analytically (6):

$$\begin{aligned} G_D(\mathbf{r}, \mathbf{r}', \boldsymbol{\varrho}) &= \langle \delta c(\mathbf{p} + \mathbf{r}) \cdot \delta c(\mathbf{p} + \mathbf{r}' + \mathbf{q}(\boldsymbol{\varrho})) \rangle_{\mathbf{p}} \\ &= \langle c \rangle \prod_{i=1}^n (4\pi D_i)^{-\frac{1}{2}} \exp\left(-\frac{(r'_i + q_i - r_i)^2}{4D_i t(\boldsymbol{\varrho})}\right), \end{aligned} \quad (4)$$

where  $\delta c(\mathbf{p})$  is the fluctuation in concentration of the fluorescent dye at location  $\mathbf{p}$ ,  $\langle c \rangle$  is the average concentration,  $D_i$  are diagonal components of the diffusion tensor in the coordinate system composed of principal axes, collected here into  $\mathbf{D} = [D_x, D_y, D_z]$ . If diffusion is isotropic then all components in  $\mathbf{D}$  are equal. In the case of anisotropic diffusion, components of  $\mathbf{D}$  can have different values. The time delay  $t(\boldsymbol{\varrho})$  indicates how much time has passed between acquisition of two pixels separated by the shift  $\boldsymbol{\varrho}$ . The number  $n$  indicates the number of dimensions and in general  $n = 3$ . The equations are still valid, however, for other  $n$  values as well.

Although the PSF is dependent on the microscope and should be measured experimentally, an analytic estimate is often used (5, 6):

$$W(\mathbf{r}) = \prod_{i=1}^n \exp\left(-2\frac{r_i^2}{w_i^2}\right) \quad (5)$$

Here,  $\mathbf{w}$  is a vector describing the width of the PSF in spatial directions. It is customary to perform calibrations using a fluorescent molecule with a known concentration in order to determine the  $\mathbf{w}$  values. Furthermore, the  $x$  and  $y$  components of  $\mathbf{w}$  are often assumed to be equal.

Using the PSF definition from Eq.5 and  $G_D$  from Eq.4 the integrals in Eq.2 can be

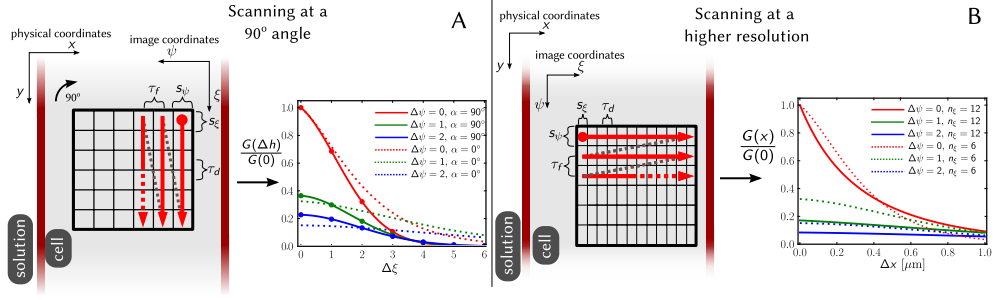


FIGURE S2: Modified scanning for RICS. (A) Scanning at an angle  $\alpha$  rotates the image coordinates with respect to the physical coordinates and results in a different CF which can be used for determining anisotropy of diffusion. The CF for  $0^\circ$  angle scanning from Fig. S1B is shown in dotted lines and differs from the CF obtained for an image scanned at a different angle. In the shown example, scanning is performed at a  $90^\circ$  angle, effectively aligning the image  $\xi$  axis with the physical  $y$  axis and image  $\psi$  axis with physical  $x$  axis. (B) Changing the scanning resolution also alters the shape of the CF. In the example shown, the image is scanned at two times higher resolution resulting in the CF depicted with solid lines. Since the pixel dwell time  $\tau_d$  is not changed, scanning one line takes two times longer. For comparison, the CF from Fig. S1B is shown in dotted lines. The horizontal axis now shows physical shift values in  $\mu\text{m}$  since the pixel size and count for the two CF-s is different.

calculated and the following analytic form obtained:

$$G(\boldsymbol{\rho}) = \frac{1}{\langle c \rangle} \prod_{i=1}^n \left[ \frac{1}{\sqrt{\pi (4D_i t(\boldsymbol{\rho}) + w_i^2)}} \cdot \exp\left(-\frac{q(\boldsymbol{\rho})_i^2}{4D_i t(\boldsymbol{\rho}) + w_i^2}\right) \right]. \quad (6)$$

From this result it can be seen that with zero shift (i.e.,  $\boldsymbol{\rho} = (0, 0, 0)$ ) the CF gives:

$$G(0) = \frac{1}{\langle c \rangle} \prod_{i=1}^n \frac{1}{\sqrt{\pi} w_i}. \quad (7)$$

As  $G(0)$  is independent of the diffusion of the fluorescent molecule it can be used to determine the global concentration of the molecule or, knowing that, the properties of the PSF (i.e., components of  $\mathbf{w}$ ).

## 1.2 Time delay between pixels

Scanning a 2D raster image with  $n_\xi$  pixels in the  $\xi$  direction, with  $\tau_d$  seconds used as the dwell time for all pixels and  $\tau_f$  being the time that it takes for the beam to move from the end of one line to the beginning of the next, the time delay between two pixels separated by the shift  $\boldsymbol{\rho}$  used in Eqs. 6 and 9 is:

$$t(\boldsymbol{\rho}) = t(\Delta\xi, \Delta\psi) = \Delta\xi \cdot \tau_d + \Delta\psi \cdot (n_\xi \cdot \tau_d + \tau_f). \quad (8)$$

Inserting this relation in the CF Eqs. 6 and 9 will yield the function that can be used for fitting experimentally obtained data and obtaining diffusion coefficients.

### 1.3 Motivation for modifications

As we have demonstrated, RICS can be used to determine anisotropy of diffusion by varying the time delay between physical location in the sample during a scan. This can be achieved by altering the angle of scanning (7).

Also, diffusion dependent changes in the CF can be subtle, making them hard to detect and fit, especially with noisy data. Through changes in scanning resolution additional aspects of the CF can be estimated, leading to a larger amount of datapoints available for fitting.

### 1.4 Changes in scanning angle

In order to detect anisotropy of diffusion, several scanning angles can be used to alter the time delay between pixels acquired from the same location (7). When scanning is performed at an angle  $\alpha$  relative to the physical coordinate axes, the CF equations need to be modified to account for this. For example, if scanning is performed under a  $90^\circ$  angle, the image  $\xi$  and  $\psi$  axes actually correspond to the physical  $y$  and  $x$  axes, respectively (see Fig. S2A). The CF that takes the scanning angle into account is:

$$G(\boldsymbol{\rho}, \alpha) = \frac{1}{\langle c \rangle} \prod_{i=1}^n \left[ \frac{1}{\sqrt{\pi (4D_i t(\boldsymbol{\rho}) + w_i^2)}} \cdot \exp \left( -\frac{q(\boldsymbol{\rho}, \alpha)_i^2}{4D_i t(\boldsymbol{\rho}) + w_i^2} \right) \right], \quad (9)$$

where the physical shift  $\mathbf{q}$  is now a function of the rotation angle  $\alpha$ :

$$\mathbf{q}(\boldsymbol{\rho}, \alpha) = \boldsymbol{\rho} \mathbf{S} (\mathbf{M}(\alpha))^T \quad (10)$$

$\mathbf{M}(\alpha)$  is the rotation matrix for rotation angle  $\alpha$ . For rotating around the  $z$  axis, as is done in this paper, the rotation matrix is:

$$\mathbf{M}(\alpha) = \begin{pmatrix} \cos \alpha & -\sin \alpha & 0 \\ \sin \alpha & \cos \alpha & 0 \\ 0 & 0 & 1 \end{pmatrix}.$$

It is possible to do rotations around another axis or even multiple rotations around different axes by inserting a suitable rotation matrix in Eq.10 (assuming that the microscope employed is able to perform such scans).

The physical shift vector from Eq.10 for rotation  $\alpha$  around the  $z$  axis is:

$$\begin{aligned}
 \mathbf{q}(\boldsymbol{\rho}, \alpha) &= [\Delta x, \Delta y, \Delta z] \\
 &= \boldsymbol{\rho} \mathbf{S} (\mathbf{M}(\alpha))^T \\
 &= \begin{pmatrix} \Delta \xi \cdot s_\xi \\ \Delta \psi \cdot s_\psi \\ \Delta \zeta \cdot s_\zeta \end{pmatrix}^T \begin{pmatrix} \cos \alpha & \sin \alpha & 0 \\ -\sin \alpha & \cos \alpha & 0 \\ 0 & 0 & 1 \end{pmatrix} \\
 &= \begin{pmatrix} \Delta \xi \cdot s_\xi \cdot \cos \alpha - \Delta \psi \cdot s_\psi \cdot \sin \alpha \\ \Delta \xi \cdot s_\xi \cdot \sin \alpha + \Delta \psi \cdot s_\psi \cdot \cos \alpha \\ \Delta \zeta \cdot s_\zeta \end{pmatrix}^T.
 \end{aligned}$$

It is easy to verify that when  $\alpha = 0$ ,  $\mathbf{M}$  reduces to the identity matrix and Eq.9 simplifies to Eq.6.

### 1.5 Scanning resolution

Changes in scanning resolution (7) or pixel dwell time  $\tau_d$  (8) will alter the time delay function Eq.8 and result in different correlation curves. An example for scanning with double resolution but unchanged pixel dwell time  $\tau_d$  in  $\xi$  axis is shown on Fig. S2B. An increased resolution increases the time taken to record a line and decreases pixel size. Therefore, in order to compare the CF for different resolutions it is more suitable to present them as functions of physical distance as is done in Fig. S2B.

### 1.6 Two diffusing species

It is possible for the fluorescent molecule to bind with other, larger, molecules in the intracellular solution. As a result, two subspecies of the fluorescent molecule would be diffusing in the cell: the faster unbound form and the slower bound form. Assuming that fluorescent properties of the dye are not altered as a result of binding and that the two species are non-interacting (i.e., the binding/unbinding is relatively slow), the CF for two species diffusing is (5, 9) :

$$\begin{aligned}
 G(\boldsymbol{\rho}, \alpha) &= \frac{1}{\langle c_1(\mathbf{p}) + c_2(\mathbf{p}) \rangle_{\mathbf{p}}^2} \\
 &\cdot \iint W(\mathbf{r}) W(\mathbf{r}') (\langle c_1 \rangle \cdot g_{D1} + \langle c_2 \rangle \cdot g_{D2}) \, d\mathbf{r} \, d\mathbf{r}', \quad (11)
 \end{aligned}$$

where  $\langle c_1 \rangle$ ,  $\langle c_2 \rangle$  are concentrations of the two components and  $g_{D1}$  and  $g_{D2}$  are given by  $G_{Dk}(\mathbf{r}, \mathbf{r}', \boldsymbol{\rho}, \alpha) / \langle c_k \rangle$ , ( $k = 1, 2$ ). Inserting the gaussian PSF given in Eq.5 to

calculate the CF for two components from Eq.11:

$$G(\boldsymbol{\rho}, \alpha) = \frac{1}{(\langle c_1 \rangle + \langle c_2 \rangle)^2} \cdot \left[ \langle c_1 \rangle \prod_{i=1}^n \frac{\exp\left(-\frac{q(\boldsymbol{\rho}, \alpha)_i^2}{4D_{1,i}t(\boldsymbol{\rho}) + w_i^2}\right)}{\sqrt{\pi(4D_{1,i}t(\boldsymbol{\rho}) + w_i^2)}} + \langle c_2 \rangle \prod_{i=1}^n \frac{\exp\left(-\frac{q(\boldsymbol{\rho}, \alpha)_i^2}{4D_{2,i}t(\boldsymbol{\rho}) + w_i^2}\right)}{\sqrt{\pi(4D_{2,i}t(\boldsymbol{\rho}) + w_i^2)}} \right],$$

where  $D_{1,i}$ ,  $D_{2,i}$  are diffusion coefficients in direction  $i$  for the first and second component, respectively.

## 1.7 Triplet states

It is possible for a fluorescent molecule to go into a so-called triplet state from where it relaxes back to ground state after a delay much longer than it takes for the normal excitation-emission cycle to complete. This phenomenon, if ignored, could cause diffusion coefficients to be overestimated. To account for this effect, we multiply the CF function (Eq.9 or Eq.11) with a compensation factor (4, 8–10) :

$$1 + \frac{T}{1-T} \exp\left(-\frac{t}{\tau}\right), \quad (12)$$

where  $T$  is the fraction of molecules in triplet state and  $\tau$  the triplet state relaxation time.

## 1.8 Full form of correlation function

In this work the experimentally measured PSF was used instead of the approximated one (Eq.5), necessitating numerical integration for each CF evaluation:

$$G(\boldsymbol{\rho}, \alpha) = \frac{1}{\langle F_1(\mathbf{p}) + F_2(\mathbf{p}) \rangle_{\mathbf{p}}^2} \left( 1 + \frac{T}{1-T} \exp\left(-\frac{t}{\tau}\right) \right) \cdot \iint W(\mathbf{r})W(\mathbf{r}') (\langle c_1 \rangle \cdot g_{D1} + \langle c_2 \rangle \cdot g_{D2}) \, d\mathbf{r} \, d\mathbf{r}' \quad (13)$$

This is the CF form used for fitting experimental data in this work.

## 2 DETAILED METHODS

### 2.1 Confocal setup

To perform imaging for raster image correlation spectroscopy (RICS), we designed and built a confocal microscope. This allowed us to automate image acquisition under

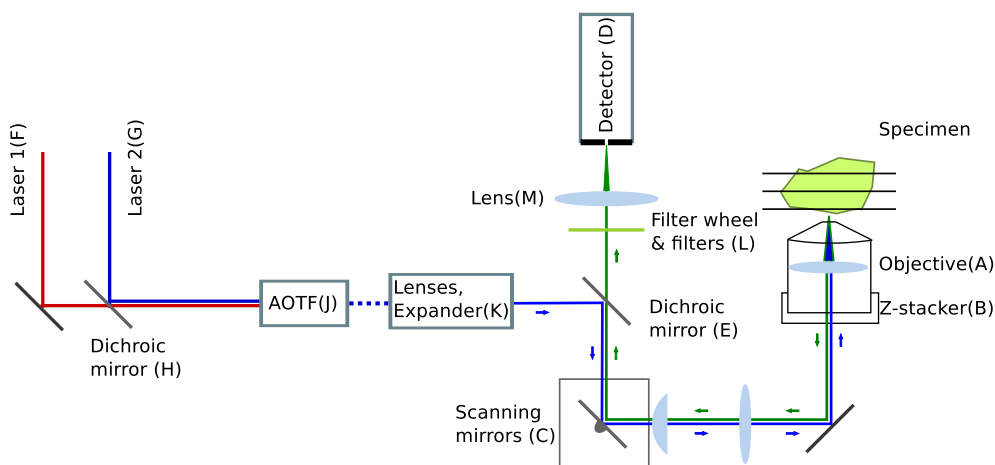


FIGURE S3: Scheme of the confocal microscope setup. See text for description of the parts.

varying laser scanning angles and frequencies.

The confocal microscope was built around Olympus IX71-FV5F-2, using the left side port with the mounted scanning lens (FV3-PLI2-2, Olympus). Images were acquired using water-immersion 60 $\times$  objective (UPLSAPO, NA 1.2, Olympus, indicated by *A* on Fig. S3) mounted on piezoelectric objective-lens positioning system (MIPOS 250 SG driven by 12V40 CLE piezo amplifier, Piezosystem Jena, Germany, *B* on Fig. S3). Excitation laser beam was guided and fluorescence signal descanned (i.e., emitted light from the sample returns along the path taken by excitation light, reflecting from the scanning mirrors (*C*) before heading to the detector (*D*) from the dichroic mirror (*E*) on the image plane of the scanning lens using galvo mirrors (6210H 3mm 6121H 2-mirror system, Cambridge Technology, MA, USA; *C* on Fig. S3).

Two lasers were used in the experiments: 633 nm 05-LHP-151 (Melles Griot, USA; *F* on Fig. S3) and 473 nm SDL-473-LN-O10T (Shanghai Dream Lasers Technology Co. Ltd, China, *G* on Fig. S3). Beams of the lasers were combined using LM01-503 dichroic (Semrock, Rochester, NY, USA; *H* on Fig. S3); all following dichroics and filters are from this company), passed through an acousto-optical tunable filter (AOTF; *J* on Fig. S3) to select the laser line and regulate power of the excitation (AOTFnC-VIS-TN, AA Sa Opto-Electronic Division, France). Laser beam was expanded and filtered by spatial filter KT310 using C220TME-A (FD 11mm) as focusing lens, P25S (25  $\mu$ m) pinhole, and LA1608-A (FD 75mm) as a collimating lens (all from Thorlabs, NJ, USA, *K* on Fig. S3). After the spatial filter, the beam was passed through iris SM1D12C (Thorlabs) set at 2.4 mm. Excitation light and fluorescence emission were separated by dichroic FF500/646-Di01-25x36 (*E* on Fig. S3). Fluorescence signal passed an emission filter (FF01-550/88-25 or FF01-725/150-25 for 473 nm or 633 nm excitation, respectively) which was selected using motorized filter wheel FW102B (Thorlabs; *L* on Fig. S3). After passing the emission filter, fluorescence signal was

focussed by AC254-500-A1-ML (FD 500 mm;  $M$  on Fig. S3 ) on photon counter SPCM-AQRH-13 (PerkinElmer, USA;  $D$  on Fig. S3). In this design, photon counter detector (nominal diameter 170  $\mu\text{m}$ ) was used as a pinhole. The optical scheme was mounted on honeycomb table top 1HT12-15-20 positioned on pneumatic vibration isolation system 1VIS95-065-08-70 (Standa, Lithuania). The scheme was covered by custom cover with internal wall separating excitation light processing before the dichroic that splits excitation and emission light. To avoid signal contamination from emitted radiation by galvo mirrors, a wall was mounted that prevented the radiation to reach the detector from mirror motors. In addition, filter wheel LED position indicator was turned off during acquisition to avoid emission signal contamination. Optical scheme was adjusted to optimize for maximal emission signal and symmetry of point spread function (PSF). Resulting PSF has been published earlier (11).

Confocal microscope was controlled using custom made software. Galvo mirrors, piezoelectric objective-lens positioning system and AOTF were driven by PCIe-6259 (National Instruments, Texas, USA) using analog (mirrors and piezomotor) and digital outputs (AOTF). Feedback from galvo mirrors and piezomotor was recorded via analog input channels of the same card. This feedback signal was used to optimize the driving signal to ensure that the specified region of interest was scanned. Photon counter pulses were counted using PCI-6602 card (National Instruments) and read out by the software with the specified pixel time (1  $\mu\text{s}$  for RICS measurements, 25  $\mu\text{s}$  or larger for imaging). Excitation light was reduced during flyback using AOTF ensuring that it fully recovered by the beginning of each imaged line. The cards and the software was running on Linux (OpenSUSE) PC with National Instruments cards interfaced using NI-DAQmx 8.0.1 driver (National Instruments).

Imaging for RICS was performed in a  $\sim 20 \times 20 \mu\text{m}$  region with line scanning frequencies 167, 289, and 500 Hz. The signal was acquired during half of the scan time with the other half used for flyback. Imaging was performed with different scan directions by changing the angle of acquisition from  $-180^\circ$  to  $+180^\circ$  with a step of  $20^\circ$ . Images were acquired in sets of 90 (scanning frequency 500 Hz), 60 (289 Hz), and 30 (167 Hz) frames. The order with images with different scanning frequencies and directions were recorded was randomized.

“Poking” of cells was performed with 1.0 mm diameter glass pipettes (World Precision Instruments, USA) manufactured into 0.5  $\mu\text{m}$  diameter tips using a pipette puller (PC-10 puller, Narishige, Japan). Cell membranes were permeated by controlling the pipette with a micromanipulator (PatchStar Micromanipulator System PS-8300C, Scientifica, England).

## 2.2 Determination of diffusion coefficients using RICS

Measurements were performed using different laser scanning frequencies and directions, similar to our earlier study (12). Through variation of scanning speed and direction, we change  $t(\varrho)$ . As a result, several components of diffusion coefficients can

be estimated and fits can be optimized against measurements obtained with different scan frequencies. In total we used 19 angles spanning the range from 0 to 360 degrees and 3 different scanning speeds. In our analysis, we assumed that the shape of rat cardiomyocyte can be approximated as a cylindrical rod. In experiments, cells were aligned along the  $y$  axis. Thus,  $D_y$  corresponded to longitudinal diffusion coefficient  $D_L$  and  $D_x = D_z$  — to the transverse one  $D_{TR}$ .

DCs, concentrations, and triplet state parameters were determined by fitting Eq.13 with the correlation function estimated from measurements. Here, correlation between pixels on the same line as well as pixels on two adjacent lines was used. Fit was performed using the least squares method by the Levenberg-Marquardt algorithm (13). Integral in Eq.13 was determined numerically to take into account the asymmetry of the PSF, as in (12). PSF measurements were conducted regularly so as to verify that it remains stable throughout the experiment series. Fits were performed with the PSF obtained for the current alignment.

Effect of fluorophore photobleaching can be compensated for by using the approach applied in (8, 14). This involves correcting the correlation curves obtained for the  $i$ -th image by multiplying it with the ratio of average intensity of the  $i$ -th image to that of the first image. We did not apply this correction, however, as we perform RICS analysis only to an subsection of the recorded images where the average image intensity did not change over time. This selectivity effectively means that a separate compensation factor is not necessary. Due to the high photostability of the dyes employed (as indicated by long stable ranges in image sequences) we considered triplet states as the main cause for loss of fluorescence that would interfere with DC estimation.

For calibration, the PSF was scaled with the scaling factor that was optimized together with other parameters when fitting the measurements recorded in water and solution. The scaling factor was found to be  $1.042 \pm 0.014$  ( $n=24$ ). Value of 1.04 was used when analysing data recorded in cardiomyocytes.

When estimating DCs with RICS in cells, images are first processed by removing the immobile fraction of the signal using moving average, as in (2, 15). For that images were blurred with a 3x3 kernel (each pixel's value was taken as the average of the pixel together with its closest neighbors) to reduce interference with DC estimation (see *Supporting results*). This is similar to the approach used in (8).

## 2.3 Solutions

The measurement solution contained (in mM) 0.5 EGTA (Sigma, 03778), 3.0  $\text{KH}_2\text{PO}_4$  (Sigma, P0662), 3.0  $\text{MgCl}_2$  (Sigma, 63068), 20 HEPES (Sigma, H3375), 110 sucrose (Sigma, S1888), 20 taurine (Sigma, 86329), 0.5 dithiothreitol (Sigma, D0632) and 60 lactobionate (Sigma, L2398), 5 glutamate (Sigma, 49449), 2 malate (Sigma, M6413). In addition, 5 mg/ml BSA (Roche, 10 775 835 001) was added, and pH was adjusted at 25°C to 7.1 with KOH.

The simplified solution with reduced content of macromolecules contained (in mM)

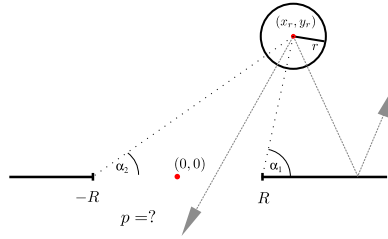


FIGURE S4: Probability  $p$  of particle of radius  $r$  located at  $x_r, y_r$  diffusing through a pore of radius  $R$  within timestep  $\tau$ .  $\alpha_1$  and  $\alpha_2$  are the angles within which it is possible for the particle to permeate the pore (shown approximately on the figure)

0.5 EGTA, 3.0  $\text{KH}_2\text{PO}_4$ , 3.0  $\text{MgCl}_2$ , 20 HEPES, 0.5 dithiothreitol and 60 lactobionate. pH was adjusted at  $25^\circ\text{C}$  to 7.1 with KOH.

### 3 MATHEMATICAL MODEL

#### 3.1 Relation of barrier permeability to barrier and molecule properties

*Motivation.* In our stochastic diffusion model we employ a permeability parameter  $p$  that describes the probability of a particle to traverse a barrier after coming into contact with it. This would, in reality, correspond to a distribution of permeable pores with a given radius on the surface of the barrier. If pore and particle dimensions are of the same order of magnitude then different particles would have different probabilities of being able to pass through the same pore, i.e., a permeability value of 1% for ATTO633-ATP would correspond to a smaller permeability for Alexa647-dextran 10K. Our goal is to determine the relative permeability values between particles of different sizes and to find a relationship between permeability and particle and pore dimensions.

*Derivation.* We take a circular object of radius  $r$  located at  $(x_r, y_r)$ . The object is diffusing with diffusion coefficient  $D_x$ . Centered at  $(0, 0)$  is a wall with an opening of radius  $R$  (see Fig. S4.)

The particle makes a random step, consisting of two independent steps in  $x$  and  $y$  directions:  $dx \sim \mathcal{N}(0, \sigma)$  and  $dy \sim \mathcal{N}(0, \sigma)$ , where  $\sigma = \sqrt{2D_x\tau}$ . Total distance travelled  $L = \sqrt{dx^2 + dy^2}$ , follows the Rayleigh distribution:

$$L \sim \text{Rayleigh}(L, \sigma) = \frac{L}{\sigma^2} \exp\left(-\frac{L^2}{2\sigma^2}\right)$$

Probability of the particle passing through the hole is:

$$\begin{aligned}
 p_\alpha &= \frac{\int_{\alpha_1}^{\alpha_2} \int_{\frac{y_r}{\sin \alpha}}^{\infty} \text{Rayleigh}(L, \sigma) \, dL \, d\alpha}{\underbrace{\int_0^{\alpha_2} \int_0^{\infty} \text{Rayleigh}(L, \sigma) \, dL \, d\alpha}_{=1}} \\
 &= \frac{\int_{\alpha_1}^{\alpha_2} \exp\left(-\frac{y_r^2}{2\sigma^2 \sin^2 \alpha}\right) \, d\alpha}{2\pi}, \tag{14}
 \end{aligned}$$

where  $\alpha_1$  and  $\alpha_2$  are the minimum and maximum angles at which the object can still pass through the hole and  $\frac{y_r}{\sin \alpha}$  is the minimal distance to travel to pass through at angle  $\alpha$ . From Fig. S4 it is visible that  $\alpha_1$  and  $\alpha_2$  change as  $x_r, y_r, r$  and  $R$  change. It is possible to calculate  $\alpha$  values iteratively with increasing accuracy or by numerically solving the exact equation relating all the parameters. The integral in Eq.14 can not be represented in elementary functions and we must calculate the probabilities we seek numerically. Example probabilities for ATTO633-ATP and Alexa647-dextran 10K are shown on Fig. S5. As can be seen, the probabilities for ATTO633-ATP compared to Alexa647-dextran 10K to go through the pore are greater at all locations.

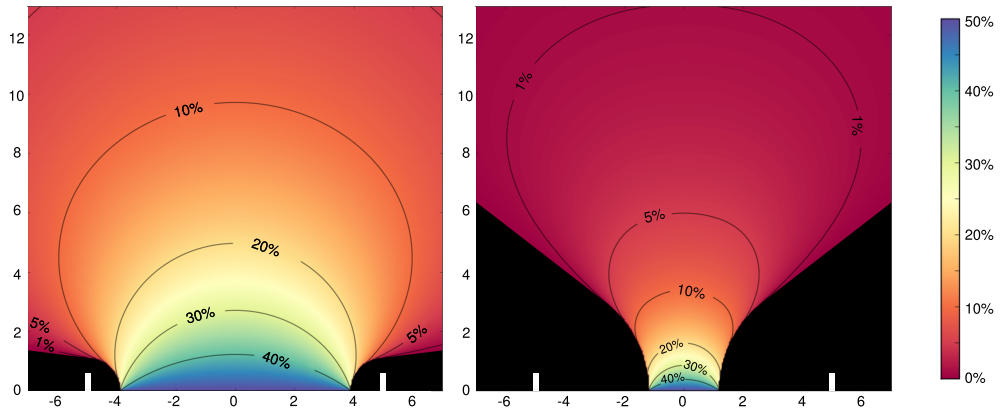


FIGURE S5: Probabilities for ATTO633-ATP (left) and Alexa647-dextran 10K (right) of going through a 10nm diameter pore (shown with white lines). Color at a given location indicates probability of the particle going through the pore in one random step. The area in black shows the region from where it is impossible for the particle to go through the pore.

The probability for a particle to get out from the inside of a square  $D$  with side length

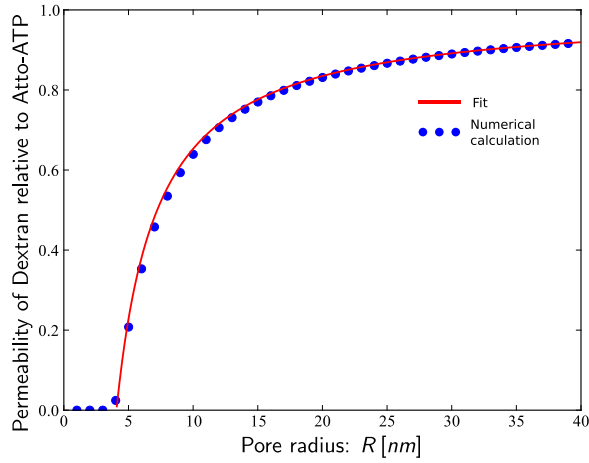


FIGURE S6: Ratio of probability of Alexa647-dextran 10K to ATTO633-ATP going through a pore of radius  $R$ . As pore radius increases, the ratio approaches 1, i.e., both particles are almost as like to permeate the pore. Dots indicate numerical calculations based on Eq.17, solid line is an approximate fit.

$d$  covered with  $n$  pores of radius  $R$  on each side is:

$$P_a = \frac{4n \cdot \overbrace{\iint p_a dx_r dy_r}^{\doteq Q}}{\iint_D dx_r dy_r} = \frac{4n \cdot Q}{d^2}, \quad (15)$$

where  $Q$  is the value of the numerically calculated surface integral of  $p_a$ .

Probability  $P_a$  from Eq.15 gives the combined probability of a particle reaching the wall from anywhere inside the square and then passing through a pore, i.e.,  $P_a = p \cdot P_b$ , where  $P_b$  is the probability of the particle reaching the wall, and  $p$  is the probability of permeating the wall (the barrier permeability parameter used in our stochastic diffusion model). In order to calculate  $P_b$  we first need to find the probability of reaching the wall from a given position  $(x_r, y_r)$ . This is given by:

$$p_b = \frac{\int_0^\pi \exp\left(-\frac{y_r^2}{2\sigma^2 \sin^2 \alpha}\right) d\alpha}{\int_0^\pi \int_0^\infty \text{Rayleigh}(L, \sigma) dL d\alpha} = \text{erfc} \frac{y_r}{\sigma\sqrt{2}},$$

where  $\text{erfc}$  is the complementary error function. For  $P_b$  we get:

$$P_b = \frac{4 \cdot \iint p_b \, dx_r \, dy_r}{\iint dx_r \, dy_r} = \frac{4d\sigma\sqrt{\frac{2}{\pi}}}{d^2}. \quad (16)$$

Combining Eqs. 15 and 16 we get for permeability  $p$ :

$$p = \frac{P_a}{P_b} = \frac{nQ}{d\sigma\sqrt{\frac{2}{\pi}}}.$$

When we compare two molecules with different radii and diffusion coefficients (i.e.,  $r_1 \neq r_2$  and  $\sigma_1 \neq \sigma_2$ , whereby  $Q_1 \neq Q_2$ ), then the ratio of their respective permeabilities is:

$$\frac{p_1}{p_2} = \frac{Q_1 \cdot \sigma_2}{Q_2 \cdot \sigma_1}. \quad (17)$$

The dependence of this ratio on pore radius  $R$  for ATTO633-ATP and Alexa647-dextran 10K is shown on Fig. S6. The fit depicted on the figure is:  $\frac{p_1}{p_2} \approx \frac{R-r_1}{R-r_2}$ . The fit can match the theoretical values closely and is trivial to calculate compared to finding exact theoretical values which require time consuming numerical calculations. The formula itself can be justified by the following:  $n$  pores of radius  $R$  on a otherwise impermeable line of length  $d$  gives  $\frac{n \cdot R}{d}$  as the ratio of permeable to impermeable sections of the line i.e., permeability. For a particle with radius  $r$  the effective radius of a pore would be  $R - r$ , giving  $\frac{n \cdot (R-r)}{d}$  as permeability. Introducing pore density  $\eta = n/d$  we can write:  $p = \eta(R - r)$ . It is easy to see that using this result for two different particles and taking the ratio would yield the formula used for the fit in Fig. S6.

In two dimensions, total permeability for  $n$  circular pores of radius  $R$  on a surface with area  $A$  would be  $\frac{n \cdot \pi R^2}{A}$ . Again, for a particle this translates to effective permeability of  $p = \frac{n \cdot \pi (R-r)^2}{A}$ . Defining  $\eta$  as the number of pores per unit area, we get:

$$p = \eta \cdot \pi (R - r)^2,$$

which is the relationship between permeability, pore radius and particle radius used in our calculations.

### 3.2 Theoretical correlation function for 1D RICS

In order to analyze images obtained from the simplified 1D stochastic diffusion model, an analytic expression for the correlation function is used in fitting. This is obtained for the 1D case from Eq.3. The correlation function showing correlation between

pixels separated from each other by image shift  $\Delta\xi$  and time  $t$ , can be calculated from:

$$G(\Delta\xi) = \frac{\int_{-\infty}^{\infty} \int_{-\infty}^{\infty} W(x_1)W(x_2)G_D(x_1, x_2, \Delta\xi) dx_1 dx_2}{\left( \langle c \rangle \int_{-\infty}^{\infty} W(x) dx \right)^2} .$$

Here,  $G_D$  is the correlation due to diffusion (from Eq.4 with  $n = 1$ )

$$G_D(x_1, x_2, \Delta\xi) = \frac{c}{\sqrt{4\pi D_x t}} \exp\left(-\frac{(x_2 + \Delta\xi \cdot s_\xi - x_1)^2}{4iD_x \cdot t}\right) ,$$

with  $\langle c \rangle$  representing concentration.  $D_x$  the diffusion coefficient,  $s_\xi$  the pixel size in  $\xi$  direction and  $t = t(\Delta\xi)$  is the delay time between acquisition of two pixels separated by  $\Delta\xi$ .

$W$  is the 1D PSF (from Eq.5 with  $n = 1$ ):

$$W(x) = \exp\left(-\frac{2x^2}{w_x^2}\right) ,$$

where  $w_x$  determines the width of the PSF.

After taking all the integrals and similar to Eq.6 with  $n = 1$ :

$$G(\Delta\xi) = \frac{\exp\left(-\frac{(s_\xi \cdot \Delta\xi)^2}{4D_x t + w_x^2}\right)}{\langle c \rangle \sqrt{\pi} \sqrt{4D_x t + w_x^2}} .$$

This formula was used to fit numerical experiments performed with the 1D stochastic model.

## 4 SUPPORTING RESULTS

### 4.1 RICS extensions

To demonstrate the extended RICS protocol, we determined diffusion coefficients (DCs) of fluorescent dyes in water. Representative correlation functions (CF) calculated from measurements of ATTO633-ATP and Alexa647-dextran 10K are shown in Fig. S7. By varying the frequency of laser scanning while acquiring images in confocal microscope, we varied the relationship between spatial and temporal components of fluctuations of the signal (Fig. S7A and B). The plots in Fig. S7A and B contain the same data and theoretical fits. However, since we alter the scanning frequency it is easier to visually discern the differences in correlation if it is shown as a function of time (Fig. S7B) rather than space (Fig. S7A), which is the classical representation

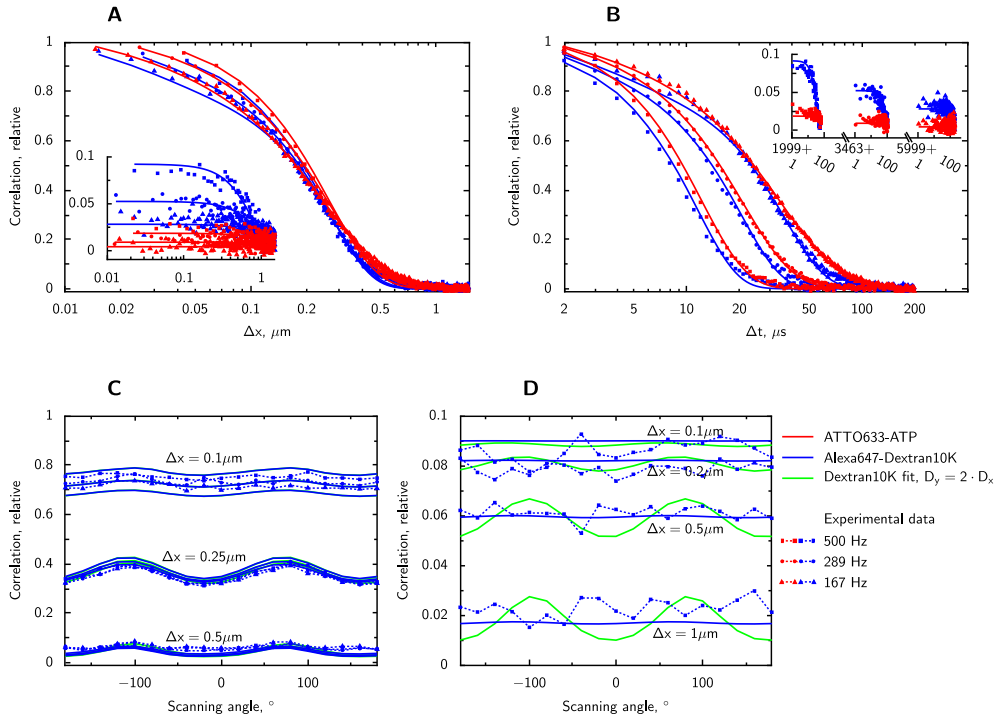


FIGURE S7: Diffusion of ATTO633-ATP (red) and Alexa647-dextran 10K (blue) in water analyzed by RICS. Experimental data (points) acquired at different laser scanning frequencies and directions are fitted with theoretical correlation curves given in Eq.13 (lines). By using dyes with different diffusion coefficients, we demonstrate the influence of diffusion coefficient on spatial (A) and temporal (B) components of correlation functions. Data and theoretical fits shown on A and B are identical. A is the classical way of presenting correlation functions in RICS analysis. As we use multiple scanning speeds, plotting correlation as a function of time (as in B) illustrates the differences caused by changes in scanning speed. Converting between A and B plots can be done by employing Eq.8. On A and B, imaging was performed with the laser scanning along a line parallel to axis  $x$  at different frequencies (frequencies noted in legend on the right bottom). Correlation along the same line is shown in the main graphs (A,B) while correlation of the signal between pixels in adjacent lines is shown in the insets. Due to the laser backtracking and variation in scan frequencies, temporal component has gaps visible in the inset of B. Due to asymmetry of PSF, laser scanning in different directions leads to modification of correlation function between pixels in the same line (C) and in the adjacent lines (D). This is demonstrated by showing correlation function estimated from the experiment (dots connected by dashed lines) and results of the fit (solid blue line) for Alexa647-dextran 10K. Correlation between pixels in the same line is not as sensitive to anisotropy of diffusion as correlation between neighbouring lines, resulting in an overlap between fits having a two time difference in diffusion coefficients in the  $y$  direction, as seen on C. Distinction between isotropic and anisotropic fits is mainly visible on correlation between pixels in adjacent lines (D).

for RICS. In both cases Eq.13 was used for the theoretical fit. While for Alexa647-

dextran 10K a significant correlation of fluorescence fluctuations can be observed between pixels in two consecutive scan lines (Fig. S7A and B insets), the correlation is rather small for ATTO633-ATP. This is due to the larger DC of ATTO633-ATP leading to a smaller probability of a molecule staying in the same neighborhood while the laser is scanning two consecutive lines. For Alexa647-dextran 10K, correlation of fluctuations between pixels depends on laser scanning frequency, as demonstrated in Fig. S7A and B insets. By taking into account asymmetry of the point spread function (PSF), we can fit CFs obtained from measurements at different laser scanning frequencies and directions with a theoretical CF from Eq.13 . The resulting fits are represented in Fig. S7 by solid lines. From analysis of the CFs for Alexa647-dextran 10K in water, dependence of CF on scanning angle in Fig. S7C and D demonstrates that asymmetry of PSF is mainly influencing correlation between pixels in the same line of an image. When fitting the CFs with a model that assumes a two time difference in DCs in  $x$  and  $y$  directions (green solid line in Fig. S7C and D), we observed that the model solution was different from isotropic case mainly in the signal correlation between pixels in adjacent lines (Fig. S7D). Correlation of the signal in the same line was not that much influenced by anisotropy (green and blue lines in Fig. S7C are very close to each other). Note that this observation can depend on the DCs.

Obtained diffusion coefficients, triplet time constants ( $\tau$ ) and triplet state contribution ( $T$ ) to correlation functions for ATTO655-COOH, ATTO633-ATP, and Alexa647-dextran 10K are shown in Table 1 (main text). To test our method, we analyzed diffusion of ATTO655-COOH in water at 26°C. According to our measurements, the DC for ATTO655-COOH is  $454 \pm 3 \mu\text{m}^2/\text{s}$ . This is similar to the DC in water determined for the same dye using 2-focal fluorescence correlation spectroscopy measurements (16),  $426 \pm 8 \mu\text{m}^2/\text{s}$  at 25°C. Taking into account the difference in temperatures, this would correspond to  $\sim 437 \mu\text{m}^2/\text{s}$  in our conditions. DCs for ATTO633-ATP and Alexa647-dextran 10K which we used to study diffusion in cardiomyocytes (CM) were smaller in water as well as in the measurement solution (Table 1). Comparing DCs in water and solution, we can see that exposure to solution reduces the DC of Alexa647-dextran 10K and ATTO655-COOH to 80-85% of the value in pure water. For ATTO633-ATP, the reduction is considerably larger: DC in solution was only 60% of the value in water. We checked whether this reduction of DC could be attributed to the binding of a fraction of ATTO633-ATP to proteins in measurement solution. However, RICS analysis was not able to resolve two components (slow and fast) of ATTO633-ATP (both components had the same DC when the slow component's DC was not limited). However, when exposed to a simplified solution with a reduced amount of macromolecules (see *Detailed Methods* of Supporting Material for solution composition), we observed a reduction of the DC of ATTO633-ATP to  $265 \pm 10 \mu\text{m}^2/\text{s}$  ( $n = 4$ ), i.e., to  $\sim 80\%$  of the value in water. In contrast, the DCs of Alexa647-dextran 10K and ATTO655-COOH in this simplified solution remained similar to their DCs in water :  $60 \pm 1$  ( $n = 4$ )  $\mu\text{m}^2/\text{s}$  and  $451 \pm 10 \mu\text{m}^2/\text{s}$  ( $n = 5$ ), respectively. This suggests that diffusion of ATTO633-ATP in the measurement solution is influenced

in part by interaction of ATTO633-ATP salt with ions in the solution, leading to an increase in the apparent hydrodynamic radius of ATTO633-ATP. To avoid any bias induced by such interaction, we compared the DCs of dyes in the cell to the DCs in the measurement solution, not to the coefficients in water.

We fitted the CFs estimated from the measurements in water and solution using the anisotropic model. According to our fits, DCs in longitudinal  $y$  (L) direction was systematically overestimated (Table 1) leading to up to 22% difference in DCs (the largest anisotropy was estimated for ATTO633-ATP in solution). Thus, small differences in DCs due to anisotropy cannot be resolved with our method. We found that the predicted anisotropy can depend on the model used. In estimating DCs, we used a model where the  $x$  and  $z$  direction were taken to represent the transverse  $TR$  direction. When taking  $y$  and  $z$  as the transverse direction instead, the predicted anisotropy was much smaller. The exception was a relatively high anisotropy predicted for Alexa647-dextran 10K in water (25%). We think that such dependence on the model is induced by inaccuracies in the PSF.

When estimating DCs with RICS in cells, images are first processed by removing the immobile fraction of the signal using a moving average. We applied the same pre-processing to images recorded in water and solution. As a result, we found that such pre-processing affects RICS analysis. Influence on DC was found to be relatively small with DC estimated after removal of the average being  $0.95\times$  to  $1.13\times$  larger than DC estimated from the original images. However, triplet state characteristics were influenced more profoundly with triplet state time constant increasing by  $1.17\times$  to  $1.52\times$  and triplet state contribution increasing by  $1.05\times$  to  $1.36\times$ . To reduce the influence of pre-processing on RICS analysis, we took advantage of sub-PSF pixel sizes and performed averaging by using images blurred with a  $3\times 3$  kernel (each pixel's value was taken as the average of the pixel together with its closest neighbors). Using such a kernel reduced the influence of average signal subtraction on DC ( $1.02\times$  to  $1.05\times$  larger than before pre-processing), triplet state time constant ( $1.08\times$  to  $1.16\times$ ), and triplet state contribution ( $0.92\times$  to  $1.04\times$ ). On the basis of these observations, we used blurring by  $3\times 3$  kernel in analysis of diffusion in cardiomyocytes.

## 4.2 Diffusion obstacle parameter sensitivity

Parameters presented in Table 2 of the main text were obtained by finding intersections between curves of experimental and computational results. As visible from Figures 2C,2D and 2E in the main text, a range of barrier-to-barrier distance, pore radius and pore density values satisfy the constraints of the model and computational results. The experimentally obtained DC values have a error associated with them. In order to estimate the uncertainties caused by measurement errors in the parameters we found, Monte Carlo analysis was applied. Similar to the procedure depicted on Figure 2B and 2C, random DC for ATTO633-ATP and Alexa647-dextran 10K were chosen from a normal distribution with the mean and standard deviation equal to the values from

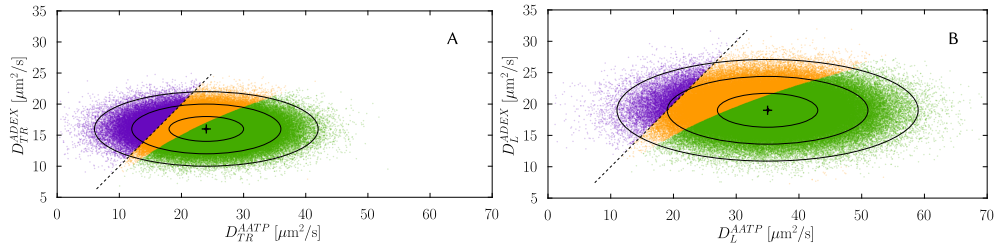


FIGURE S8: Distributions of random generated pairs of ATTO633-ATP and Alexa647-dextran 10K diffusion coefficients in transverse(A) and longitudinal directions (300000 values each). Pairs were randomly generated from normal distributions having the mean and standard deviation obtained from experiment (shown in Table 1 of the main text. Experimental mean values are shown with a cross. Ellipses indicate distances 1,2 and 3 standard deviations from the mean. Dotted line show DC values of ATTO633-ATP and Alexa647-dextran 10K are equal. As explained in the text, values left of this line are discarded and not included in analysis. The middle region(shown in yellow) contains DC value pairs where density of pores in barrier would be less then 1 per barrier. For the DC values in the green region intersections are found as in the main text and collected for statistics.

experiments presented in Table 1 (i.e.,  $\mathcal{N}(24, 6)$ ,  $\mathcal{N}(16, 2)$  for ATTO633-ATP and Alexa647-dextran 10K in the transverse direction and  $\mathcal{N}(35, 8)$ ,  $\mathcal{N}(19, 3)$  in the longitudinal direction). For each randomly generated ATTO633-ATP Alexa647-dextran 10K DC value pair, intersections were found and from those a range of suitable parameter values determined. Random sampling was performed 300000 times for both transverse and longitudinal directions. The resulting distribution of random DC value pairs are shown on Fig. S8A and B for the transverse and longitudinal directions, respectively. Of possible combinations two types were discarded. First, cases where DC of Alexa647-dextran 10K was larger than ATTO633-ATP (left of the dashed lines and on Fig. S8) and, secondly, cases where the pore density value was so low that less than one would be present on a single barrier element (the middle, light region on Fig. S8). For all other pairs model parameter maximum and minimum values were obtained and collected. Histograms for obtained maximum and minimum parameter values are presented in Figs. S9 and S10. Histograms for maximum estimate of DC reduction values are not shown as they were always 100% of the DC in solution. The results presented in Table 2 in the main text are the mean and standard deviations of these distributions.

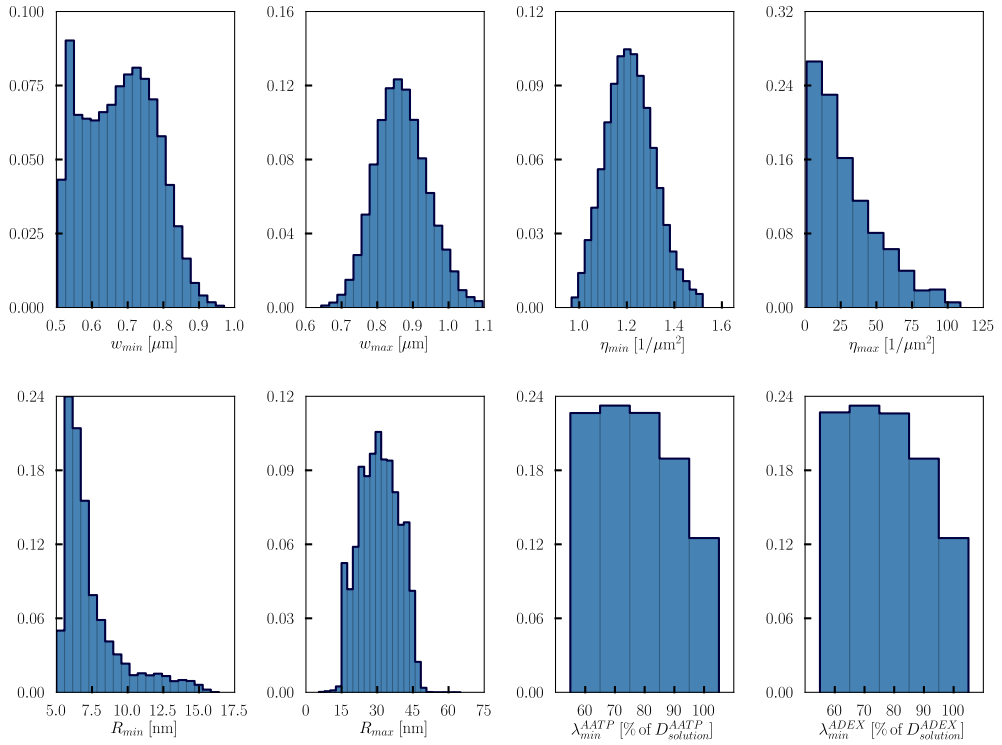


FIGURE S9: Histograms showing distributions of minimum and maximum model parameter values obtained from Monte Carlo simulations in the transverse direction.

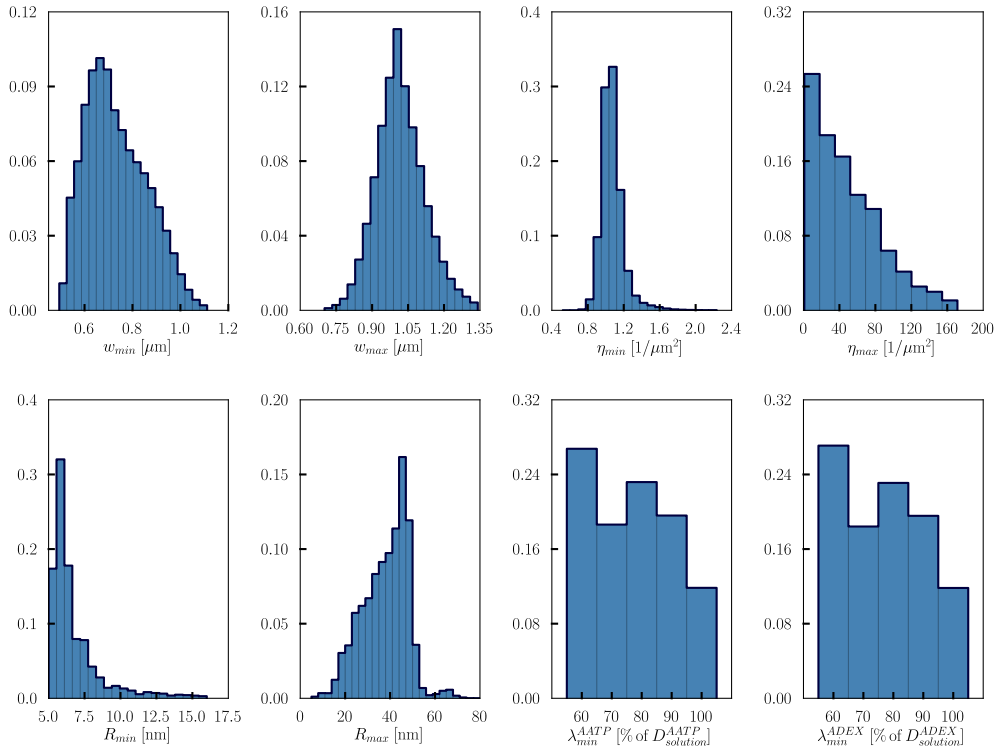


FIGURE S10: Histograms showing distributions of minimum and maximum model parameter values obtained from Monte Carlo simulations in the longitudinal direction.

**SUPPORTING REFERENCES**

1. Brown, C. M., R. B. Dalal, B. Hebert, M. A. Digman, A. R. Horwitz, and E. Gratton, 2008. Raster image correlation spectroscopy (RICS) for measuring fast protein dynamics and concentrations with a commercial laser scanning confocal microscope. *J Microsc* 229:78–91.
2. Digman, M. A., C. M. Brown, P. Sengupta, P. W. Wiseman, A. R. Horwitz, and E. Gratton, 2005. Measuring fast dynamics in solutions and cells with a laser scanning microscope. *Biophys J* 89:1317–1327.
3. Digman, M. A., and E. Gratton, 2011. Lessons in Fluctuation Correlation Spectroscopy. *Annu Rev Phys Chem* 62:645–668.
4. Haustein, E., and P. Schuille, 2007. Fluorescence correlation spectroscopy: novel variations of an established technique. *Annu. Rev. Biophys. Biomol. Struct.* 36:151–169.
5. Lakowicz, J., 2006. Principles of fluorescence spectroscopy. Springer.
6. Thompson, N., 2002. Fluorescence Correlation Spectroscopy. In J. Lakowicz, C. D. Geddes, and J. R. Lakowicz, editors, Topics in Fluorescence Spectroscopy, Springer US, volume 1 of *Topics in Fluorescence Spectroscopy*, 337–378.
7. Vendelin, M., and R. Birkedal, 2008. Anisotropic diffusion of fluorescently labeled ATP in rat cardiomyocytes determined by raster image correlation spectroscopy. *Am. J. Physiol. Cell. Physiol.* 295:C1302–1315.
8. Gröner, N., J. Capoulade, C. Cremer, and M. Wachsmuth, 2010. Measuring and imaging diffusion with multiple scan speed image correlation spectroscopy. *Opt. Express* 18:21225.
9. Krichevsky, O., and G. Bonnet, 2002. Fluorescence correlation spectroscopy: the technique and its applications. *Reports on Progress in Physics* 65:251.
10. Widengren, J., U. Mets, and R. Rigler, 1995. Fluorescence correlation spectroscopy of triplet states in solution: a theoretical and experimental study. *J Phys Chem* 99:13368–13379.
11. Laasmaa, M., M. Vendelin, and P. Peterson, 2011. Application of regularized Richardson-Lucy algorithm for deconvolution of confocal microscopy images. *J Microsc* 243:124–140.
12. Vendelin, M., and R. Birkedal, 2008. Anisotropic diffusion of fluorescently labeled ATP in rat cardiomyocytes determined by raster image correlation spectroscopy. *Am J Physiol Cell Physiol* 295:C1302–C1315.
13. Moré, J. J., D. C. Sorensen, K. E. Hillstrom, and B. S. Garbow, 1984. The MINPACK Project. In W. J. Cowell, editor, Sources and Development of Mathematical Software, Prentice-Hall.
14. Brown, C. M., R. B. Dalal, B. Hebert, M. A. Digman, A. R. Horwitz, and E. Gratton, 2008. Raster image correlation spectroscopy (RICS) for measuring fast protein dynamics and concentrations with a commercial laser scanning confocal microscope. *J. Microsc.* 229:78–91.
15. Rossow, M. J., J. M. Sasaki, M. A. Digman, and E. Gratton, 2010. Raster image correlation spectroscopy in live cells. *Nat Protoc* 5:1761–1774.
16. Dertinger, T., V. Pacheco, I. von der Hocht, R. Hartmann, I. Gregor, and J. Enderlein, 2007. Two-focus fluorescence correlation spectroscopy: a new tool for accurate and absolute diffusion measurements. *Chemphyschem* 8:433–443.

DISSERTATIONS DEFENDED  
AT TALLINN UNIVERSITY OF TECHNOLOGY  
ON NATURAL AND EXACT SCIENCES

---

1. **Olav Kongas.** *Nonlinear Dynamics in Modeling Cardiac Arrhythmias.* 1998.
2. **Kalju Vanatalu.** *Optimization of Processes of Microbial Biosynthesis of Isotopically Labeled Biomolecules and Their Complexes.* 1999.
3. **Ahto Buldas.** *An Algebraic Approach to the Structure of Graphs.* 1999.
4. **Monika Drews.** *A Metabolic Study of Insect Cells in Batch and Continuous Culture: Application of Chemostat and Turbidostat to the Production of Recombinant Proteins.* 1999.
5. **Eola Valdre.** *Endothelial-Specific Regulation of Vessel Formation: Role of Receptor Tyrosine Kinases.* 2000.
6. **Kalju Lott.** *Doping and Defect Thermodynamic Equilibrium in ZnS.* 2000.
7. **Reet Koljak.** *Novel Fatty Acid Dioxygenases from the Corals *Plexaura homomalla* and *Gersemia fruticosa*.* 2001.
8. **Anne Paju.** *Asymmetric oxidation of Prochiral and Racemic Ketones by Using Sharpless Catalyst.* 2001.
9. **Marko Vendelin.** *Cardiac Mechanoenergetics in silico.* 2001.
10. **Pearu Peterson.** *Multi-Soliton Interactions and the Inverse Problem of Wave Crest.* 2001.
11. **Anne Menert.** *Microcalorimetry of Anaerobic Digestion.* 2001.
12. **Toomas Tiivel.** *The Role of the Mitochondrial Outer Membrane in in vivo Regulation of Respiration in Normal Heart and Skeletal Muscle Cell.* 2002.
13. **Olle Hints.** *Ordovician Scelocodonts of Estonia and Neighbouring Areas: Taxonomy, Distribution, Palaeoecology, and Application.* 2002.
14. **Jaak Nõlvak.** *Chitinozoan Biostratigraphy in the Ordovician of Baltoscandia.* 2002.
15. **Liivi Kluge.** *On Algebraic Structure of Pre-Operad.* 2002.
16. **Jaanus Lass.** *Biosignal Interpretation: Study of Cardiac Arrhythmias and Electromagnetic Field Effects on Human Nervous System.* 2002.
17. **Janek Peterson.** *Synthesis, Structural Characterization and Modification of PAMAM Dendrimers.* 2002.
18. **Merike Vaher.** *Room Temperature Ionic Liquids as Background Electrolyte Additives in Capillary Electrophoresis.* 2002.
19. **Valdek Mikli.** *Electron Microscopy and Image Analysis Study of Powdered Hardmetal Materials and Optoelectronic Thin Films.* 2003.
20. **Mart Viljus.** *The Microstructure and Properties of Fine-Grained Cermets.* 2003.
21. **Signe Kask.** *Identification and Characterization of Dairy-Related *Lactobacillus*.* 2003
22. **Tiiu-Mai Laht.** *Influence of Microstructure of the Curd on Enzymatic and Microbiological Processes in Swiss-Type Cheese.* 2003.
23. **Anne Kuuskalu.** *2–5A Synthetase in the Marine Sponge *Geodia cydonium*.* 2003.
24. **Sergei Bereznev.** *Solar Cells Based on Polycrystalline Copper-Indium Chalcogenides and Conductive Polymers.* 2003.
25. **Kadri Kriis.** *Asymmetric Synthesis of C2-Symmetric Bimorpholines and Their Application as Chiral Ligands in the Transfer Hydrogenation of Aromatic Ketones.* 2004.
26. **Jekaterina Reut.** *Polypyrrole Coatings on Conducting and Insulating Substrates.* 2004.
27. **Sven Nõmm.** *Realization and Identification of Discrete-Time Nonlinear Systems.* 2004.
28. **Olga Kijatkina.** *Deposition of Copper Indium Disulphide Films by Chemical Spray Pyrolysis.* 2004.
29. **Gert Tamberg.** *On Sampling Operators Defined by Rogosinski, Hann and Blackman Windows.* 2004.
30. **Monika Übner.** *Interaction of Humic Substances with Metal Cations.* 2004.
31. **Kaarel Adamberg.** *Growth Characteristics of Non-Starter Lactic Acid Bacteria from Cheese.* 2004.
32. **Imre Vallikivi.** *Lipase-Catalysed Reactions of Prostaglandins.* 2004.
33. **Merike Peld.** *Substituted Apatites as Sorbents for Heavy Metals.* 2005.
34. **Vitali Syritski.** *Study of Synthesis and Redox Switching of Polypyrrole and Poly(3,4-ethylenedioxythiophene) by Using in-situ Techniques.* 2004.
35. **Lee Põllumaa.** *Evaluation of Ecotoxicological Effects Related to Oil Shale Industry.* 2004.
36. **Riina Aav.** *Synthesis of 9,11-Secosterols Intermediates.* 2005.
37. **Andres Braunbrück.** *Wave Interaction in Weakly Inhomogeneous Materials.* 2005.

38. **Robert Kitt.** *Generalised Scale-Invariance in Financial Time Series.* 2005.
39. **Juss Pavelson.** *Mesoscale Physical Processes and the Related Impact on the Summer Nutrient Fields and Phytoplankton Blooms in the Western Gulf of Finland.* 2005.
40. **Olari Ilison.** *Solitons and Solitary Waves in Media with Higher Order Dispersive and Nonlinear Effects.* 2005.
41. **Maksim Säkki.** *Intermittency and Long-Range Structurization of Heart Rate.* 2005.
42. **Enli Kiipli.** *Modelling Seawater Chemistry of the East Baltic Basin in the Late Ordovician–Early Silurian.* 2005.
43. **Igor Golovtsov.** *Modification of Conductive Properties and Processability of Polyparaphenylene, Polypyrrole and polyaniline.* 2005.
44. **Katrin Laos.** *Interaction Between Furcellaran and the Globular Proteins (Bovine Serum Albumin  $\beta$ -Lactoglobulin).* 2005.
45. **Arvo Mere.** *Structural and Electrical Properties of Spray Deposited Copper Indium Disulphide Films for Solar Cells.* 2006.
46. **Sille Ehala.** *Development and Application of Various On- and Off-Line Analytical Methods for the Analysis of Bioactive Compounds.* 2006.
47. **Maria Kulp.** *Capillary Electrophoretic Monitoring of Biochemical Reaction Kinetics.* 2006.
48. **Anu Aaspõllu.** *Proteinases from Vipera lebetina Snake Venom Affecting Hemostasis.* 2006.
49. **Lyudmila Chekulayeva.** *Photosensitized Inactivation of Tumor Cells by Porphyrins and Chlorins.* 2006.
50. **Merle Uudsemaa.** *Quantum-Chemical Modeling of Solvated First Row Transition Metal Ions.* 2006.
51. **Tagli Pitsi.** *Nutrition Situation of Pre-School Children in Estonia from 1995 to 2004.* 2006.
52. **Angela Ivask.** *Luminescent Recombinant Sensor Bacteria for the Analysis of Bioavailable Heavy Metals.* 2006.
53. **Tiina Lõugas.** *Study on Physico-Chemical Properties and Some Bioactive Compounds of Sea Buckthorn (*Hippophae rhamnoides L.*).* 2006.
54. **Kaja Kasemets.** *Effect of Changing Environmental Conditions on the Fermentative Growth of *Saccharomyces cerevisiae* S288C: Auxo-accelerostat Study.* 2006.
55. **Ildar Nisamedtinov.** *Application of  $^{13}\text{C}$  and Fluorescence Labeling in Metabolic Studies of *Saccharomyces* spp.* 2006.
56. **Alar Leibak.** *On Additive Generalisation of Voronoi's Theory of Perfect Forms over Algebraic Number Fields.* 2006.
57. **Andri Jagomägi.** *Photoluminescence of Chalcopyrite Tellurides.* 2006.
58. **Tõnu Martma.** *Application of Carbon Isotopes to the Study of the Ordovician and Silurian of the Baltic.* 2006.
59. **Marit Kauk.** *Chemical Composition of CuInSe<sub>2</sub> Monograin Powders for Solar Cell Application.* 2006.
60. **Julia Kois.** *Electrochemical Deposition of CuInSe<sub>2</sub> Thin Films for Photovoltaic Applications.* 2006.
61. **Ilona Oja Aşik.** *Sol-Gel Deposition of Titanium Dioxide Films.* 2007.
62. **Tiia Anmann.** *Integrated and Organized Cellular Bioenergetic Systems in Heart and Brain.* 2007.
63. **Katrin Trummal.** *Purification, Characterization and Specificity Studies of Metalloproteinases from Vipera lebetina Snake Venom.* 2007.
64. **Gennadi Lessin.** *Biochemical Definition of Coastal Zone Using Numerical Modeling and Measurement Data.* 2007.
65. **Enno Pais.** *Inverse problems to determine non-homogeneous degenerate memory kernels in heat flow.* 2007.
66. **Maria Borissova.** *Capillary Electrophoresis on Alkylimidazolium Salts.* 2007.
67. **Karin Valmsen.** *Prostaglandin Synthesis in the Coral Plexaura homomalla: Control of Prostaglandin Stereochemistry at Carbon 15 by Cyclooxygenases.* 2007.
68. **Kristjan Piirimäe.** *Long-Term Changes of Nutrient Fluxes in the Drainage Basin of the Gulf of Finland – Application of the PolFlow Model.* 2007.
69. **Tatjana Dedova.** *Chemical Spray Pyrolysis Deposition of Zinc Sulfide Thin Films and Zinc Oxide Nanostructured Layers.* 2007.
70. **Katrin Tomson.** *Production of Labelled Recombinant Proteins in Fed-Batch Systems in Escherichia coli.* 2007.
71. **Cecilia Sarmiento.** *Suppressors of RNA Silencing in Plants.* 2008.
72. **Vilja Mardla.** *Inhibition of Platelet Aggregation with Combination of Antiplatelet Agents.* 2008.
73. **Maie Bachmann.** *Effect of Modulated Microwave Radiation on Human Resting Electroencephalographic Signal.* 2008.
74. **Dan Hüvonen.** *Terahertz Spectroscopy of Low-Dimensional Spin Systems.* 2008.
75. **Ly Villo.** *Stereoselective Chemoenzymatic Synthesis of Deoxy Sugar Esters Involving Candida antarctica Lipase B.* 2008.

76. **Johan Anton.** *Technology of Integrated Photoelasticity for Residual Stress Measurement in Glass Articles of Axisymmetric Shape.* 2008.
77. **Olga Volobujeva.** *SEM Study of Selenization of Different Thin Metallic Films.* 2008.
78. **Artur Jõgi.** *Synthesis of 4'-Substituted 2,3'-dideoxynucleoside Analogues.* 2008.
79. **Mario Kadastik.** *Doubly Charged Higgs Boson Decays and Implications on Neutrino Physics.* 2008.
80. **Fernando Pérez-Caballero.** *Carbon Aerogels from 5-Methylresorcinol-Formaldehyde Gels.* 2008.
81. **Sirje Vaask.** *The Comparability, Reproducibility and Validity of Estonian Food Consumption Surveys.* 2008.
82. **Anna Menaker.** *Electrosynthesized Conducting Polymers, Polypyrrole and Poly(3,4-ethylenedioxythiophene), for Molecular Imprinting.* 2009.
83. **Lauri Ilison.** *Solitons and Solitary Waves in Hierarchical Korteweg-de Vries Type Systems.* 2009.
84. **Kaia Ernits.** *Study of In<sub>2</sub>S<sub>3</sub> and ZnS Thin Films Deposited by Ultrasonic Spray Pyrolysis and Chemical Deposition.* 2009.
85. **Veljo Sinivee.** *Portable Spectrometer for Ionizing Radiation "Gammamapper".* 2009.
86. **Jüri Virkepu.** *On Lagrange Formalism for Lie Theory and Operadic Harmonic Oscillator in Low Dimensions.* 2009.
87. **Marko Piirsoo.** *Deciphering Molecular Basis of Schwann Cell Development.* 2009.
88. **Kati Helmja.** *Determination of Phenolic Compounds and Their Antioxidative Capability in Plant Extracts.* 2010.
89. **Merike Sõmera.** *Sobemoviruses: Genomic Organization, Potential for Recombination and Necessity of P1 in Systemic Infection.* 2010.
90. **Kristjan Laes.** *Preparation and Impedance Spectroscopy of Hybrid Structures Based on CuIn<sub>3</sub>Se<sub>5</sub> Photoabsorber.* 2010.
91. **Kristin Lippur.** *Asymmetric Synthesis of 2,2'-Bimorpholine and its 5,5'-Substituted Derivatives.* 2010.
92. **Merike Luman.** *Dialysis Dose and Nutrition Assessment by an Optical Method.* 2010.
93. **Mihhail Berezovski.** *Numerical Simulation of Wave Propagation in Heterogeneous and Microstructured Materials.* 2010.
94. **Tamara Aid-Pavlidis.** *Structure and Regulation of BDNF Gene.* 2010.
95. **Olga Bragina.** *The Role of Sonic Hedgehog Pathway in Neuro- and Tumorigenesis.* 2010.
96. **Merle Randrüüt.** *Wave Propagation in Microstructured Solids: Solitary and Periodic Waves.* 2010.
97. **Marju Laars.** *Asymmetric Organocatalytic Michael and Aldol Reactions Mediated by Cyclic Amines.* 2010.
98. **Maarja Grossberg.** *Optical Properties of Multinary Semiconductor Compounds for Photovoltaic Applications.* 2010.
99. **Alla Maloverjan.** *Vertebrate Homologues of Drosophila Fused Kinase and Their Role in Sonic Hedgehog Signalling Pathway.* 2010.
100. **Priit Pruunsild.** *Neuronal Activity-Dependent Transcription Factors and Regulation of Human BDNF Gene.* 2010.
101. **Tatjana Knjazeva.** *New Approaches in Capillary Electrophoresis for Separation and Study of Proteins.* 2011.
102. **Atanas Katerski.** *Chemical Composition of Sprayed Copper Indium Disulfide Films for Nanostructured Solar Cells.* 2011.
103. **Kristi Timmo.** *Formation of Properties of CuInSe<sub>2</sub> and Cu<sub>2</sub>ZnSn(S,Se)<sub>4</sub> Monograin Powders Synthesized in Molten KI.* 2011.
104. **Kert Tamm.** *Wave Propagation and Interaction in Mindlin-Type Microstructured Solids: Numerical Simulation.* 2011.
105. **Adrian Popp.** *Ordovician Proetid Trilobites in Baltoscandia and Germany.* 2011.
106. **Ove Pärn.** *Sea Ice Deformation Events in the Gulf of Finland and This Impact on Shipping.* 2011.
107. **Germo Väli.** *Numerical Experiments on Matter Transport in the Baltic Sea.* 2011.
108. **Andrus Seiman.** *Point-of-Care Analyser Based on Capillary Electrophoresis.* 2011.
109. **Olga Katargina.** *Tick-Borne Pathogens Circulating in Estonia (Tick-Borne Encephalitis Virus, Anaplasma phagocytophilum, Babesia Species): Their Prevalence and Genetic Characterization.* 2011.
110. **Ingrid Sumeri.** *The Study of Probiotic Bacteria in Human Gastrointestinal Tract Simulator.* 2011.
111. **Kairit Zovo.** *Functional Characterization of Cellular Copper Proteome.* 2011.
112. **Natalja Makarytsheva.** *Analysis of Organic Species in Sediments and Soil by High Performance Separation Methods.* 2011.
113. **Monika Mortimer.** *Evaluation of the Biological Effects of Engineered Nanoparticles on Unicellular Pro- and Eukaryotic Organisms.* 2011.

114. **Kersti Tepp.** *Molecular System Bioenergetics of Cardiac Cells: Quantitative Analysis of Structure-Function Relationship.* 2011.
115. **Anna-Liisa Peikola**. *Organic Aerogels Based on 5-Methylresorcinol.* 2011.
116. **Leeli Amon.** *Palaeoecological Reconstruction of Late-Glacial Vegetation Dynamics in Eastern Baltic Area: A View Based on Plant Macrofossil Analysis.* 2011.
117. **Tanel Peets.** *Dispersion Analysis of Wave Motion in Microstructured Solids.* 2011.
118. **Liina Kaupmees.** *Selenization of Molybdenum as Contact Material in Solar Cells.* 2011.
119. **Allan Olsper**. *Properties of VPg and Coat Protein of Sobemoviruses.* 2011.
120. **Kadri Koppel.** *Food Category Appraisal Using Sensory Methods.* 2011.
121. **Jelena Gorbatšova.** *Development of Methods for CE Analysis of Plant Phenolics and Vitamins.* 2011.
122. **Karin Viipsi.** *Impact of EDTA and Humic Substances on the Removal of Cd and Zn from Aqueous Solutions by Apatite.* 2012.
123. **David W. Schryer.** *Metabolic Flux Analysis of Compartmentalized Systems using Dynamic Isotopologue Modeling.* 2012